Nanowire-based solar cells:
Device design and implementation

THÈSE N^{O} 6077 (2014)

PRÉSENTÉE LE 7 FÉVRIER 2014
À LA FACULTÉ DES SCIENCES ET TECHNIQUES DE L'INGÉNIEUR
LABORATOIRE DES MATÉRIAUX SEMICONDUCTEURS
PROGRAMME DOCTORAL EN SCIENCE ET GÉNIE DES MATÉRIAUX

ÉCOLE POLYTECHNIQUE FÉDÉRALE DE LAUSANNE

POUR L'OBTENTION DU GRADE DE DOCTEUR ÈS SCIENCES

PAR

Anna DALMAU MALLORQUÍ

acceptée sur proposition du jury:

Prof. A. Mortensen, président du jury
Prof. A. Fontcuberta i Morral, directrice de thèse
Prof. J. R. Morante Lleonart, rapporteur
Prof. P. Roca i Cabarrocas, rapporteur
Prof. F. Sorin, rapporteur

ÉCOLE POLYTECHNIQUE
FÉDÉRALE DE LAUSANNE

Suisse
2014

To my father

Abstract

In the context of the current global energy crisis the interest for renewable energies in general and photovoltaic in particular has significantly emerged. For many years the efficiency of photovoltaic energy conversion has been limited to the detailed balance limit proposed by Shockley and Queisser, which takes into account intrinsic thermodynamic losses. Recently, new concepts have been proposed to increase the efficiency beyond this limit. One of these solutions includes the use of semiconductor nanowires, which benefit from their quasi–one dimensional geometry to enhance the light absorption and efficiently collect the carriers when designed in a radial manner. In this thesis, the potential of nanowire–based devices for photovoltaic applications is investigated in detail.

In the first part of the thesis, a top–down method to fabricate radial junction silicon microwire arrays is presented. The advantages and limitations of these kind of devices are identified. The importance of the thickness and doping concentration of both the *p*–core and *n*–shell on the photovoltaic performance is also highlighted.

Electronic recombination losses represent the main issue on nanowire array solar cells due to their high surface–to–volume ratio. The passivation of surface states is a crucial step to boost their efficiencies to the theoretical maximum. In the second part of this thesis, different materials are investigated for surface passivation purposes in the context of silicon photovoltaics. The analysis of the interface properties permits to distinguish between chemical– and field–effect–related passivation, which give rise to completely different passivation schemes. Their implementation and output on silicon nanowire arrays obtained by Near–Field Phase–Shift Lithography are compared.

The third part of the thesis lays emphasis on the front transparent electrode. The complexity of the 3D–structured surface of nanowire arrays is overcome by the formation of a highly conformal metal nanoparticle film via a polymer–brush–guided method. It is a novel and flexible process which allows to tune the type, size, shape and density of metallic particles by changing the template composition and thickness. This solution leads to an enhancement of light absorption due to an increased scattering from metallic nanoparticles.

Ordered growth of InAs nanowires on a patterned silicon substrate is presented in the last part of the thesis. The role of the pattern on the nanowire growth is studied in detail. The photovoltaic performance of InAs nanowires on silicon is tested and analyzed considering the fundamental physical properties of the junction.

Keywords: nanowire, solar cell, passivation, plasmons, heterojunction

Résumé

Dans le contexte actuel de crise énergétique, l'intérêt pour les énergies renouvelables en général, et pour l'énergie solaire en particulier, s'est ravivé. Depuis de nombreuses années, le rendement énergétique des cellules solaires a été fixé par le modèle du bilan détaillé proposé par Shockley et Queisser, qui tient compte des pertes thermodynamiques intrinsèques au système. Récemment, des nouveaux concepts pour repousser les limites du rendement énergétique ont été proposés. L'une de ces solutions consiste en l'utilisation des nanofils semi–conducteurs à jonction radiale, qui bénéficient de leur géométrie quasi–unidimensionelle pour améliorer l'absorption de la lumière et la séparation des charges. Au cours de cette thèse, le potentiel des dispositifs photovoltaïques à nanofils à été étudié en détail.

La première partie de la thèse présente une méthode de fabrication de réseaux de microfils de silicium à jonction radiale. Les avantages et les limites de ces types de dispositifs ainsi que l'importance de l'épaisseur et de la densité de dopage des régions p et n sont analysés.

La recombinaison de surface représente la principale source de pertes des dispositifs à base de nanofils à cause de leur rapport surface/volume élevé. La passivation des états de surface constitue une étape essentielle vers une efficacité proche du niveau maximal théorique. La deuxième partie de cette thèse compare différents matériaux en ce qui concerne leur qualité de passivation du silicium. La caractérisation de l'interface permet de distinguer entre une passivation chimique et une passivation à effet de champ électrique, qui donnent lieu à deux schémas de passivation différents. Leur implémentation et performances sur des réseaux de nanofils de silicium fabriqués par lithographie Near–Field Phase–Shift sont comparés.

La troisième partie de la thèse met l'accent sur l'électrode avant. Afin de surmonter la complexité liée à la tridimensionnalité de la surface des réseaux de nanofils, une procédé de préparation de chaînes de polymère greffées pour guider la formation d'une couche uniforme à base de nanoparticules métalliques a été conçu. Celui–ci est un processus souple et innovateur qui permet d'ajuster la taille, la forme et la densité des particules métalliques en modifiant la composition et l'épaisseur de la matrice. Cette solution mène à une meilleure absorption des rayons lumineux grâce à la contribution des nanoparticules métalliques à la dispersion de la lumière.

Enfin, la croissance ordonnée de nanofils d'InAs sur un substrat à motif de silicium est présentée et le rôle du motif dans la croissance du nanofil a été largement étudié. Le rendement photovoltaïque des réseaux de nanofils a été testé et analysé en considérant les propriétés physiques fondamentales de la jonction.

Mots clés : nanofil, cellule solaire, passivation, plasmons, hétérojonction

Contents

List of Figures

List of Tables

1 Introduction

The appropriateness of being dependent on fossil–fuel resources has been called into question both because of its limited availability and because its contribution to global climate change. The debate has pushed the market and governments to turn to renewable energies. Within this framework, photovoltaic energy has been proposed as one of the multiple alternatives to reach a global solution.

Over the last decades, solar photovoltaic production and research have grown significantly showing the increasing interest that this renewable source has stirred up among the scientific community and manufacturers. Among next generation solar cell designs, nanowires are highly appreciated because they provide many degrees of freedom.

The use of nanowire building blocks for photovoltaic applications will be the *leitmotif* of this thesis. The physics of p–n junction and the optical properties of nanowire arrays are briefly introduced in this chapter. The scope of the different chapters of the thesis are also summarized herein.

1.1 World Energy Overview

A capitalist world–economy is sustained by a constant growth in production and sales. Intrinsic to this growth imperative is the increase in energy demands. This led to a global energy consumption in 2011 of 12 billion tonnes of oil equivalent, 92% of which are oil, coal, natural gas and nuclear energy [1]. Nonrenewable energies are subject to a wide range of uncertainties, such as resource availability, macroeconomic trends, political conflicts or environmental policies. By way of illustration, Figure 1.1 shows the oil price evolution over the last four decades. The 1973 oil crisis rocked crude oil price by more than 100%, remaining very volatile since that collapse. Moreover, since 2005 crude oil supply turned to be unable to respond to increasing demands (Figure 1.2). Oil reservoirs are more unaccessible and more expensive techniques are required for extraction.

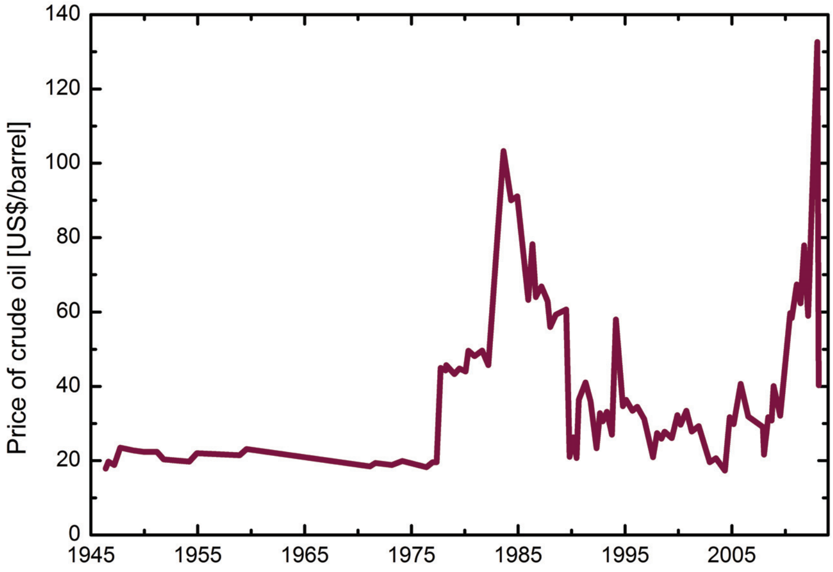

Figure 1.1: Real price of crude oil over the last half century in November 2008 dollars per barrel (adapted from [2]).

On the other hand, natural gas is still abundant. The employment of new extraction techniques such as hydraulic fracturing, also known as '*fracking*', has increased the production and thus, has driven down prices. However, there is a lot of controversy around the employment of such techniques and their environmental impact. Hence, regulatory legislations have increased over the last years.

The case of coal is a bit different. Even though it is the most polluting of all fossil fuels and its demand is always bound to environmental policies, coal can play a key role in the future since its reserves are enormous compared to oil and natural gas [4].

The less consumed non–renewable energy source is nuclear power. Around 5% of the world primary energy consumption in 2011 was supplied by this type of energy. However, 2011

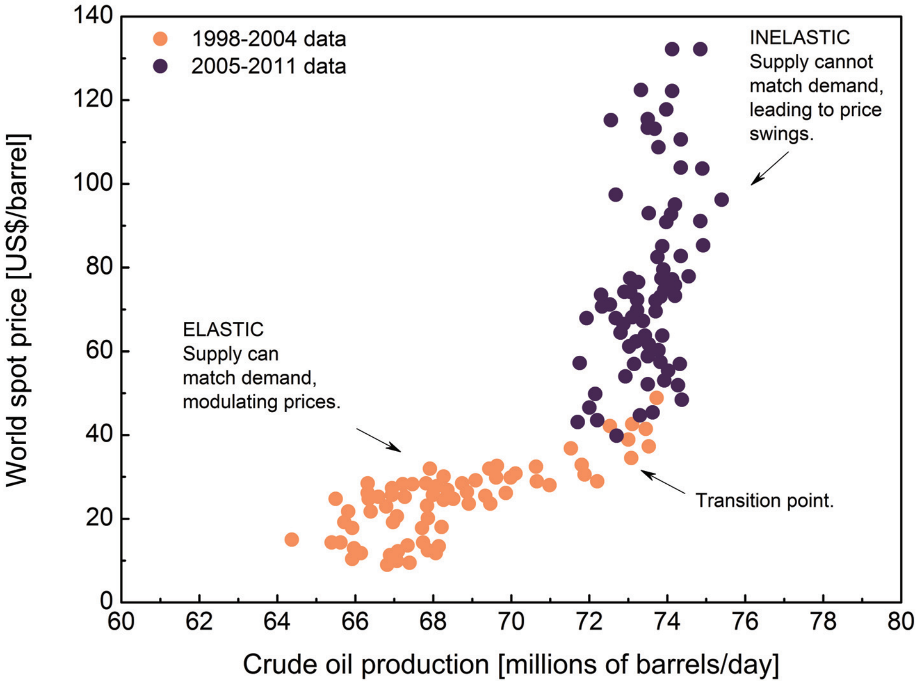

Figure 1.2: Conventional crude oil production as a function of price. From 2005 onwards, the production turned to be inelastic: a slight increase in production causes prices to ramp up (adapted from [3]).

nuclear accident in Fukushima, Japan, prompted a rethink of nuclear energy policy in many countries, leading to an immediate drop of world consumption of 4.3%, backing down to 2003 consumption rates [1].

The renewable sector (mainly biomass, wind, hydro and photovoltaic) has not been immune to the recent global economic crisis, but its strong growth in Asia maintained the upward trend. Moreover, it still benefits from government policies concerning both economic stimulation of the sector and penalization of polluting fuels. Photovoltaic installations were not an exception to this legalistic advantages. Solar systems were already used at the 1960s in specialised applications. The high cost of this technology prevented commercial deployment until the beginning of this century. This change resulted mainly from both a drastic cost reduction thanks to technological advances and the introduction of policy support through feed–in tariffs. Feed–in tariffs allowed the producers to recover the cost of the installation over its lifetime and, hence, reduce the project risk. This encouraged a massive investment in PV installations, resulting in a drastic drop of costs. However, when the Spanish incentives suddenly ended by September 2008, demand reduced sharply causing an excess of production and a plunge of prices. Solar–grade silicon price evolution depicted in Figure 1.3 clearly illustrates this fact. As a consequence, manufacturers started a price competition which pushed lots of them into bankruptcy [5].

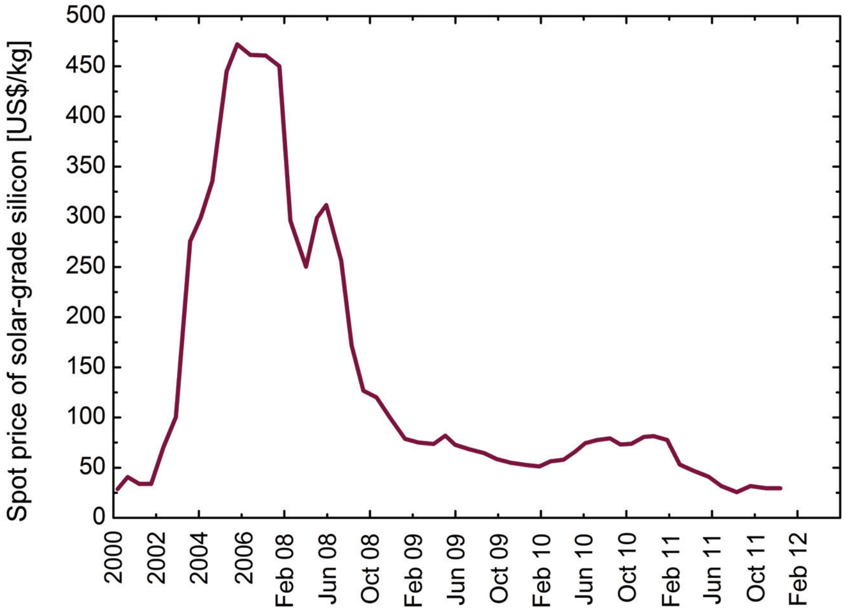

Figure 1.3: Spot price of solar–grade silicon ($/kg) (adapted from [5]).

In this context, state–of–the–art technology broke into the market jumping from research matter to large–scale production and commercialization. Two good examples of this are Innovalight^{TM} and Sol Voltaics^{TM}. Innovalight^{TM} [6] is a Silicon Valley company which manufactures a nanotechnology–based silicon ink that boosts solar cell performance by adding a single low–cost process step at the customer production line. The idea is as simple as suspending silicon nanocrystals uniformly in a solvent, so that precise micron–thick lines can be printed exactly under the front metal contacts, forming a selectively highly doped emitter. Such a promising technology increases the cell's output power 5 to 7%. And, above all, it is achieved at an almost negligible cost for solar cell manufacturers.

On the other hand, Sol Voltaics^{TM} [7] is a young company founded in 2008 by a Swedish research group based in Lund University and led by Prof. Lars Samuelson. While tens of solar panel makers go bankrupt, Sol Voltaics^{TM} comes into scene and proposes high–efficient nanowire–based solar cells. They propose devices made out of gallium arsenide (GaAs) nanowires grown through an economic process called Aerotaxy^{TM}. Gold nanoparticles are used as seed particles. When suspended in a gas mixture of precursors and heated up, one–dimensional GaAs structures start to form [8]. It is a continuous process that allows the growth of high–quality nanowires at low–cost fabrication and providing a reproducible dimension–control. The grown nanowires can be easily integrated into solar panel by deposition and alignment directly from the gas phase, or stored into a liquid for further processing steps.

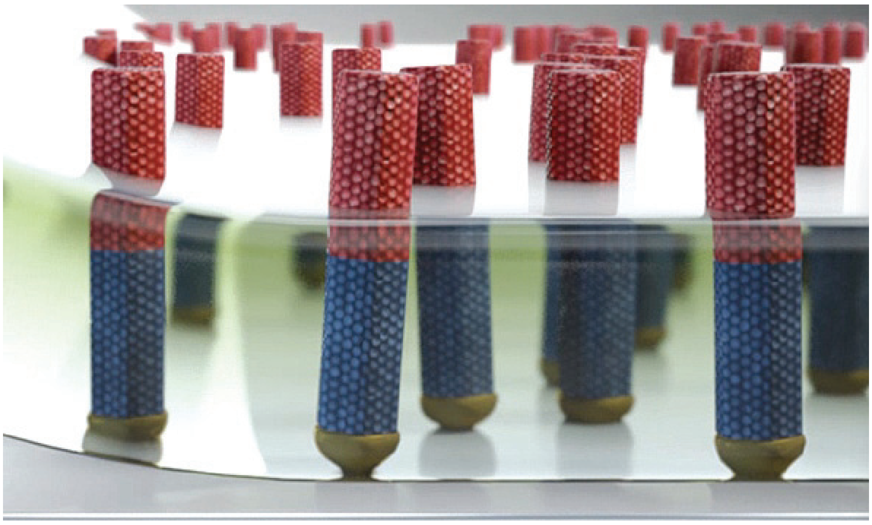

Figure 1.4: Sol Voltaics$^{\mathrm{TM}}$ produces gallium arsenide nanowires through an economic process called Aerotaxy$^{\mathrm{TM}}$ and integrates them into solar panels (taken from [7]).

1.2 Theoretical Background

Solar cells benefit from the photovoltaic effect to convert light into electricity [9]. Carriers are generated by absorption of photons with higher energy than the band gap and then separated at the *p*–*n* junction. A *p*–*n* junction is the union of two regions doped *p*–type (the Fermi level is closer to the valence band) and *n*–type (the Fermi level is closer to the conduction band), respectively. When these two regions are brought together, electrons flow from the *n*–side to the *p*–side and viceversa for holes, until the system reaches thermodynamic equilibrium and the Fermi level is the same in both regions. The alignment of the Fermi level induces the bending of both the conduction and valence bands at the junction. Due to the potential gradient an electric field is established, which creates a drift current opposite to the diffusion current. The region affected by the electric field is called *depletion region*. Then, an electron excited within this region drifts to the *n*–doped zone and the opposite for holes. Figure 1.5 shows the band diagram of both regions before and after bringing them together.

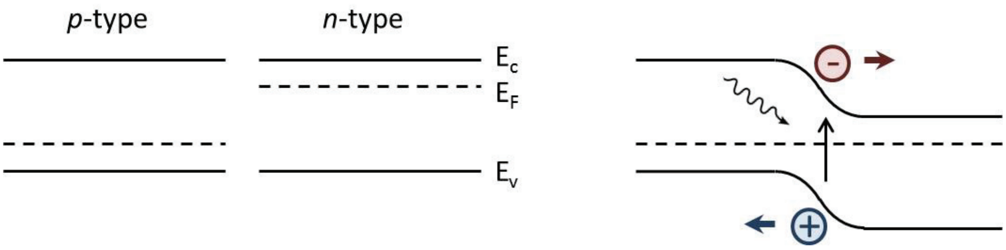

Figure 1.5: Schematic representation of the band diagram of a *p*– and *n*–type semiconductor in isolation (left) and separation of photogenerated carriers at the junction (right).

The photogenerated current can work as a current source in an external circuit. The current–voltage characteristics in the dark have a diode–like behavior and under illumination the curve is shifted due to the generated photocurrent (Figure 1.6). The range of bias between 0 and V_{oc} defines the regime in which the device is generating power. From this curve we can extract different values that describe the performance of the cell.

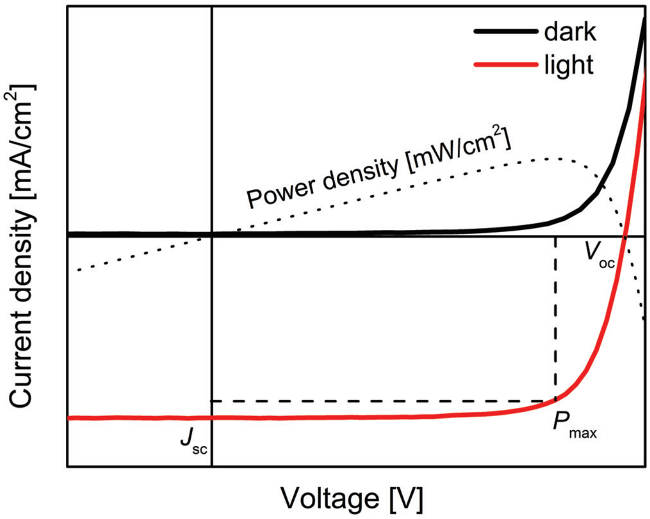

Figure 1.6: Current–voltage characteristics in the dark (black line) and under illumination (red line) of a solar cell. The power density is defined by the dotted line.

Efficiency is a term that gives the ratio between the maximum output power of the solar cell, P_{max}, and the incident light power, P_{in}:

$$\begin{aligned} \eta &= \frac{P_{\text{max}}}{P_{\text{in}}} && (1.1) \\ &= \frac{J_{\text{sc}} V_{\text{oc}} FF}{P_{\text{in}}}, && (1.2) \end{aligned}$$

where J_{sc} is the short–circuit current density and defines the current density at zero bias, V_{oc} is the open–circuit voltage which is the potential difference when contacts are isolated and the fill factor, *FF*, is the ratio of the maximum electrical power output to the product of V_{oc} and J_{sc}:

$$FF = \frac{P_{\text{max}}}{J_{\text{sc}} V_{\text{oc}}}. \tag{1.3}$$

Its value ranges from 0 to 1 and it decreases with the presence of shunt and series resistances.

The current-voltage characteristics for a *p–n* junction under illumination is given by the equation:

$$J = J_0 \left[\exp\left(\frac{qV}{nkT} \right) - 1 \right] - J_{\mathrm{sc}}, \tag{1.4}$$

where $q = 1.602 \times 10^{-19}$ C is the electronic charge, $k = 1.38 \times 10^{-23}$ $\mathrm{m^2 kg\, s^{-2}\, K^{-1}}$ is Bolzmann's constant and the temperature T is assumed to be 300 K. n is the ideal factor and determines how ideal is the device response (it ranges from 1, for an ideal cell, to 2) and J_0 is the saturation current density. This in turn leads to the following expression for V_{oc}:

$$V_{\mathrm{oc}} = \frac{nkT}{q} \ln \left[\frac{J_{\mathrm{sc}}}{J_0} + 1 \right]. \tag{1.5}$$

Shockley and Queisser [12] found the theoretical upper limit for efficiency of a single *p*–*n* junction with a band gap, $\mathrm{E_g}$, of 1.1 eV to be 30%. This detailed balance limit follows from the assumptions that all the incoming light with energy greater than $\mathrm{E_g}$ is absorbed, exactly one electron–hole pair is generated by each absorbed photon and only radiative recombination

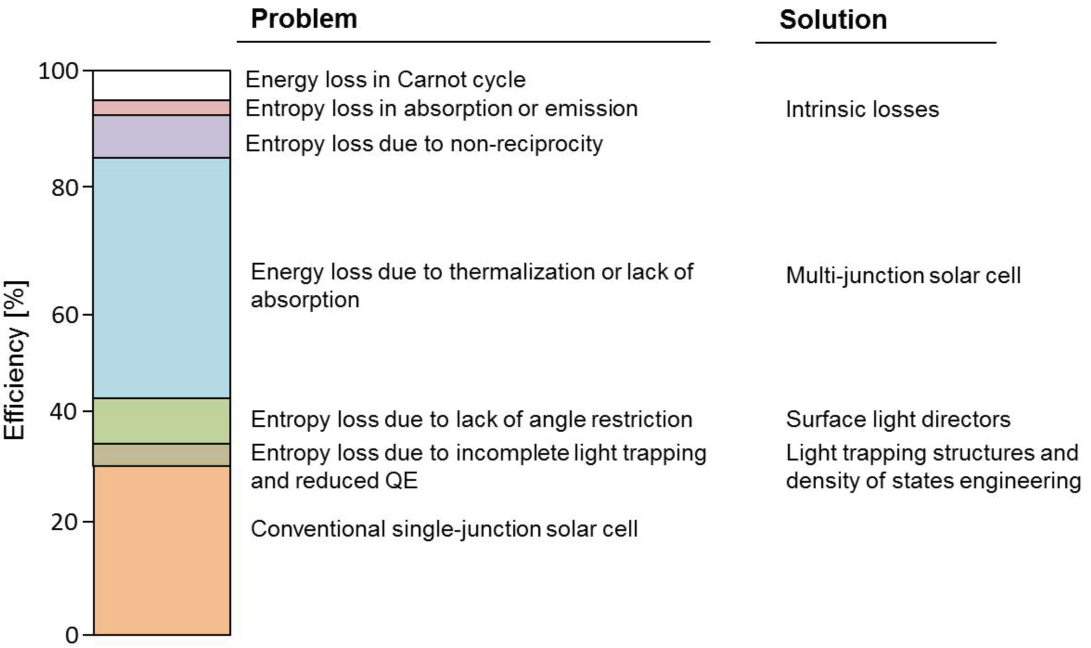

Figure 1.7: Thermodynamic losses in solar–energy conversion. The upper limit of the orange bar depicts the record efficiency of 28.3% for a conventional single–junction solar cell [10]. The rest of the bars indicate losses due to thermodynamics. Possible solutions to reduce these losses are listed in the right–hand column (adapted from [11]).

occurs, *i.e.* spontaneous photon emission.

Figure 1.7 schematizes the thermodynamic losses that limit the efficiency of conventional solar cells [11]. The first factor is the thermalisation that follows a band-to-band excitation. The deficit between the photon energy and the photovoltage ($E - qV_{\mathrm{oc}}$) is lost to heat. Moreover, the open–circuit voltage is defined by the electron and hole quasi–Fermi level splitting and it is always smaller than the band gap energy according to:

$$qV_{\mathrm{oc}} = E_g\left(1 - \frac{T}{T_{\mathrm{sun}}}\right) - kT\left[\ln\left(\frac{\Omega_{\mathrm{emit}}}{\Omega_{\mathrm{sun}}}\right) + \ln\left(\frac{4n^2}{I}\right) - \ln(\mathrm{QE})\right], \tag{1.6}$$

where T and T_{sun} are the temperatures of the cell and the sun, respectively, Ω_{emit} and Ω_{sun} correspond to the solid angle of emission and collection, I is the light concentration factor (I=1 in the case of a planar cell without any antireflection coating) and n is the refractive index. The first term on the right represents fundamental thermodynamic losses based on Carnot's theorem. The first term in square brackets is the entropy loss on photon absorption and spontaneous emission due to a higher solid angle of the latter. The second term in the square brackets corresponds to losses due to poor absorption. The last term, where $\mathrm{QE} = R_{\mathrm{rad}}/(R_{\mathrm{rad}} + R_{\mathrm{nrad}})$ is the quantum efficiency for radiative recombination, describes non–radiative recombination losses. These losses are intimately related to the external photon emission efficiency: a good extraction of internal photons allows high internal luminescence and carrier density, leading to higher open–circuit voltages [13].

The so–called 'third generation' solar cells have introduced new concepts and technologies which extend in scope beyond the Shockley–Queisser limit. Spectral splitting (multiple and intermediate band gaps [14,15]), hot–carrier collection [16] or multiple exciton generation [17] are exciting developments that have the potential to result in high–efficiency photovoltaics. In the same way, nanostructures and nanostructured materials have been explored as active components of such devices. One example are semiconductor nanowires, which due to their one–dimensional structure, exhibit unique electrical, optical, magnetic and mechanical properties. During the last decade and thanks to their quantum properties, they have been largely investigated as building blocks for electronic, optoelectronic and sensor applications [18, 19], and recently they have been integrated as key PV elements.

The use of nanowires for photovoltaic applications presents several advantages such as the enhancement of absorption thanks to the light concentrating and light trapping properties of dense nanowire arrays or the possibility of decoupling light absorption and carrier collection into orthogonal directions by using radial *p–n* junctions [20]. These two factors allow the use of cheap materials as substrates and low–quality materials as active PV components.

Light absorption in nano and microwire arrays have been recently explored. This effect strongly depends on the nanowire dimensions, filling fraction and material properties and, hence, more than one model needs to be used to understand it. Thus, ray optics can explain light trapping in indirect band gap microwire (4 μm radius) arrays [21]. It has been found that when standing on a Lambertian back reflector, there is and asymptotic increase in light trapping for low filling factors that exceeds $2n^2$, being n the refraction index of the material. However, this model could not explain the increase in absorption of small wire arrays (1 μm radius). When nanowire diameters are smaller or comparable to the radiation wavelengths, optical interference and guiding effects play a dominant role. For direct band gap materials, nanowires exhibit resonances similar to those described by Mie theory, resulting in a built–in light concentration effect of ~8 [22]. It should be noted that both effects enable nanowires to be further separated from one another, resulting in a reduction of material volume and, hence, a reduction in costs and in an increase of efficiency because of an increase of open–circuit voltage coming from the self–concentration effect.

Moreover, the use of nanowires reports more benefits when using a radial–junction configuration. In particular, this geometry is interesting for materials that have diffusion lengths that are low relative to their optical thickness [20]. An optimal design should be a radius approximately equal to the minority carriers diffusion length and a length similar to the optical length of the material. Such a configuration will also allow high doping levels, which will lead to an increase of the built–in voltage.

However, owing to the high surface–to–volume ratio of nanowires, surface and junction recombination become the main handicaps to reach higher efficiencies, increasing the value of the last entropy loss in Equation 1.6.

1.3 Outline of the Thesis

In this thesis, the use of nanowires as building blocks for photovoltaic applications is studied. Each chapter is dedicated to analyze in detail a part of the device, reinforcing the advantages of using nanowires and limiting their intrinsic constraints. Most of the work has been done on silicon micro/nanowires homojunction solar cells. However, one chapter is also focused on III/V nanowires, such as InAs, and their integration on silicon.

In chapter 2, we study the impact of the junction design on the carrier collection and on the overall efficiency of the cell. Radial junction Si microwires are fabricated and different junction depths and p–doping concentrations are compared.

Chapter 3 focuses on the analysis of surface recombination on silicon nanowires. In this case, and in order to increase the effect of the recombination on the cell performance, we employe axial junction Si nanowires fabricated by means of an innovative photolithography method called phase–shift lithography. Different surface passivation techniques are used and their effect on minority carriers lifetime is discussed.

In chapter 4, the importance of a good transparent front electrode is emphasized. A novel approach based on thin metal films generated via a polymer–brush–guided method is presented. The homogeneity of the film along the wires and its optical and electrical properties are studied.

Finally, chapter 5 is dedicated to the growth of ordered arrays of InAs nanowires on a patterned Si wafer by means of molecular beam epitaxy (MBE). A model that drives the nanowire growth on a defined pattern is proposed. The performance of such a heterojunction as a photodiode is also measured and analyzed.

2 Radial Junction Engineering on Si Microwire–Array Solar Cells

In this chapter, we outline our approach to fabricate radial junction silicon microwire solar cells using a top–down method. Radial *p–n* junction configuration presents several advantages over planar devices, but also some drawbacks. All the *pros* and *cons* will be analyzed. Furthermore, the impact of the junction design on the light–to–current conversion efficiency of the cell is also reported. The results reveal the importance of the junction depth, core thickness or doping concentrations when designing the device.

Publications:
A. Dalmau Mallorquí, F. M. Epple, D. Fan, O. Demichel, and A. Fontcuberta i Morral, *Effect of the p–n Junction Engineering on Si Microwire–Array Solar Cells*, Phys. Status Solidi A **209** (2012), 1588–1591.

2.1 Introduction

The use of nanowires for photovoltaic applications constitutes a promising approach thanks to their high aspect–ratio. Densely packed vertical wires can improve light absorption thanks to their anti–reflective and light trapping properties. But what is even more interesting is that they offer the advantage of decoupling light absorption and carrier collection into orthogonal directions by using a radial junction: while photogenerated minority carriers are collected in the radial direction, incident light is absorbed axially. Conventional planar *p–n* junction geometry requires highly absorbing and pure materials. Highly absorbing in order to absorb the photons close to the junction and to reduce the volume of material used and highly pure to increase the minority carrier diffusion length and improve the collection of photogenerated carriers. This is especially critical for materials with high optical thickness (we define optical thickness of a material as the thickness required to absorb 90% of the above–band–gap photons), such as the widely–used silicon.

These constraints can be overtaken by introducing a radial junction: nanowires can be as long as needed to absorb all the light and thinner than the minority–carrier diffusion length. This entails the possibility of optimizing both absorption and carrier collection while using low–quality materials as active PV components [20, 23]. It was Kayes *et al.* in 2005 who first gave a boost to the field demonstrating theoretically the benefits of using this configuration. Large efficiency gains (from 1.5% to 11%) were predicted for silicon nanowires [20]. However, was not before 2007, when the group of Lieber reported about single *p–i–n* nanowires, that the first experiment was demonstrated [24]. The same group compared, later on, the response of optimized *p–i–n* nanowires in axial and coaxial geometries [25]. The values of short–circuit current density and efficiency obtained were largely better in the case of radial configuration (24 in front of 3.5 mA/cm^2 and 3.4 in front of 0.5%, respectively) and confirmed the promising potential of such a design.

The first attempt on contacting vertical arrays of nanowires in parallel were published by Tsakalakos *et al.* [26]. *P*–core silicon wires grown by means of a VLS process coated with a conformal plasma–enhanced chemical vapor deposited *n*–doped a–Si:H shell on stainless steel substrate were fabricated. Although the results were low (V_{oc} ~0.13 V, FF~0.28 and η ~0.1%) they constituted the proof–of–concept of using such nanostructures on large area devices. Those results were later on improved by other groups [27–30]. For instance, the group of Atwater fabricated vertically aligned arrays of crystalline *p–n* junction Si microwires grown by a vapor–liquid–solid (VLS) process, exhibiting 3.81% conversion of simulated AM 1.5G solar illumination to electrical energy [31]. This performance was improved up to 5.64% by introducing Al_2O_3 particles in between the wires to scatter incident light and the best response was obtained by adding a passivation a–SiN_x:H layer, a Ag back reflector and Al_2O_3 scattering particles. This device produced a V_{oc} of 0.5 V, a J_{sc} of 24.3 mA/cm^2, a FF of 0.65 and an efficiency of 7.92%. But the best results on nanowire–based solar cells published up to now were obtained by the group of Borgström [32]. They succeeded in fabricating axial *p–i–n* InP nanowires arrays on *p*–doped InP substrate with efficiences up to 13.8%. They identified two key elements to optimize the cell performance: the nanowire diameter and the length of the top *n*–part. Moreover, even if InP has a direct and optimal band gap (1.34 eV) for single–junction devices, they understood that light absorption in nanowires does not follow the ray optics law.

Actually, lots of works have also been focused on improving the optical absorption. Zhu *et al.* proposed the use of nanocones and nanodomes to gradually reduce the effective refractive index [33, 34]. Such structures led to a 30% increase with respect to a planar film. On the other hand, some calculations have shown that certain periodic pillars can act as photonic crystals giving rise to a maximum light–trapping path length enhancement factor of several hundreds at resonance wavelengths, and exceeding Lambertian theoretical limit for most wavelengths [35]. However, the optimal geometrical parameters (diameter and pitch) to maximize the electrical conversion efficiency strongly depend on the material [36, 37]. Light absorption of ordered arrays of wires was compared, experimentally and theoretically, to randomly–arranged arrays by Convertino *et al.* They showed that an increase of the disorder degree of the wire arrangement results in an enhancement of the scattering cross–section [38].

One should also note that thanks to the small diameter of nanowires, there is an elastic relaxation at the nanowire sidewall surfaces that makes possible to grow sequences of large lattice mismatch materials one on top of each other. This provides the opportunity to grow III–V and II–VI nanowires on cheaper substrates such as Si and to fabricate defect–free multi–junction solar cells. One of the most widely used III-V semiconductor is GaAs. Its optimal band gap for solar spectrum (1.42 eV) and good absorption coefficient (it is a direct band gap material) convert GaAs to an interesting alternative to Si technology. Colombo *et al.* reported the highest efficiency for a single nanowire solar cell to date [39]. Radial *p*-*i*-*n* structures were fabricated by catalyst–free molecular beam epitaxy (MBE) growth, achieving an efficiency of 4.5% and a V_{oc} and FF of 0.6 V and 0.65, respectively. In parallel, LaPierre *et al.* fabricated an array of GaAs nanowires resulting in an efficiency of 0.8% [40]. Other III–V nanowire solar cells were created using InP or GaN with efficiencies of 3.37% and 0.19%, respectively [41, 42].

Another interesting approach is the use of nanowires in hybrid and dye–sensitized solar cells (DSC). Organic materials have lower carrier mobility than inorganic, what induces higher recombination losses. CdSe or CdTe nanorods embedded in a polymer matrix were used to provide a guided path for electrical transport in hybrid solar cells, obtaining an efficiency of 1.7% and 1.06%, respectively [43, 44]. The same idea was applied to dye–sensitized solar cells using TiO_2 or ZnO nanorods with efficiencies ranging from 0.5% to 6.2% [45–47]. Higher dye loadings should lead to an improvement of their performance, even though electron transport in the organic matrix is limited.

The flexibility and processability of polymer were exploited by the group of Atwater to design a method to peel off the nanowires from the growth substrate [48]. Free–standing Si wires grown on a Si(111) wafer were embedded into a polydimethylsiloxane (PDMS) polymer matrix and subsequently cured and they were then mechanically removed from the substrate. This technique gives the opportunity to reuse the substrate to grow new wire arrays, increasing the economical benefits of such a device.

2.2 Sample Preparation

Hexagonally ordered arrays of microwires were fabricated by a combination of optical lithography and deep reactive ion etching. We used 380–μm thick Czochralski <100> Si wafers doped with B and covered by a layer of 500 nm thermally grown SiO_2. For a further analysis on the importance of the doping concentration of the base, different resistivities were selected: 0.1–0.5 Ω·cm, 1–5 Ω·cm and 1–10 Ω·cm. The oxide layer was used as mask material for the subsequent long etching process.

Wires were defined by photolithographically patterning AZ1512H photoresist (Figure 2.1a)and transferred to Si substrate by a two-step reactive ion etching. C_4F_8 plasma was used to remove SiO_2, followed by a Bosch process (which alternates between a SF_6 plasma etching and a C_4F_8 chemical passivation) that defined the final length of the wires (Figure 2.1b). Surface defects and impurities caused by the etching processes were latterly removed by oxidizing the surface 100 nm. In order to protect the back side of the wafer from subsequent diffusion, a layer of oxide was needed. Thus, prior to stripping off the oxide by a buffered HF dip, a thick layer of photoresist was spin coated on the rear surface. Once the front side was oxide–freed, the photoresist was removed. At this point, a radial n–shell was formed by diffusing $POCl_3$ for 15 min at a temperature changing from 850°C to 1100°C (Figure 2.1c). Right after the diffusion,

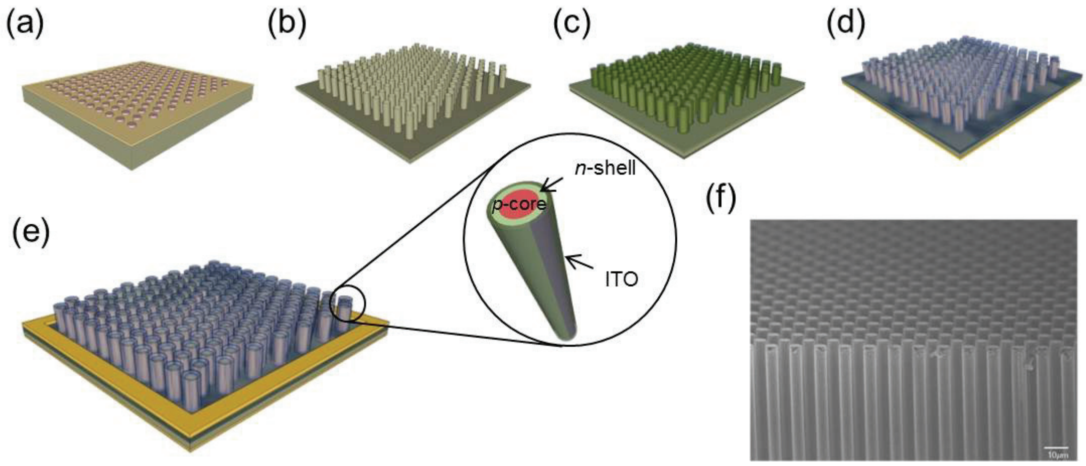

Figure 2.1: Schematic of the fabrication of radial p–n junction Si microwire arrays: (a) photolithographic patterning of a p–type Si wafer; (b) deep reactive ion etching to obtain p–core wire arrays; (c) $POCl_3$ diffusion to create an n–shell; (d) ITO and Al sputtering as front and rear contacts, respectively; and (e) evaporation of Ti/Au contacts around the arrays. A detail of the resulting cross–section is also depicted. (f) SEM image of a microwire array viewed at ~ 30° tilt.

the surface was again exposed to buffered HF long enough to remove the oxide grown during diffusion. Higher diffusion temperatures were found to increase the depth of the junction and to decrease the steepness of the doping concentration gradient along the wire radius.

The wafer was then exposed for the last time to buffered HF in order to remove native oxide and immediately after both front and rear contacts were made. A quasi-conformal layer of indium tin oxide (ITO) was sputtered on the front side (measuring 570 nm thick on a planar surface) and 200 nm of aluminium were also sputtered on the rear surface (Figure 2.1d). ITO was used as front contact due to its transparency and high conductivity and aluminium was chosen to create an ohmic contact to the *p*-doped base. Finally, in order to avoid punching ITO by the probe tip when measuring, Ti/Au (10/100 nm) pads were evaporated through a metallic mask around the arrays (Figure 2.1e).

2.3 Results

Microwire–based solar cells were then tested under AM 1.5G illumination (Sol2A Oriel) and in the dark and compared with their planar counterparts. The best cell made up to date exhibited an efficiency of 10.13%, a J_{sc} of 23.63 mA/cm^2, a V_{oc} of 571.7 mV and a FF of 0.75. For this sample, the wire diameter was 2.4 μm with a length of 37 μm, the doping concentration of the substrate was 3.5×10^{16} cm^{-3} and the diffusion temperature 900°C. The wire array surface was 25 mm^2 and the total illuminated cell area was 29.16 mm^2. In all cases J_{sc} is calculated by normalizing to the total illuminated cell area. Figure 2.2 shows the I–V response of this cell and its planar counterpart under illumination. The 20% and 12% increase in J_{sc} and FF for microwire–based cells suggest that the array of radial–junction microwires acts as both a good

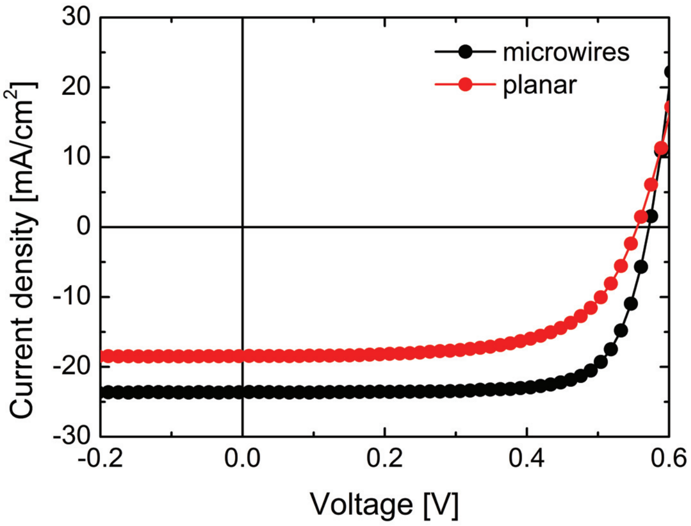

Figure 2.2: I–V characteristics of Si planar and nanowire based solar cells under AM 1.5G illumination.

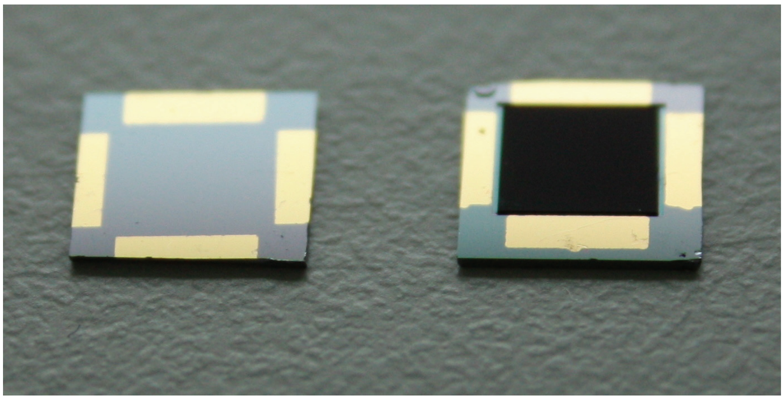

Figure 2.3: Optical image of a planar cell (on the left) and a microwire array (on the right). The better light absorption of the microwire array is visible to the naked eye.

light–trapper and a good carrier collector.

Figure 2.3 shows visible evidence of light absorption enhancement in microwire arrays. In order to better analyze it, the effect of the wire length on light absorption was studied by measuring the reflectivity with an integrating sphere. The sample was illuminated by a white light and diffuse– and specular–reflected light was captured by a sphere coated by a highly reflecting diffusive material such as $BaSO_4$. In this way, all reflected light got trapped inside the sphere and captured by a spectrometer. The relation between wire length and reflectivity is shown in Figure 2.4a. The wavy profile showed by planar devices is due to ITO reflectivity. This reflectivity is less pronounced when increasing the roughness of the surface. The optical thickness of silicon is 125 μm. In our case, as the thickness of the planar device is 380 μm we consider that the transmission of the substrate is 0. Furthermore, the microwire diameter and spacing were kept constant for all the samples, so the effective refractive index at the interface between air and microwire array was the same. Hence, the absorption enhancement when increasing the microwire length could only be induced by an increase of the light–trapping effect (Figure 2.4b). However, the increased absorption not necessarily leads to an increased short–circuit current density as a function of microwire length. J_{sc} and FF trends show that the increased surface and junction areas also impact on recombination. Figure 2.4d illustrates that for short lengths the effect of light trapping dominates over recombination losses but for higher lengths it reverses and the enhancement of surface and junction recombination losses lead to a decrease of photocurrent and fill factor.

The improvement on carrier collection due to the core–shell configuration is shown in Figure 2.4c. EQE of microwire–based devices is higher than the one of planar cells, especially for long wavelengths which are absorbed deep inside the base and are more likely to recombine before reaching the junction. Nevertheless, for very long wires recombination losses dominate and the number of collected carriers is reduced. These results are in agreement with some theoretical works reported elsewhere [49, 50]. They demonstrated that structured devices are more affected by surface recombination and that their efficiency drops more drastically

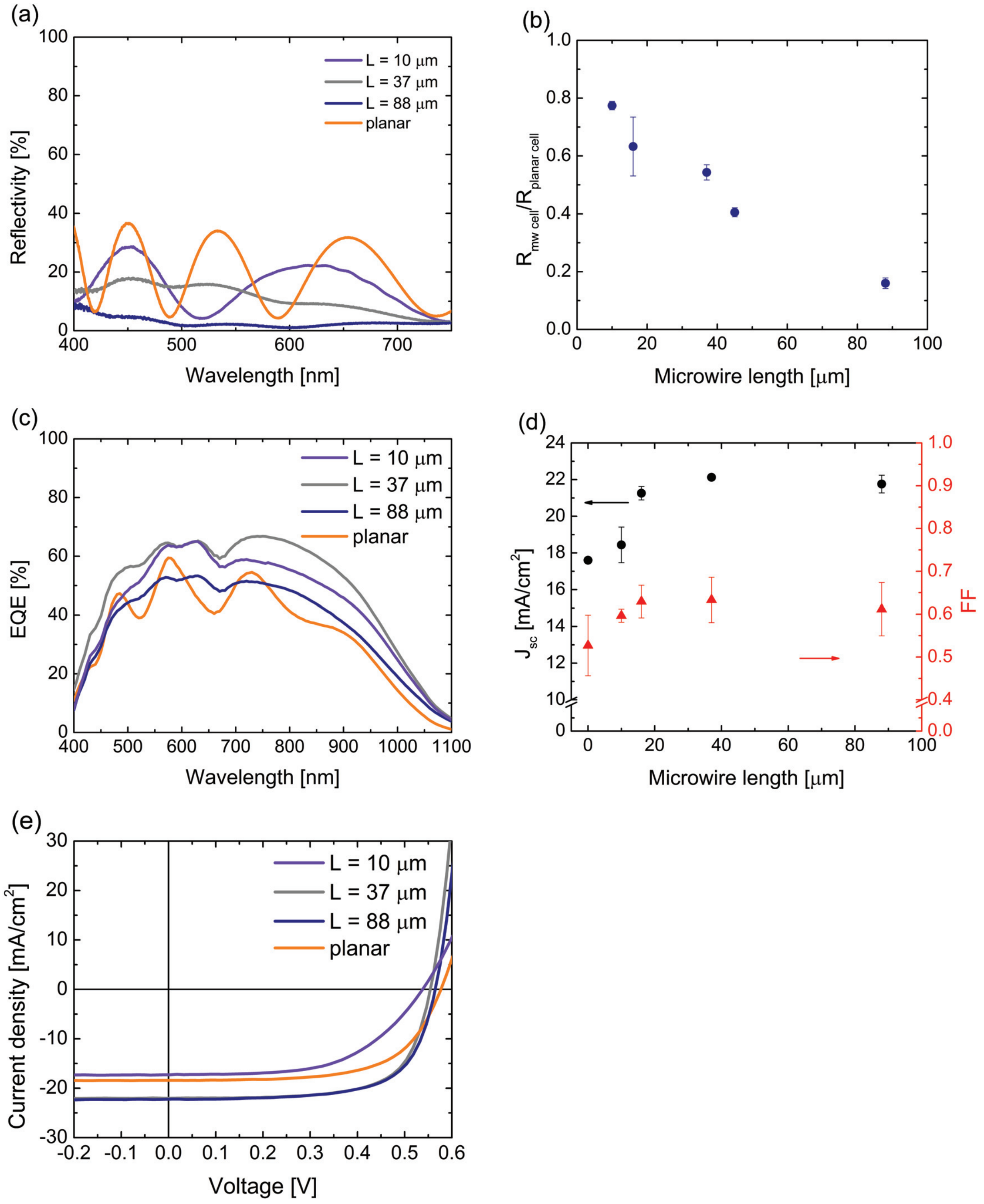

Figure 2.4: (a) Reflectivity measurements for different wire lengths, including a planar cell. (b) Ratio between microwire arrays reflectivity and planar cell reflectivity. (c) External Quantum Efficiency, (d) J_{sc} and FF values, and (e) I-V characteristics for different microwire lengths compared to planar cells (length = 0).

when increasing the surface recombination velocity than on planar devices. Therefore, a high surface recombination velocity can balance the gain from a better light absorption leading to lower efficiencies. The results showed in Figures 2.4a–d are all averaged over four samples. The performances of a single device for each case are compared in Figure 2.4e.

2.4 Junction Engineering

Photovoltaic energy conversion results from charge generation, charge separation and charge transport. The process of charge separation will be discussed in this section. A charge separation mechanism requires an internal driving force within the device. This driving force can be provided by spatial variations in the electronic properties, a so called *junction*. In semiconductor materials, there are two types of junctions: homojunctions and heterojunctions. The difference between these two type of junctions arises from the nature of the material: in homojunctions the junction is created by doping differently the two regions of the same semiconductor and in heterojunctions two different materials of different band gap are put together. In this section, the particular design of a Si *p–n* homojunction and how it affects the light conversion efficiency will be treated.

2.4.1 Doping Characterization

One of the key points on a *p–n* junction is the doping concentration of both regions. The difference in the work function of the two layers establish an electric field at the junction which drives the minority carriers photogenerated towards the opposite side. Thus, electrons will diffuse towards the *n*–region and holes towards the *p*.

Doping concentration profiles of the junctions were measured by capacitance–voltage measurements (Wafer Profiler CVP21) on flat substrates. C–V profiling is a method used for determining the doping profile of a semiconductor. The semiconductor is placed in contact with an electrolyte (ammonium bifluoride, $NH_4F{\cdot}HF$, 0.1 M) forming a Schottky barrier at the interface. This potential barrier leads to a depletion of carriers at the surface of the semiconductor and creates a capacitance. By applying an external voltage, the width of the depletion region and hence the capacitance may be changed. The dependence of the capacitance upon the applied voltage is described by the Mott-Schottky equation:

$$\frac{1}{C^2} = \frac{-2}{q\varepsilon_r\varepsilon_0 A^2 N}(V - V_{fb}), \tag{2.1}$$

where C is the capacitance, ε_0 is the vacuum permittivity (= 8.854×10^{-14} farad/cm), ε_r is the relative permittivity, A is the measured area, N is the carrier concentration, V represents the applied voltage and V_{fb}, the flat-band potential.

Thus, the carrier concentration N at the border of the depletion region is inversely proportional to the slope of $d(1/C^2)/dV$:

$$N = \frac{-2}{q\varepsilon_r\varepsilon_0 A^2 \frac{d\left(\frac{1}{C^2}\right)}{dV}}. \tag{2.2}$$

The same electrolyte is used to electrochemically etch the surface. Holes are conducted to the surface (by applying a forward bias in the case of *p*–type semiconductors or by creating electron-hole pairs using light in the case of *n*–type semiconductors) and, once there, they release valency electrons of the surface atoms by recombination. When all the valency electrons are removed, the ionized atom is dissolved into the electrolyte.

By alternating capacity measurements and electrochemical etching, a doping profile along the cross–section is obtained.

2.4.2 Variation on the Doping Concentration of the *p*–Core

In the next two sections, the impact of doping levels and junction position on the performance of the cell will be discussed in detail.

First, the effect of the doping concentration of the substrate was analyzed. In order to do so, three different substrates with different resistivities were chosen: 0.1–0.5, 1–5 and 1–10 Ω·cm. From C–V measurements it was found out that these resistivities correspond to a doping concentration of 3.5×10^{16}, 6.5×10^{14} and 4.2×10^{14} cm^{-3}, respectively. The diffusion process for the *n*–shell was done at 850°C for 35 minutes the three substrates and the resulting doping profile is shown in Figure 2.5. The erratic profile of the *p*–doped region at the interface with the *n*–shell is due to an experimental aberration resulting from the sharpness of the junction [51].

As expected from the fabrication process, we found that the doping concentration of the core is constant, while the doping concentration at the shell decreases from the surface to the core following the diffusion profile depicted by Fick's law:

$$\frac{\partial N_D}{\partial t} = D\frac{\partial^2 N_D}{\partial x^2}, \tag{2.3}$$

where N_D is the dopant concentration, D is the diffusivity of P into Si, t is the diffusion time and x the diffusion depth. Applying the boundary conditions, the Laplace transform reduces equation 2.3 to:

$$Q(x,t) = Q_s \cdot \mathrm{erfc}\left(\frac{x}{2\sqrt{Dt}}\right). \tag{2.4}$$

The phosphorus profile resulting from diffusion exhibits three distinct behaviors [52]:

- A **high concentration region**, where the total phosphorus concentration exceeds the

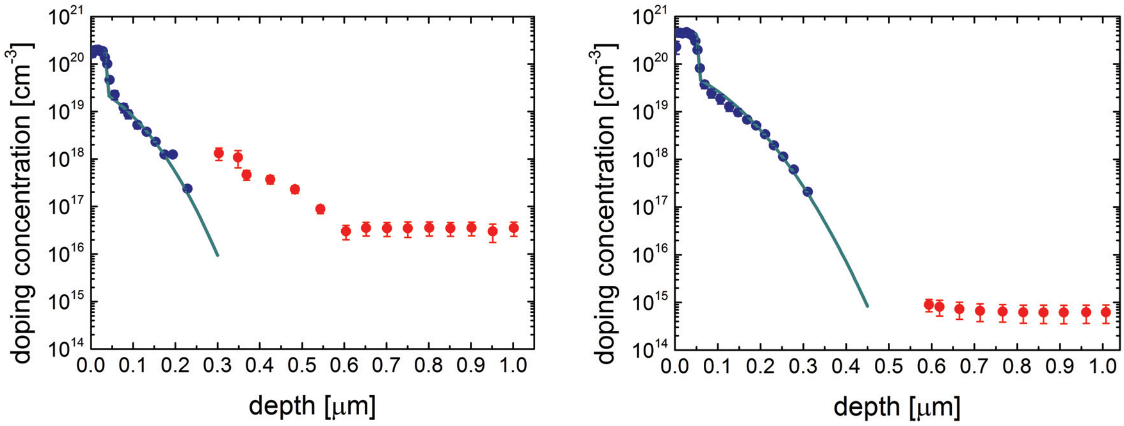

(a) $N_A = 3.5 \times 10^{16}$ cm^{-3}

(b) $N_A = 6.5 \times 10^{14}$ cm^{-3}

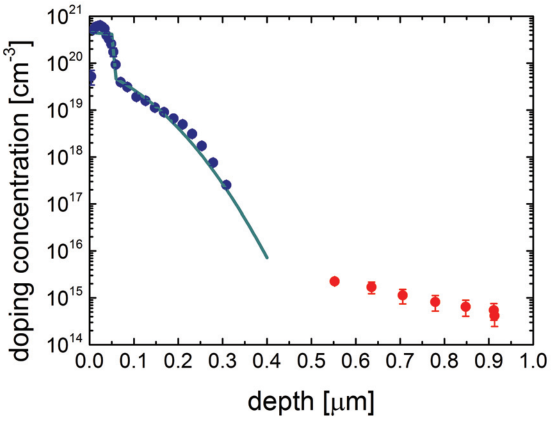

(c) $N_A = 4.2 \times 10^{14}$ cm^{-3}

Figure 2.5: Doping profiles along the cross–section for a diffusion temperature of 850°C. Blue dots represent experimentally measured *n*–doping and red dots, *p*–doping. The continuous lines show the simulated diffusion profiles.

free carrier concentration. In this region the diffusivity is given by:

$$D_{\text{high}} = 3.85 \exp\left(\frac{-3.66}{kT}\right) + 44.2 \exp\left(\frac{-4.37}{kT}\right)\left[\frac{n_{\text{s}}}{n_{\text{i}}}\right]^2, \tag{2.5}$$

where n_{i} is the intrinsic concentration and n_{s} is the concentration at the surface.

- A **kink** in the profile at an electron concentration of:

$$n_{\text{e}} = 4.65 \cdot 10^{21} \exp\left(\frac{-0.39}{kT}\right), \tag{2.6}$$

- A **tail region** of enhanced diffusivity. Here the diffusivity is expressed by:

$$D_{\text{tail}} = 3.85 \exp\left(\frac{-3.66}{kT}\right) + 4.44 \exp\left(\frac{-4}{kT}\right)\frac{n_{\text{s}}^3}{n_{\text{e}}^2 n_{\text{i}}}\left[1 + \exp\left(\frac{0.3}{kT}\right)\right]. \tag{2.7}$$

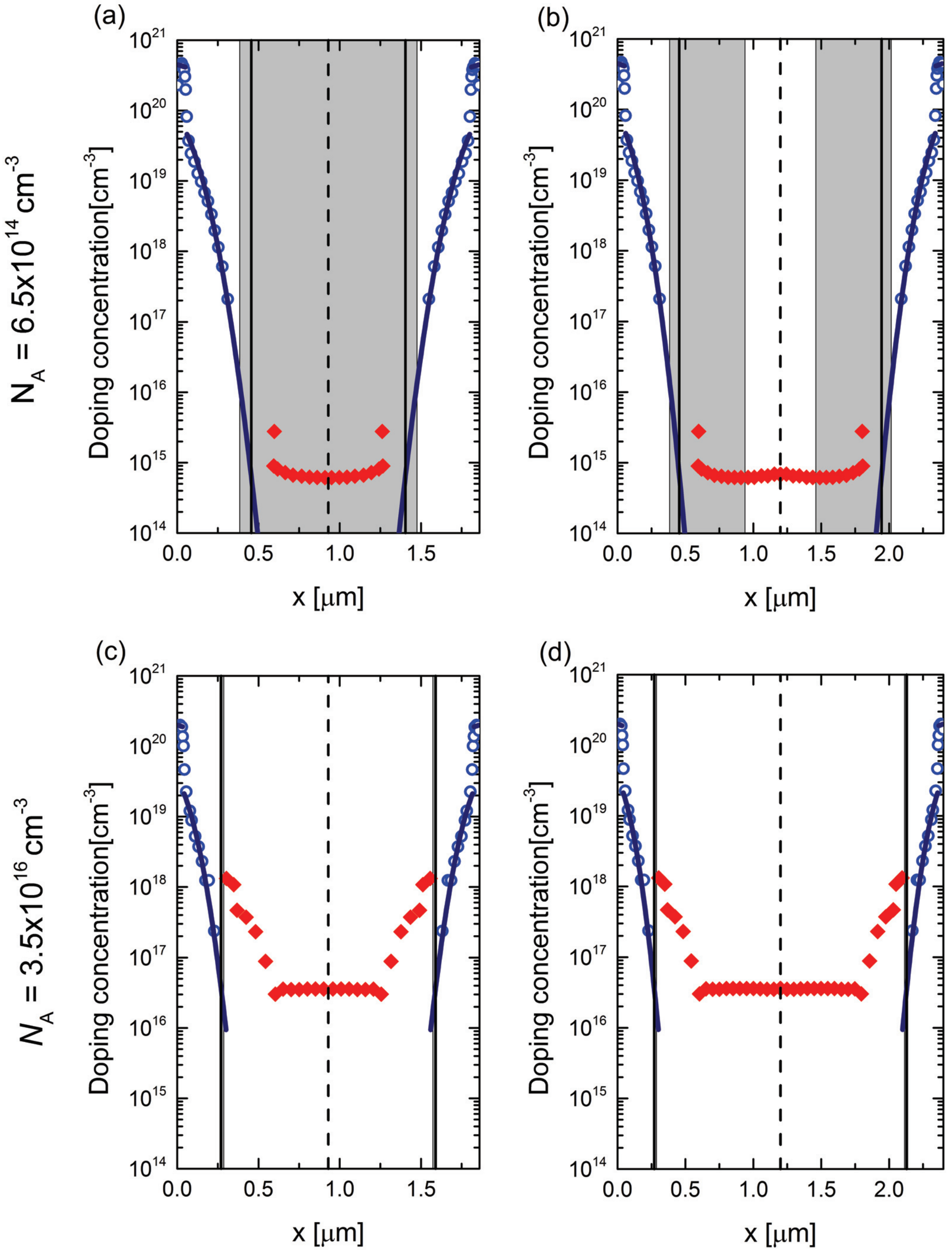

Figure 2.6: Doping profiles across the wire cross–section. The symbols represent experimental measurements and the continuous lines show the simulated diffusion profiles. Vertical black lines define the position of the junction, while grey areas represent depleted regions for four different situations: (a) $N_A = 6.5 \times 10^{14}$ cm^{-3}, $\phi = 1.86\mu$m; (b) $N_A = 6.5 \times 10^{14}$ cm^{-3}, $\phi = 2.4\mu$m; (c) $N_A = 3.5 \times 10^{16}$ cm^{-3}, $\phi = 1.86\mu$m; (d) $N_A = 3.5 \times 10^{16}$ cm^{-3}, $\phi = 2.4\mu$m.

As shown in Figure 2.6, the fitting of the doping profiles for a diffusion of $POCl_3$ at 850°C and 35 min (corresponding to the continuous lines) are in agreement with CV measurements. As it can be seen, the higher is the doping level of the substrate the shallower is the junction and the higher the gradient within the shell. In order to understand how these two phenomena could affect the performance of the device, we have calculated the depletion width in both regions by solving Poisson's equation at the junction. Assuming the continuity of the electric field, ξ, at the junction and fixing the differential potential between n and p regions to be equal to the built–in voltage (V_{bi}), this yields [53]:

$$\frac{1}{\varepsilon_{\mathrm{r}}\varepsilon_0}\int_{x_{\mathrm{j}}}^{x_{\mathrm{n}}} \rho(x)\mathrm{d}x = \frac{1}{\varepsilon_{\mathrm{r}}\varepsilon_0}\int_{-x_{\mathrm{p}}}^{x_{\mathrm{j}}} \rho(x)\mathrm{d}x, \tag{2.8}$$

$$V_{\mathrm{bi}} = -\int_{-x_{\mathrm{p}}}^{x_{\mathrm{n}}} \xi(x)\mathrm{d}x, \tag{2.9}$$

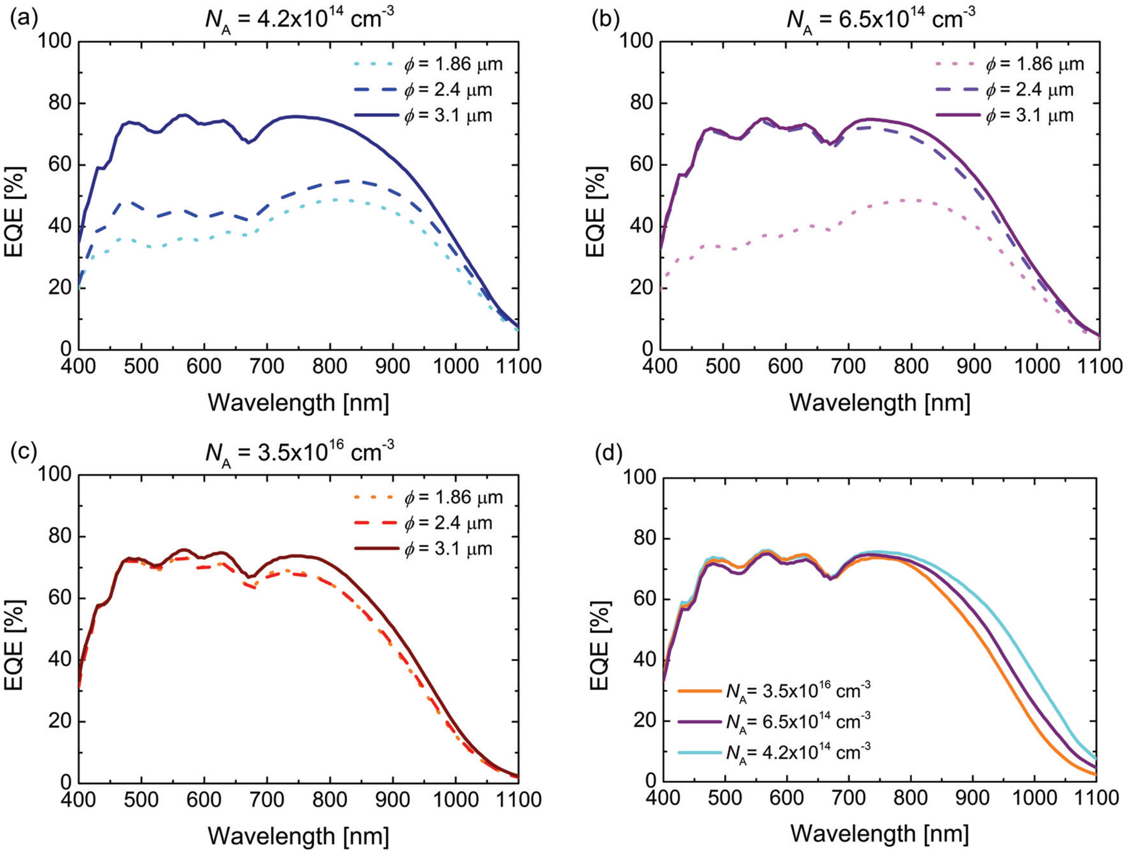

Figure 2.7: External quantum efficiency as function of the diameter for (a) $N_{\mathrm{A}} = 4.2 \times 10^{14} cm^{-3}$, (b) $N_{\mathrm{A}} = 6.5 \times 10^{14} cm^{-3}$ and (c) $N_{\mathrm{A}} = 3.5 \times 10^{16} cm^{-3}$. (d) Comparison of the EQE of all three p–doping concentrations for a wire diameter of 3.1 μm.

where ρ is the net charge density, x_j is the junction depth and x_n and x_p denote the depletion limits. The depletion widths resulting from these calculations are reported in Table 2.1 and transposed to the wire cross–section (indicated by grey areas in Figure 2.6). The plot shows the microwire cross–section with the doping profiles and the depletion region widths for two different *p*–doping concentrations (6.5×10^{14} and 3.5×10^{16} cm^{-3}) and wire diameters (1.86 and 2.4 μm). Comparing these two cases, we observe that wires with higher *p*–doping concentration present thinner depletion widths (77 nm compared to 555 nm) and shallow junction depths (270 nm instead of 455 nm). As a consequence, for the smallest microwire diameter (1.86 μm) the core is fully depleted. This occurs for diameters of 1.86 and 2.4 μm when the *p*–doping concentration is 4.2×10^{14} cm^{-3} and for a diameter of 1.86 μm in the case of a *p*–doping concentration of 6.5×10^{14} cm^{-3}.

External quantum efficiencies (EQE) for all three dopings are compared in Figure 2.7. As shown in plots (a) and (b) of Figure 2.7, the quantum efficiency decreases significantly for small diameters and low *p*–doping concentrations, especially in the visible regime as the light is mainly absorbed in the wires. For long wavelengths, photons are absorbed beneath the wires [54] and the EQE for all the diameters becomes similar.

These low efficiencies for fully depleted wires could be explained by an enhancement of the recombination rate within the depleted shell [55, 56]. In order to align the Fermi level at both *p* and *n* sides, conduction and valence bands bend upward at the core of the wire. Thus, due to the internal electric field created by the band bending, electrons tend to move to the shell and holes are pushed to the core. However, a reduction of the wire diameter leads to a fully depleted core. In this case, holes get confined at the axis of the wire and the electron–hole pair

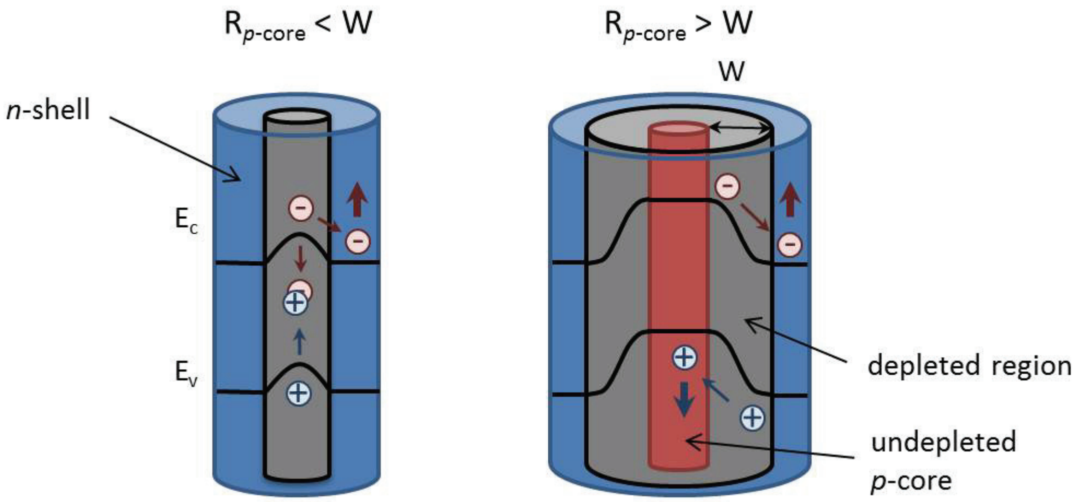

Figure 2.8: Sketch of the band diagram profile and carrier separation dependence on the relation between depletion width, W, and core radius, R_core. E_c and E_v denote conduction and valence band, respectively.

Table 2.1: Summary of the electrical characteristics of microwire arrays with different p–doping concentrations and diameters. The height of the microwires is 37 μm.

ϕ (μ m)	N_A (cm^{-3})	Junction depth (nm)	Depletion width (nm)	J_{sc} (mA/cm^2)	V_{oc} (V)	FF	η (%)
1.86	4.2×10^{14}	610	758	20.0±0.5	0.53	0.74±0.06	7.9±0.2
	6.5×10^{14}	455	555	19.8±0.2	0.55	0.71±0.37	7.7±0.5
	3.5×10^{16}	270	77	22.3±0.4	0.54	0.58±0.39	6.9±0.5
2.40	4.2×10^{14}	610	758	21.6±0.3	0.53	0.73±0.01	8.4±0.1
	6.5×10^{14}	455	555	23.3±0.1	0.53	0.64±0.08	7.9±0.1
	3.5×10^{16}	270	77	22.4±0.2	0.54	0.57±0.26	6.8±0.4
3.10	4.2×10^{14}	610	758	24.9±0.3	0.53	0.73±0.21	9.7±0.3
	6.5×10^{14}	455	555	24.4±0.2	0.54	0.68±0.23	9.0±0.3
	3.5×10^{16}	270	77	22.7±0.3	0.50	0.50±0.22	5.8±0.3
planar	4.2×10^{14}	610	758	18.9±0.3	0.53	0.76±0.04	7.6±0.1
	6.5×10^{14}	455	555	20.3±0.2	0.55	0.74±0.23	8.3±0.3
	3.5×10^{16}	270	77	17.9±0.2	0.55	0.62±0.04	6.1±0.1

recombination increases strongly. Hence, current is limited by photogenerated electrons. This effect is qualitatively illustrated in Figure 2.8.

To further illustrate this effect on the performance of the devices, the solar power conversion efficiencies were also measured under an AM 1.5G illumination, obtaining a maximum mean efficiency of 9.7%. All the results summarized in Table 2.1 were averaged over 4 samples fabricated under the same conditions. They show that both fill factor (FF) and efficiency (η) increase when decreasing the p–doping concentration. This enhancement could be explained by a decrease of the bulk recombination [57], as it demonstrates the EQE curves of the 3.1–μm–diameter nanowire arrays for the three different p–doping levels (Figure 2.7d). Clearly, long–wavelength photons, which are absorbed in the bulk, are collected more efficiently (*i.e.* recombination decreases) when the doping concentration of the substrate is lower. These measurements also suggest that the larger is the undepleted core, the higher is the short–circuit current density, presumably as a result of increased carrier collection. It should be noted that this statement can only be true as long as the distance from the center of the nanowire to the depletion region is smaller than the diffusion length of the minority carriers.

2.4.3 Variation on the Doping Concentration of the *n*–Shell

Next, the effect of the doping concentration and thickness of the shell was analyzed. In order to do so, the doping of the substrate was kept constant to 3.5×10^{16} cm^{-3} and the n–type doping was varied by diffusing $POCl_3$ at two different temperatures: 900 and 850°C. The measured and calculated n–doping profiles for these two cases are depicted in Figure 2.9a and 2.9b, respectively. As the diffusion of dopants increases with the temperature, the thickness of the shell in the case of a diffusion at 900°C is thicker (635 nm) than the one created with a diffusion

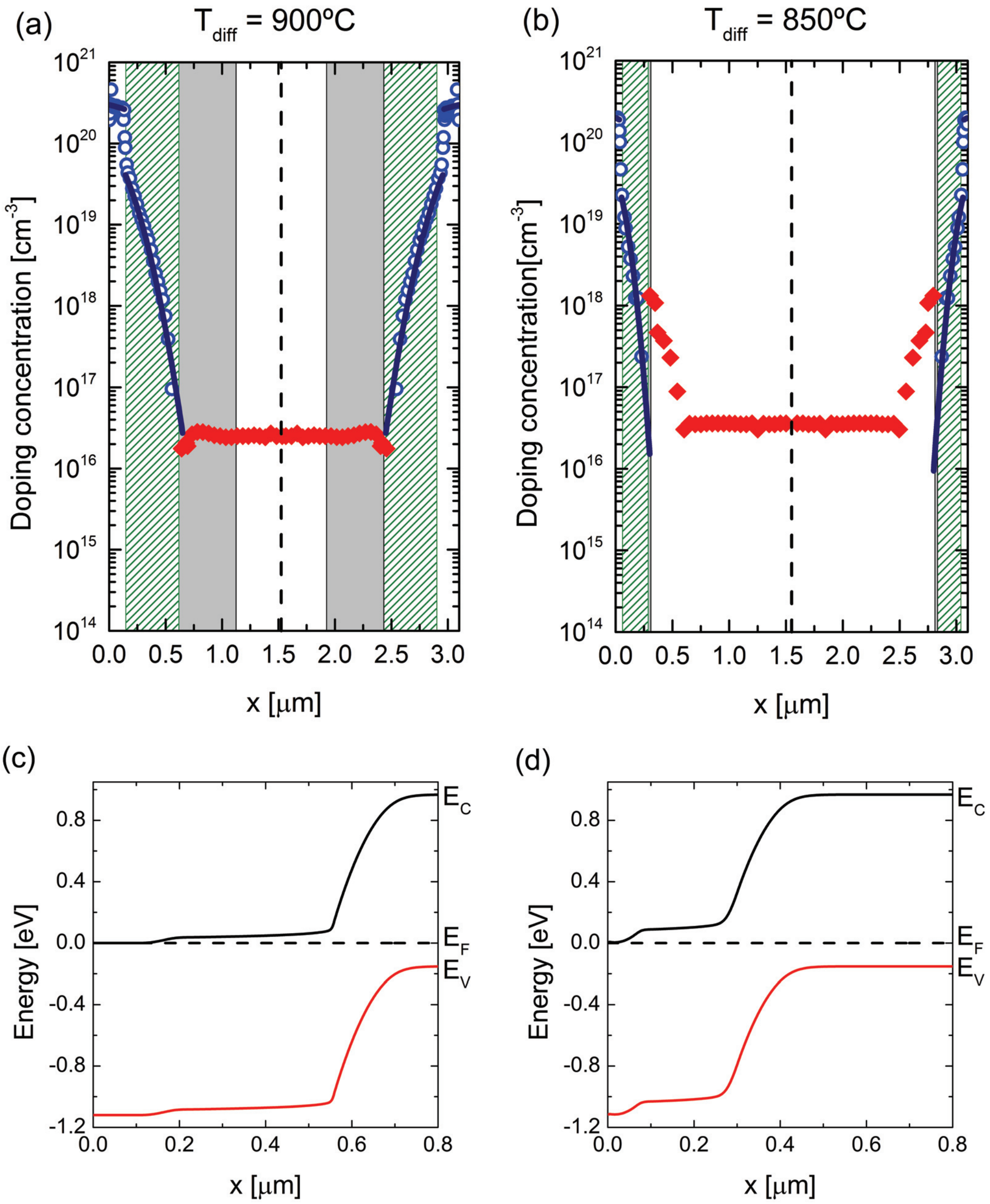

Figure 2.9: Doping profiles across the wire cross–section for a diffusion temperature of (a) 900°C and (b) 850°C. The symbols represent experimental measurements and the continuous lines show the simulated diffusion profiles. Vertical black lines define the position of the junction, grey areas represent depleted regions and shaded green areas depict the zone where the diffusion length of minority carriers is higher than the distance to the junction. Modeling of the band alignment at the junction for (c) T_{diff} =900°C and (d) T_{diff} =850°C.

at 850°C (270 nm). Logically, in the first case the doping concentration decreases less abruptly and this turns to a thicker depletion region (515 and 77 nm, respectively).

The gradual decrease of the doping concentration along the *n*–shell creates an internal electric field that pushes electrons towards the surface and holes to the core. However, looking at the doping profile of the 900°C diffusion sample we should note that it presents a plateau close to the surface, which suppresses any electric field in this zone and, as a consequence, it strongly enhances the carrier recombination via surface traps. Moreover, in order to evaluate the collection efficiency of photogenerated carriers, we need to take into account the diffusion lengths of minority carriers, which depend on the carrier concentration [58]. The diffusion length of holes at an electron concentration of $2 \times 10^{20}\mathrm{cm}^{-3}$ (doping concentration at the plateau) is around 200 nm. As the beginning of the depleted area is at a depth of 627 nm, the carriers generated at the surface recombine before reaching the junction. Shaded green areas in Figure 2.9a and 2.9b correspond to the regions where the photogenerated carriers can be efficiently collected. This area is noticeably closer to the microwire surface for the lower temperature diffusion (around 60 nm) than for the higher one (around 150 nm).

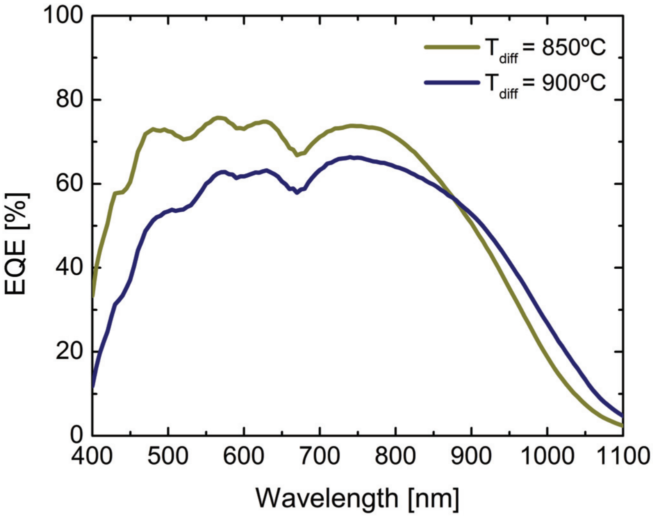

Figure 2.10: EQE characteristics of devices with P–diffused *n*–shells at 850 and 900°C.

If we compare the spectral dependence of the EQE of both devices (Figure 2.10) we can see that the cells obtained with a 900°C diffusion exhibit a lower EQE in a wider range of wavelengths, and especially in the visible regime. This result is in agreement with the existence of a doping concentration plateau next to the surface which benefits electron–hole pair recombination at the surface as a prevailing recombination mechanism. This translates into a 4.6% higher J_{sc} for cells with *n*–doped layers obtained by a 850°C diffusion (22.73±0.26 mA/cm^2) compared to those diffused at 900°C (21.73±0.21 mA/cm^2).

2.5 Conclusions

An easy and scalable top–down method has been used to fabricate silicon microwire radial *p*–*n* junction solar cells. Efficiencies up to 10.13% were achieved for 29 mm^2 devices. The ordered array of microwires demonstrated a good light trapping. The improvement was not only due to a gradual reduction of the effective refraction index but mainly thanks to an increase of the scattering path length when increasing the wire length. The radial junction configuration also led to an improvement of photogenerated carriers collection, especially at long wavelengths. This fact was proved by spectral response measurements. Nevertheless, the increase of surface and junction area induced an increase of recombination losses which resulted into a reduction of short–circuit current density and fill factor for the longest wires.

On the other hand, we have fabricated arrays with different *p*– and *n*–doping profiles and thicknesses. The results revealed the importance of scaling the microwire diameter with the depletion width resulting from *p*– and *n*–doping concentrations in order to ensure that neither the *n*– nor the *p*–doped regions are fully depleted. The doping of the core should be kept low in order to reduce bulk recombination and its radius should be smaller than the diffusion length of minority carriers (electrons in the case of a *p*–core). Furthermore, the thickness of the *n*–shell should be kept as thin as possible to limit the emitter losses and the doping concentration should be high enough to ensure a thin *n*–depleted area. Indeed, the best mean efficiency in this study was achieved by 3.1 μm diameter microwires, with a *p*–doping of $N_\mathrm{A} = 4.2 \times 10^{14}$ and a *n*–doping obtained by a diffusion at 850°C.

Future efforts could focus on improving light absorption, especially at long wavelengths, in order to reduce the need of long wires to absorb all the light and decrease, in this way, surface and junction recombination losses. Another important point to make these devices commercially attractive is to develop a procedure to contact microwire–arrays in a substrate–free mode. This would give rise to a more flexible device which could be introduced to other electronic systems and the remain substrate could be used again to fabricate new devices.

3 Surface Recombination on Silicon Nanowire–Based Solar Cells

Surface recombination losses represent a handicap for high–efficiency solar cells. These losses are especially important on nanowire array solar cells, where the surface–to–volume ratio is greatly enhanced. The impact of different passivation materials on the effective recombination and, as a consequence, on the device performance will be experimentally analyzed on axial *p–n* junction nanowires fabricated by means of a cost–effective and scalable technique called Near–Field Phase–Shift Lithography (NF–PSL).

Publications:

A. Dalmau Mallorquí, E. Alarcon–Lladó, I. Canales Mundet, A. Kiani, and A. Fontcuberta i Morral, *Field–Effect Passivation of Silicon Nanowire Solar Cells*, *in preparation.*

3.1 Introduction

Recombination in solar cells refers to the process in which electron–hole pairs are lost due to the decay of an excited electron to a lower energy state. This process can occur via different mechanisms: radiative, Auger and/or Shockley–Read–Hall (SRH) recombination. The first one is the recombination process which dominates in direct band gap semiconductors and it is a band–to–band transition followed by an energy release through the emission of a photon. Auger recombination is also a band–to–band decay but the energy released is transferred as kinetic energy to a third particle. It is important in highly doped materials, where interaction between carriers is more likely to occur. Finally, SRH recombination is the only process where trap states in the band gap are involved. In this case, energy is lost through a band–to–trap–state transition and it is usually a dominant mechanism as it is due to impurities or defects in the crystal structure.

The last one is the most important process as it involves defect states in the band gap. In real materials, defects and impurities concentrate at the surface and at the interfaces. These defects are mainly caused by a sharp interruption of the crystal lattice, which causes dangling bonds at the semiconductor surface or by structural imperfections at the interface between two different materials, causing vacancies or interstitial defects. The surface recombination rate per unit area, U_s, can be expressed as follows [9]:

$$U_\mathrm{s} = \frac{n_\mathrm{s} p_\mathrm{s} - n_\mathrm{i}^2}{\frac{1}{S_\mathrm{n}}(p_\mathrm{s} + p_\mathrm{t}) + \frac{1}{S_\mathrm{p}}(n_\mathrm{s} + n_\mathrm{t})}, \tag{3.1}$$

where n_s and p_s are the electron and hole densities at the surface, respectively, n_i is the intrinsic carrier density, and n_t and p_t are the electron and hole densities at the trap level. S_n and S_p are the surface recombination velocities for electrons and holes and are related to the density of interface defects, N_it, by,

$$S_\mathrm{n,p} = \sigma_\mathrm{n,p} v_\mathrm{th} N_\mathrm{it}, \tag{3.2}$$

being v_th the carrier thermal velocity and $\sigma_\mathrm{n,p}$ the capture cross–section for electrons and holes. Under relevant illumination and doping levels, it can be assumed that n_t, p_t and $n_\mathrm{i} \ll n_\mathrm{s}$ and p_s. Therefore, equation 3.1 can be simplified to [59]:

$$U_\mathrm{s} \approx \frac{n_\mathrm{s} p_\mathrm{s}}{\frac{p_\mathrm{s}}{S_\mathrm{n}} + \frac{n_\mathrm{s}}{S_\mathrm{p}}}. \tag{3.3}$$

From equation 3.3 we can see that there are two ways of reducing U_s: by decreasing S_n and S_p (or, what is the same, by decreasing N_it) or by decreasing the density of one type of carrier at the surface, n_s or p_s, by introducing a built–in electric field. The first way is called *chemical passivation* and the second one, *field–effect passivation*.

The recombination rate reaches its maximum when $p_\mathrm{s}/n_\mathrm{s} \approx \sigma_\mathrm{n}/\sigma_\mathrm{p}$ [60]. Assuming identical capture cross–sections for electrons and holes, the highest recombination rate is achieved for $p_s \approx n_s$. Thus, the field–effect passivation is based on the reduction of the concentration of one type of carrier at the interface by means of an electric field induced by the presence of fixed electrical charges at the semiconductor interface.

The effective lifetime is determined by the sum of bulk (including Auger, radiative and Shockley–Read–Hall recombinations) and surface recombination processes:

$$\frac{1}{\tau_{\mathrm{eff}}} = \frac{1}{\tau_{\mathrm{SRH}}} + \frac{1}{\tau_{\mathrm{Auger}}} + \frac{1}{\tau_{\mathrm{rad}}} + \frac{1}{\tau_{\mathrm{surf}}}. \tag{3.4}$$

From equation 3.4, we can deduce that surface recombination will dominate when bulk recombination is low.

Surface Recombination on Nanowires

Surface recombination is a major concern for nanowire array solar cells due to their high surface–to–volume ratio. Their photovoltaic performance is seriously reduced by the presence of surface dangling bonds, which are shown to trap the impurities and electronically neutralize them [61]. It has been experimentally demonstrated that by reducing the surface recombination by almost two orders of magnitude the light absorption cross–section of the wire increases for a broad range of wavelengths and its photosensitivity enhances 90–fold when used as a photodetector [62]. It has also been shown that minority carriers lifetime is controlled by the surface recombination and strongly depends on the nanowire diameter [63].

The reduction in the surface recombination (SR) rate of nanowire–based solar cells results in an increase of open–circuit voltage, short–circuit current and efficiency [64]. However, the effect of the SR rate strongly depends on the junction configuration. Yu *et al.* simulated the impact of surface recombination velocity on both axial and radial *p–n* junction nanowire arrays [50]. They concluded that the recombination rate at the surface for the same doping level is higher in the axial configuration than in the radial one. In the radial configuration, minority carriers from the shell diffuse towards the junction, reducing the density of carriers close to the surface and, hence, the recombination. Nevertheless, in the axial configuration the carrier concentration at the surface is the same as in the bulk, giving rise to a higher recombination rate.

Among the many different materials investigated for passivation purposes, thermal SiO_2 [65], a–SiN_x:H [66] or Al_2O_3 [67] are some of the most widely used. We have studied experimentally the effect of these materials on the surface passivation of axial *p–n* junction Si nanowires. To this end, ordered arrays of nanowires were fabricated by Near–Field Phase–Shift Lithography, a photolithographic–based technique that allows to obtain submicron structures by manipulating the incident light. The interface between the silicon and the passivation material and their passivation properties were analyzed as well as their influence on the photoconversion efficiency.

3.2 Near–Field Phase–Shift Lithography

In order to study the impact of surface recombination on the device performance, we wanted to use thinner wires with an axial junction. As the goal was to analyze large area devices (4 × 4 mm^2) ebeam lithography was not an appropriate solution to define the nanowires as it is a time–consuming and expensive technique. Thus, we looked for an alternative method.

For the past three decades, optical lithography has been the patterning method used by the semiconductor industry. It combines a relatively high resolution with a low production cost and an easy integration to the production chain. However, the increasing density of component devices on a chip pushed the resolution limits beyond the photolithographic limits. To overcome this problem new techniques have been developed, such as nanoimprint lithography, electron beam lithography [68], nanosphere lithography [69], laser interference lithography [70], focused ion beam lithography [71] or other template–assisted patterning [72]. The approach presented in this chapter is based on conventional photolithography but it manipulates the incident light by incorporating a grating in the lithographic mask. Such technique has already been successfully used to fabricate nanochannels [73], nanoneedles, holes or boxlike structures [74].

The resolution limit, *R*, and the corresponding depth of focus, *DOF*, in standard photolithography is determined by the Rayleigh's equation:

$$R = \frac{k_1 \cdot \lambda}{NA}, \tag{3.5}$$

$$DOF = \frac{k_2 \cdot \lambda}{NA^2}, \tag{3.6}$$

where k_1 and k_2 are constants that depend on the resist material, image formation technique and process technology, λ is the incident wavelength and *NA* is the numerical aperture of the optical system, which is related to the half–angle of the maximum cone of incident light. Hence, to obtain higher resolutions, shorter light wavelengths and lens systems with larger numerical apertures can be used. To overcome this issue, industry moved towards the use of deep ultraviolet light excimer lamps (typical wavelengths of 248 or 193 nm), which requires changes in the lithography equipment as the absorption characteristics of materials change. On the other hand, when using high–NA lens systems, the depth of focus is largely reduced and the exposure becomes very sensitive to the absolute position and variations in the thickness of the resist.

In order to enhance the resolution, several techniques have been proposed by manipulating the wavefront of the incident light. This can be done by either phase shifting the wavefront in the mask plane or filtering the incident light obtaining an off–axis illumination. In both cases,

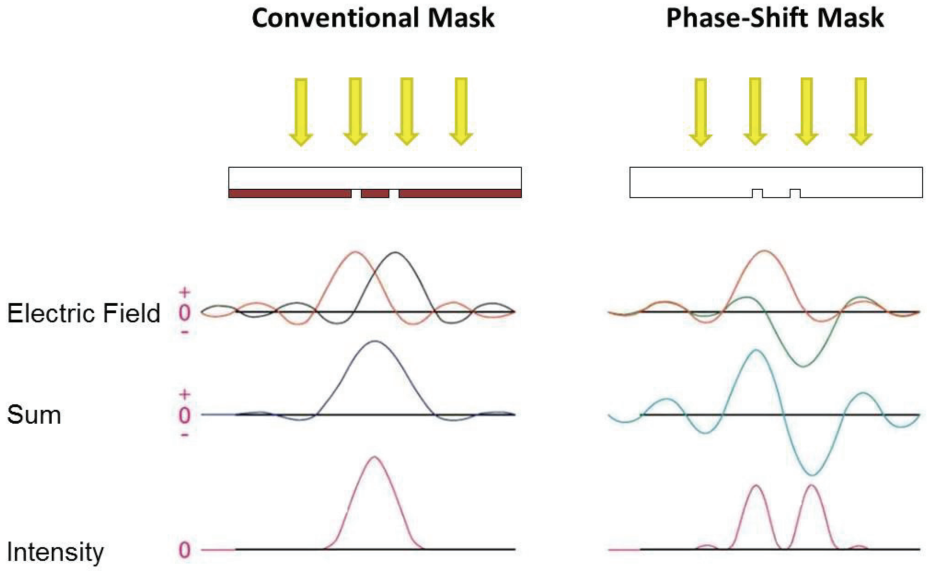

Figure 3.1: Principle of phase–shifting masks. Comparison of the diffracting optics of (a) a conventional mask and (b) an alternating PSM mask which introduces a phase–shift grating (adapted from [75]).

the zeroth–order light is cancelled out and the diffraction angle of the first–order rays halved, doubling the spatial frequency of the images that can be resolved ($\lambda/2$) [76]. The images of two neighboring apertures are resolved when the intensity in the region between their images presents a minima. Constructive interference between waves diffracted by adjacent apertures enhances the electric field between them. As the intensity is proportional to the square of the electric field, this yields to a reduction of the resolution. By adding a relief or phase–shift step, the waves transmitted through adjacent apertures are 180° out of phase with one another, canceling out the intensity between them (Figure 3.1). This effect gives rise to a higher resolution and contrast [77].

Wang *et al.* theoretically analyzed electromagnetic absorption in a photoresist layer employed in near–field phase–shift lithography [78]. They calculated the specific absorption rate (SAR) to characterize the columnar features produced within the photoresist by a periodical array of microchannels. They concluded that broadband UV illumination produces a better resolution and profile of columnar features than monochromatic light. They also studied the effect of the dimensions of the mask pattern on the SAR distribution in the photoresist layer. According to their calculations, large values of period (>4 μm) and a channel width of about half the period are needed to obtain high aspect–ratio photoresist features. Finally, they analyzed the effect of the phase–shift step height and the results indicated a better output for steps ranging from 400 to 500 nm.

The effect of the height of the phase–shift step is mostly related to the near–field effect. If the depth of surface relief of a phase–shift mask shifts the phase by an odd multiple of π, then the intensity in the near field of the mask is reduced to zero at every phase edge. When the shift deviates from this value, the depth of the intensity modulation decreases [79].

3.3 Experimental Techniques: QssPC Measurements

There exist many techniques to determine the surface recombination rate in solar cells. The minority carriers lifetime, τ_{eff} is often obtained by dynamic methods such as photoconductance decay (PCD) or open–circuit voltage decay (OCVD). In both cases the illumination is abruptly interrupted and the time–dependent decay of photoconductance or voltage, respectively, is analyzed. However, the time decay strongly depends on the depletion layer and diffusion capacitances [80]. This problem can be overcome by using quasi–steady–state (Qss) techniques, whose basis is to vary the illumination intensity at a slower speed than the minority carrier lifetime in order to have the device in almost steady–state conditions. Again, this method can be applied to measure the photoconductance (QssPC) or the open–circuit voltage (QssV$_{\mathrm{oc}}$).

In our case, we used the photoconductance technique to obtain the carriers lifetime. QssPC measurements were carried out by means of a WCT–100 photoconductance setup from Sinton Instruments. It consists of an inductive coil that converts the current produced by the excited carriers into a voltage signal which is coupled to the conductivity of the wafer [81]. The photoconductivity decay with the flashlamp intensity decay is measured. A flashlamp with a decay time of 2 ms was used. The minimum lifetime that can be measured is 3 μs.

The carrier density decay over time can be calculated from the measured photoconductivity, σ, since

$$\sigma = n\, q\, \mu, \tag{3.7}$$

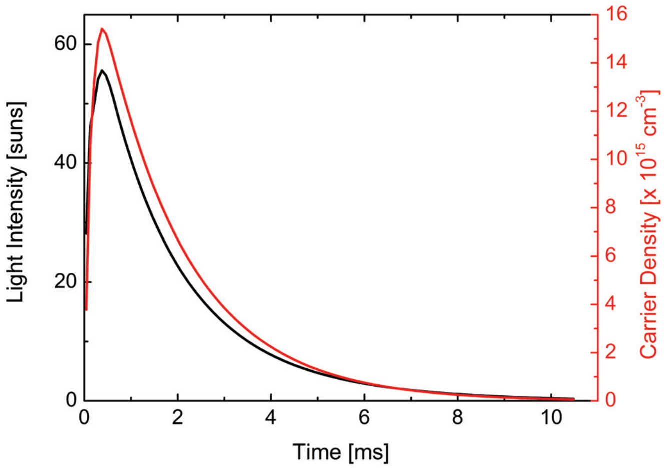

Figure 3.2: Illumination and carrier density time decay extracted from QssPC measurements.

where μ is the carrier mobility and n the carrier density. Figure 3.2 shows the carrier density (red line) and flashlamp intensity time (black line) decays.

The effective lifetime is related to the excess carrier density by the following expression:

$$\tau = \Delta n / U, \tag{3.8}$$

where Δn is the excess minority carrier density calculated from the measured photoconductivity and U is the recombination rate. U can be determined from the excess minority carriers decay by:

$$\frac{\partial \Delta n}{\partial t} = G - U + \frac{1}{q}\frac{\mathrm{d}J_\mathrm{n}}{\mathrm{d}x}, \tag{3.9}$$

where G is the generation rate and J_n is the current density of minority carriers through the sample width, x. At open–circuit conditions the last term disappears. Then, the effective lifetime can be extracted and related to the excess carrier density by merging equations 3.8 and 3.9 [82],

$$\tau_\mathrm{eff} = \frac{\Delta n}{G - \frac{\partial \Delta n}{\partial t}}. \tag{3.10}$$

Figure 3.3 depicts the effective lifetime dependence over the excess carrier density for the sample covered by the SiO_2/SiN_x bilayer. As it can be observed, τ_eff depends on the carrier injection level: it increases for low density of excess carriers reaching its maximum in the vicinity of the doping concentration and then it decreases at high injection levels. For a single–point value, we consider the lifetime obtained at an injection level of 10^{15} cm^{-3} as it is used for the majority of the reported data and it has a good signal–to–noise ratio.

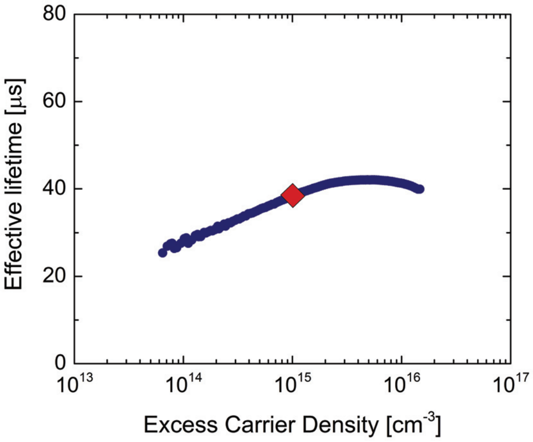

Figure 3.3: Effective lifetime versus excess carrier density for a p–doped Si wafer coated with a bilayer of 52 nm of SiO_2 and 19 nm of SiN_x. The red symbol depicts the specified injection level.

3.4 Sample Preparation

To better study the surface passivation properties of different materials and their effect on the solar cell performance, axial *p–n* junction nanowires were fabricated by means of a two–step near–field contact phase–shift lithography as reported elsewhere [74]. Large arrays of square–arranged submicron wires were obtained with this technique. For this purpose, a fused silica mask with 2–μm wide trenches with a fix period of 4 μm was first fabricated.

3.4.1 Mask Fabrication

A key issue to increase the resolution of NFC–PSL is to fabricate a grating mask with very sharp phase edges. This leads to a higher and narrower peak of the intensity profile. For this reason, electron beam lithography was used to write the design on the phase–shift mask, as it provides higher resolution than other techniques. For the same reason, fused silica was the material chosen for the mask. Its high purity results in vertical and sharp sidewalls after etching.

In order to avoid electrostatic charging during electron beam lithography, a layer of 100 and 350 nm of aluminum was sputtered on the front and back side of the mask, respectively. 150 nm of ZEP520A resist (consisting on 11% methyl styrene and chloromethyl acrylate copolymer and 89% anisole), diluted 50% in anisole was spin–coated before performing electron beam lithography. Following the indications of Wang *et al.* [78], arrays of 4×4 mm^2 were patterned with 2–μm wide trenches spaced 4μm. After development, resist–free aluminium regions were exposed for 20 s to induced coupled plasma etching using Cl_2/BCl_3 gas mixture (STS Multiplex ICP). Afterwards, a long O_2 plasma strip was performed to completely remove all the ZEP resist. Then, and using the aluminium layer as hard mask, the pattern was transferred to the fused silica substrate by means of a C_4F_8/CH_4 plasma etching for 130 s, leading to a groove depth of 500 nm. Finally, aluminium was stripped off by an aluminium etchant ANP (H_3PO_4 (85%) + CH_3COOH (100%) + HNO_3 (70%) + H_2O, 83:5:5:5) dip of around 30 min.

3.4.2 Nanowire Arrays Fabrication

380–μm thick Czochralski <100> *p*–doped Si wafers with a resistivity of 1–10 $\Omega\cdot$cm and covered by a 200–nm thermal oxide layer were used. Prior to the fabrication of the nanowires, a front–side diffusion doping was carried out. In order to do so, the back side was coated with a thick photoresist to prevent SiO_2 etching and the front oxide was stripped off by a buffered HF dip. Once the front side was oxide–freed, the photoresist was removed. The *n*–emitter was formed by diffusing $POCl_3$ for 15 min at a temperature of 950°C, while the back–side oxide was used as a diffusion barrier (Figure 3.4a). Right after the diffusion, the surface was again exposed to buffered HF to remove the oxide. The steps carried out to fabricate the Si nanowire arrays are depicted in Figure 3.4.

A first standard photolithography step was carried out to design the alignment marks, required

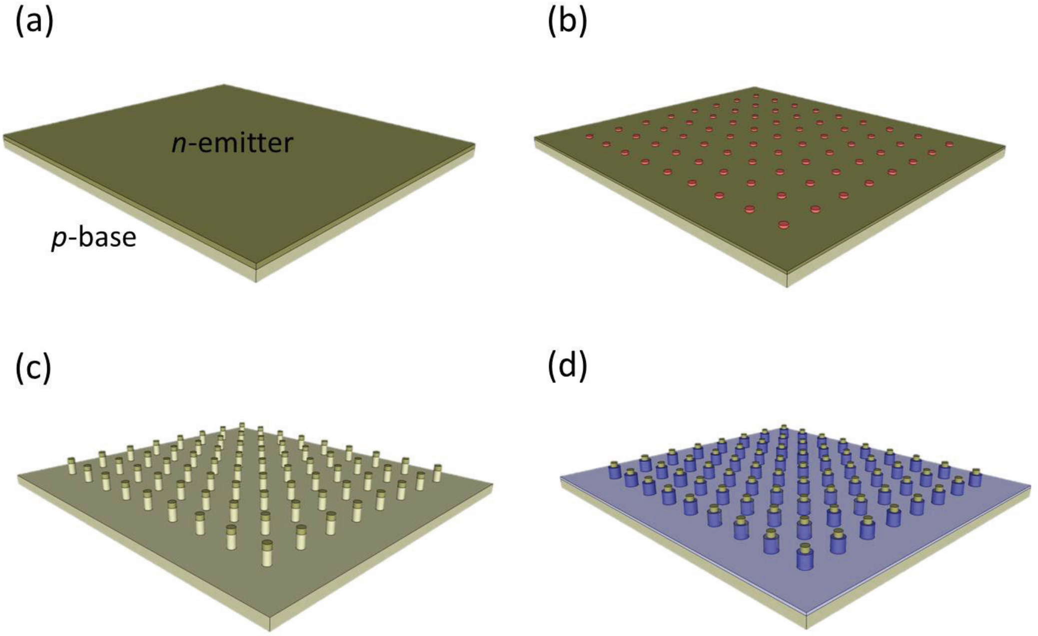

Figure 3.4: Schematic of the fabrication of axial *p*–*n* junction nanowires by PSL: (a) $POCl_3$ diffusion at 950°C; (b) double–step PSL to obtain 500–nm–diameter dots; (c) reactive ion etching; and (d) after the deposition of a passivation layer all around the wires, selective removal of it by using a polymer–infill etch mask.

to correctly align the substrate and the mask when rotating the mask 90° between the first and the second NFC–PSL steps. In order to do so, the Si wafer was coated by 1.1 μm of AZ1512H photoresist and exposed for 1.6 s. Silicon was etched for 2 min in wet etchant (HNO_3 (70%) + HF (49%) + H_2O, 5:3:20). Photoresist was removed by exposing the wafer under plasma O_2.

After coating the wafer with 650 nm of AZ ECI 3007 positive photoresist, it was exposed for 1.4 s under UV broad band light (Hg light source UV400: g, h, i–line) with a power intensity of 10 mW/cm^2. This step was repeated after rotating the mask 90°. The first exposure led to an array of stripes aligned following the X axis, while the second one defined the same array of stripes in the perpendicular direction. The array of dots were determined at the intersection between the stripes. The two exposures were done consecutively and afterwards the photoresist was developed as proceeding in a standard photolithography. For this double–step lithography, a vacuum contact between the mask and the wafer was required in order to ensure a good and uniform contact. Figure 3.5 depicts the different steps of the double–step NF–PSL. Nanowires with a diameter of 600 nm were obtained with this technique.

The PSL pattern was transferred to the silicon substrate by means of reactive ion etching (SF_6 (40 sccm)/C_4F_8 (55 sccm) gas mixure) for 4 min and, subsequently, the remaining photoresist was removed. This etching time led to a pillar height of around 2 μm (Figure 3.4c).

Then, and to electrically insulate the base from the front contact, an oxide barrier was de-

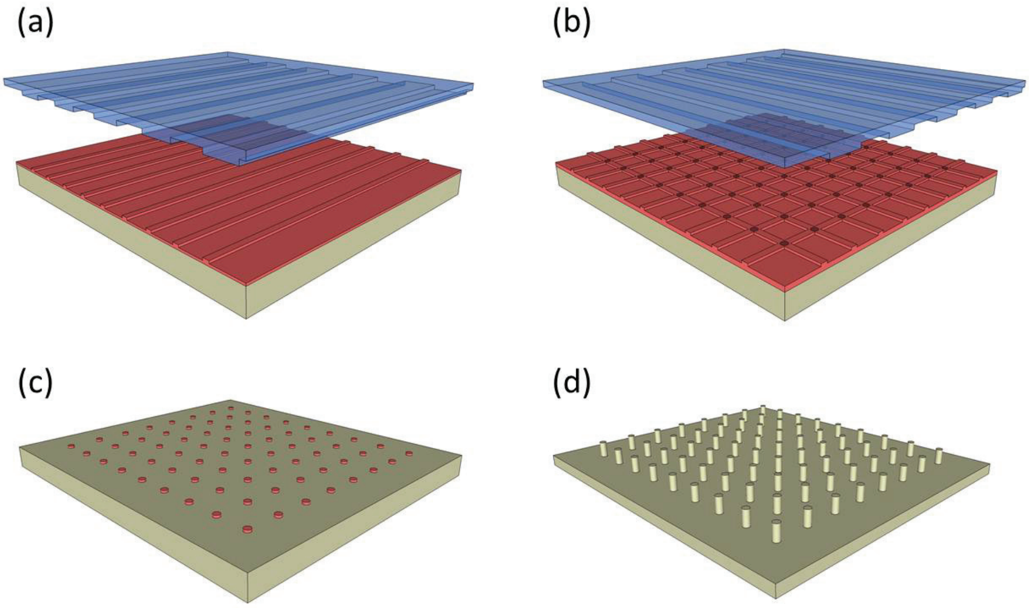

Figure 3.5: Double–step phase–shift lithography procedure: (a) first exposure, (b) second exposure rotating the mask 90° and (c) developing. The dots are defined at the intersection between the two stripe arrays. (d) The pattern is transferred to the Si substrate by means of a reactive ion etching.

posited all over the front surface. Besides, this layer should also passivate the surface. For this purpose, four different materials were tested: (i) Al_2O_3 deposited by atomic layer deposition (ALD, Beneq TFS200) using trimethylaluminum (TMA) as the precursor and H_2O as the oxidant at 200°C; (ii) SiO_2 thermally grown at 950°C in oxygen gas followed by a nitrogen anneal at the same temperature; (iii) a–SiN_x:H deposited by plasma enhanced chemical vapour deposition (Oxford PlasmaLab 100 PECVD) at a temperature of 300°C, a pressure of 800 mTorr and a gas mixture of 2% SiH_4/N_2 = 1000 sccm and NH_3 = 15 sccm; and (iv) a bilayer of thermally–grown–SiO_2/PECVD–SiN_x.

In order to free the *n*–doped tip of the pillars from any insulating barrier, a partial etching was required. For this goal, the pillars were embedded in a photoresist matrix (AZ ECI 3027). A thick film of 3100 nm of photoresist was spin–coated at 3000 rpm for 1 min and post–baked at 120°C for 5 min. Afterwards, the polymer layer was etched down to a final thickness of 1800±100 nm by means of an O_2 Induced Coupled Plasma etching (ICP). A controlled etch was achieved by using an electrostatic chuck power of 100 W and an ICP source power of 600 W. The controllability of the polymer etching is important to avoid a short–circuit between the front contact and the *p*–doped base. In this case, as the junction depth is around 1.2 μm and the pillar height of about 2 μm, a final polymer thickness of 1.3 μm was achieved. The polymer–free part of the pillars was etched by dipping the sample in BHF 7:1 solution for 20 or 50 s, depending on the thickness and nature of the oxide (Figure 3.4d). Figure 3.6 shows the doping profile within the nanowire and the passivation layer height. A last O_2 plasma removal was carried out to clean the sample from any polymer residue. Finally, 200 nm of aluminum were sputtered on the backside and 500 nm of ITO on the front side. On top of the ITO, a layer of 10 nm of Ti and 100 nm of Au was evaporated through a metallic mask all around the arrays. 12 devices of 16 mm^2 were prepared for each passivation material. A SEM image of the final device is shown in Figure 3.7.

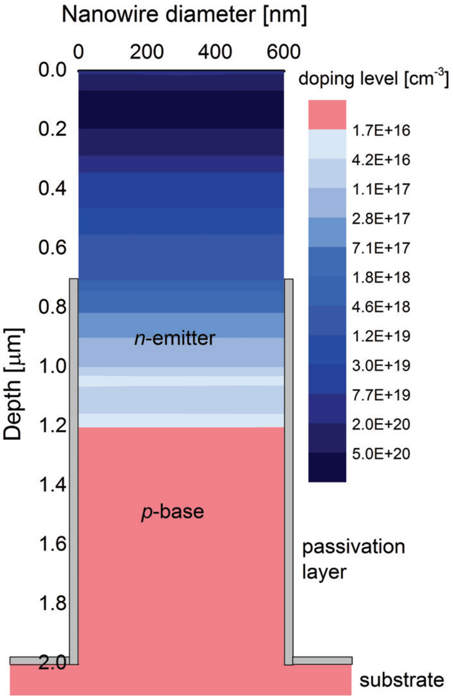

Figure 3.6: Doping profile of the axial junction within the nanowire. The grey regions on both sides of the nanowire represent the passivation layer.

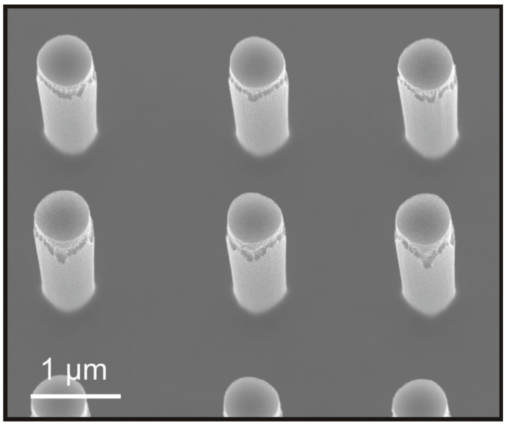

Figure 3.7: SEM image tilted 25° of PSL–fabricated nanowires. The diameter of the wires is approximately 600 nm.

3.5 Results

The current–voltage characteristics of NF–PSL nanowire–based solar cells passivated with the four different materials were measured under illumination conditions of AM 1.5G and are showed in Figure 3.8. As predicted elsewhere [50], surface recombination on axial *p–n* junction nanowire arrays have a significant impact on both short–circuit current density (J_{sc}) and open–circuit voltage (V_{oc}). Comparing the four curves, it can be observed that the devices passivated with SiN_x and Al_2O_3 have similar open–circuit voltages (V_{oc}) and short–circuit current densities (J_{sc}), yielding to efficiencies (η) of 3.4 and 2.4%, respectively. On the other hand, it is well–known that thermally grown SiO_2 leads to a high quality interface and reduced surface recombination. Unexpectedly, the device passivated with thermal SiO_2 reports the worst results (J_{sc} = 11.3 mA/cm^2, V_{oc} = 0.22 V and η = 1.2%). However, the addition of the outermost 19–nm–thick SiN_x layer greatly enhances the photovoltaic properties of the device: J_{sc} = 28.4 mA/cm^2, V_{oc} = 0.52 V, FF = 0.67 and η = 9.9%.

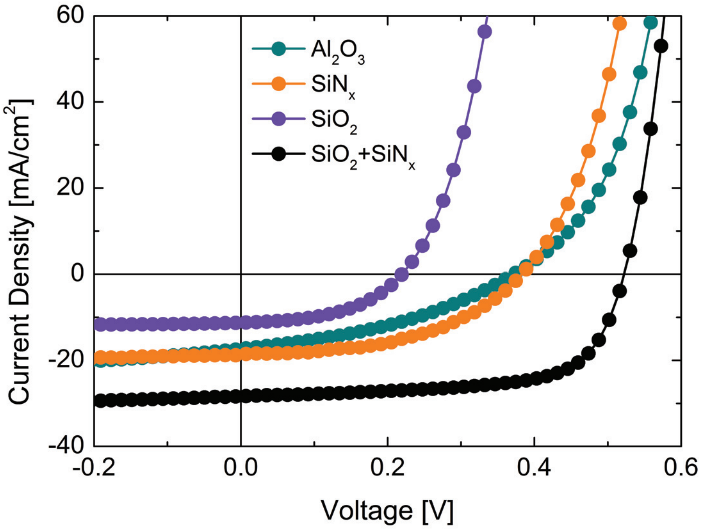

Figure 3.8: Current–voltage characteristics under AM 1.5G illumination of the nanowire arrays covered with Al_2O_3, SiN_x, SiO_2 and a SiO_2/SiN_x bilayer.

In order to understand the bad performance of the SiO_2–coated solar cell and the reason for the great improvement when adding a SiN_x layer, the carrier lifetime of the different samples were measured by means of QssPC. For these measurements a 1–10 Ω·cm *p*–type Si wafer was etched down from both sides with reactive ion etching in order to have the same surface roughness as on the nanowire sidewalls. The passivation layer was also deposited onto both sides. The measured lifetimes are summarized in Table 3.1, together with the photovoltaic characteristics. The diffusion length, L, and surface recombination velocity, S_{eff}, are calculated by the following expressions:

$$L = \sqrt{\tau_{eff}\, D} \qquad \text{and} \qquad \frac{1}{\tau_{eff}} = \frac{1}{\tau_{bulk}} + \frac{2S_{eff}}{W},$$

where D is the carrier diffusivity ($D = 34.41$ cm^2/s for a doping level $N_A = 10^{15}$ cm^{-3} [83]) and W is the wafer thickness ($W = 380$ μm). Considering that $\tau_{\text{bulk}} \gg \tau_{\text{surf}}$,

$$\frac{1}{\tau_{\text{eff}}} \approx \frac{2S_{\text{eff}}}{W}. \tag{3.11}$$

Based on QssPC results, thermal SiO_2 presents the best level of surface passivation, as it leads to the highest lifetime ($\tau_{\text{eff}} = 46$ μs), followed by the SiO_2/SiN_x bilayer, SiN_x and Al_2O_3. Nonetheless, these values do not result in a better solar cell performance. Photovoltaic properties and lifetimes for all the samples are summarized in Table 3.1.

Table 3.1: Solar cell characteristics and passivation qualities with respect to the passivation layer.

Passivating material	film thickness (nm)	τ_{eff} (μs)	S_{eff} (cm/s)	L_{eff} (μm)	J_{sc} (mA/cm^2)	V_{oc} (V)	FF	η (%)
Al_2O_3	44	13	1462	212	17.4	0.37	0.38	2.4
SiN_x	52	19	1000	257	18.7	0.38	0.48	3.4
SiO_2	48	46	413	398	11.3	0.22	0.48	1.2
SiO_2/SiN_x	52/19	38	500	362	28.4	0.52	0.67	9.9

In order to shed light in the difference between SiN_x, SiO_2 and SiO_2/SiN_x passivations, an analysis of the chemical composition of the interface between the Si substrate and the passivation layer was carried out by Fourier transformation infrared (FTIR) spectroscopy using the attenuated total reflection (ATR) mode. FTIR absorption spectra were measured with 6700 Nicolet, Thermo Fisher Scientific with a resolution of 1 cm^{-1}. From FTIR measurements, information of the different bonding densities at the interface are obtained, which can be linked to chemical and/or field–effect passivation. In Figure 3.9 the spectra of Si–SiO_2, Si–SiN_x and the bilayer Si–SiO_2/SiN_x are compared.

The SiN_x film presents several peaks around 840, 2160 and 3340 cm^{-1} resulting from the Si–N, Si–H and N–H bonds, respectively. The Si–H stretching bond can be deconvoluted into six Gaussian peaks: H–Si–Si_3 around 2000 cm^{-1}, H–Si–HSi_2 around 2060 cm^{-1}, H–Si–NSi_2 around 2100 cm^{-1}, H–Si–SiN_2 and H–Si–SiNH around 2140 cm^{-1}, H–Si–HN_2 around 2170 cm^{-1} and H–Si–N_3 around 2220 cm^{-1}. Mäckel and Lüdemann related the N–H bond concentration to the formation of the •Si≡N_3 dangling bond, the so–called K^+ center which leads to a fixed positive charge density, Q_f, of the order of 10^{12} cm^{-2} [84].

Thermally grown SiO_2 spectrum exhibits the characteristic peaks at 810, 1060 and 1250 cm^{-1} corresponding to the vibrational bending, and TO and LO modes of the stretching bands of Si–O–Si, respectively [65]. Thermal SiO_2 provides a high level of chemical passivation on Si surfaces due to its low interface defect density (~ 10^{10} cm^{-2}). The trivalently bonded Si atom (•Si≡Si_3), known as P_b center, is the main defect at Si/SiO_2 interfaces due to a lattice mismatch. These defects lead to positive Q_f of the order of 10^{10} cm^{-2} [85] and could be passivated by a

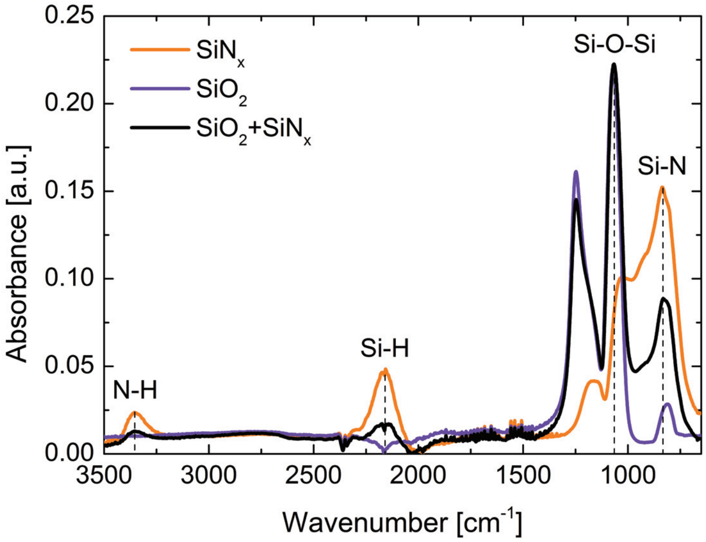

Figure 3.9: FTIR spectra of the Si/SiN$_x$, Si/SiO$_2$ and Si/SiO$_2$+SiN$_x$ interfaces.

hydrogen post–treatment. For instance, the addition of a hydrogen–containing capping layer results in a hydrogen passivation of the interface, which is corroborated by the Si–H signal at 2160 cm^{-1} of the SiO$_2$/SiN$_x$ spectra. Moreover, the addition of the SiO$_2$ interlayer between Si and SiN$_x$ reduces significantly the concentration of Si–N bonds in comparison with the Si/SiN$_x$ interface. Both effects result in no field–effect passivation induction by the SiO$_2$/SiN$_x$ stack [86].

On the other hand, the FTIR spectra of the Al$_2$O$_3$ film shown in Figure 3.10 exhibits the

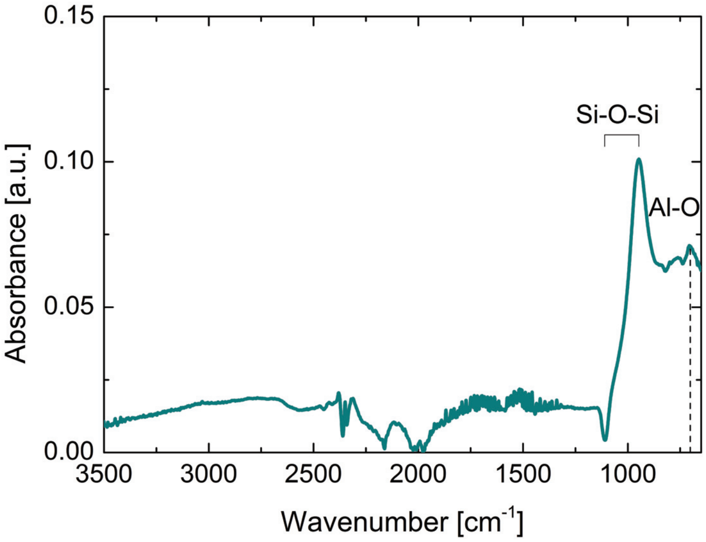

Figure 3.10: FTIR spectrum of the Si/Al$_2$O$_3$ interface.

characteristic Al–O absorption peak at 704 cm^{-1}. A thin SiO$_x$ interlayer formed during the deposition process is confirmed by the broad peak at 940–1100 cm^{-1} [87]. Hoex *et al.* suggested that this interfacial layer could induce a high density of Al vacancies at the interface [67]. Some theoretical studies have concluded that Al vacancies and O interstitial can be charged negatively [88], leading to negative Q_f values in the range of 10^{12}–10^{13} cm^{-2}.

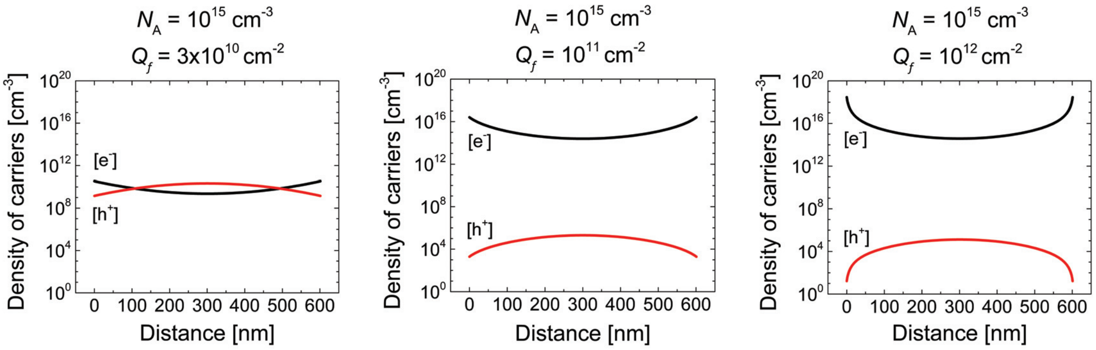

Figure 3.11: Carrier density profile across the *p*–doped Si nanowire cross–section (N_A = 10^{15} cm^{-3}) under the influence of a positive fixed charge of $Q_f = 3 \times 10^{10}$, 10^{11} and 10^{12} cm^{-2}. Black lines show the evolution of hole density with Q_f and red lines depict electron density.

The effect of the presence of fixed charges at the silicon/insulator interface of the nanowire sidewall was investigated with next**nano**^{3} [89]. Figure 3.11 illustrates the density profiles of electrons and holes across the wire cross–section for a positive fixed charge of $Q_f = 3 \times 10^{10}$, 10^{11} and 10^{12} cm^{-2} calculated for a nanowire of 600 nm of diameter and a doping concentration of $N_\mathrm{A} = 10^{15}$ cm^{-3} [89]. The positive charge creates an electric field that attracts electrons towards the surface and pushes holes away from it. The low *p*–doping concentration and small diameter of the nanowires give rise to completely inverted conditions for high Q_f values (≥ 10^{11} cm^{-2}): electrons become majority carriers while holes get reduced to minority carriers within the whole nanowire cross–section. In such cases, the junction will be shifted to the base of the nanowire. Nevertheless, for $Q_f = 3 \times 10^{10}$ cm^{-2} the electron and hole densities become equal at some point inside the nanowire cross–section ($p = n$), resulting in an increase of recombination at the core of the wire. These results could explain the poor performance of devices passivated with SiO$_2$. As mentioned above, Si/SiO$_2$ interfaces have low density of defects which leads to reduced densities of fixed charges. On the other hand, the high density of fixed charges introduced by the Si/SiN$_x$ interface results in a *n*–doped–like nanowire and the junction is moved to the base of the wire.

The negative nature of the fixed charges in the Si–Al$_2$O$_3$ system gives rise to a different outcome. At the *p*–region of the wire, the fixed charges create an electric field that shields electrons from the surface. However, since the Al$_2$O$_3$ layer partially covers the *n*–doped region of the wire, an inversion occurs at this point. Figure 3.12 demonstrates the impact of a -10^{12} cm^{-2} fixed charge on a *n*–doped region with a doping concentration of $N_\mathrm{D} = 10^{16}$ cm^{-3}. It can be observed that again the inversion of electron and hole densities leads to an equal concentration of both carriers within the nanowire core, resulting in an enhancement of the recombination at this

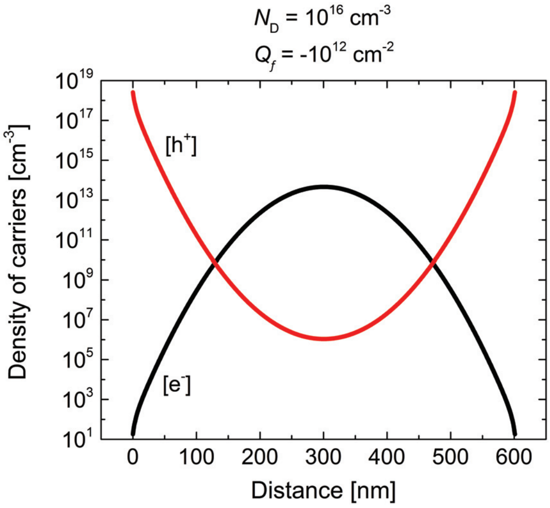

Figure 3.12: Electron and hole densities at the n–doped nanowire cross–section ($N_\mathrm{D} = 10^{16}$ cm^{-3}) under the influence of a negative fixed charge of $Q_f = -10^{12}$.

region of the wire. Figure 3.13 qualitatively illustrates the change on the carrier concentration along the wire for the four different cases.

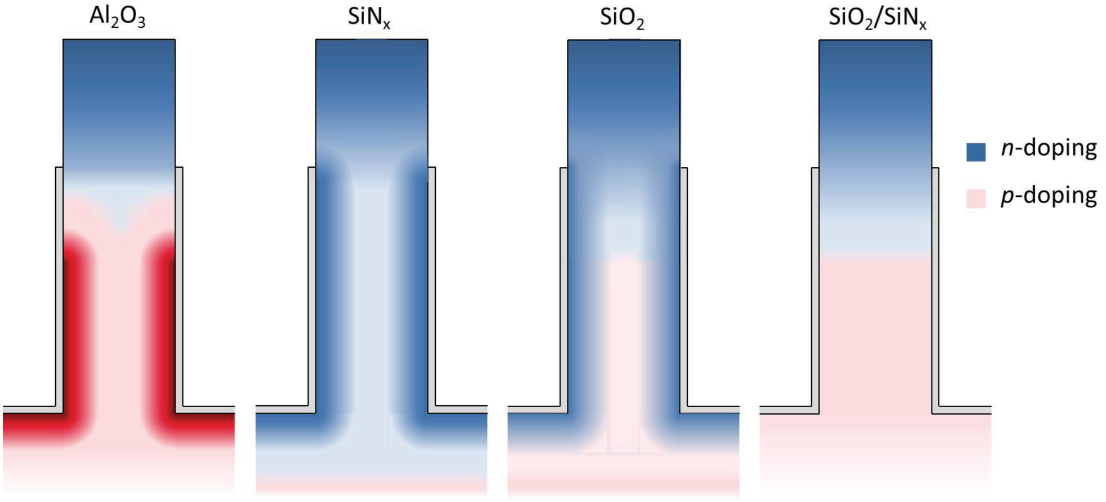

Figure 3.13: Qualitative illustration of the carrier density profile across the nanowire under the influence of interface fixed charges induced by the different passivation materials. Bluish and reddish areas depict n–doped and p–doped regions, respectively.

Finally, the light absorption in the device was calculated by Finite Difference Time–Domain (FDTD) simulations [90] reaching steady–state conditions. The incoming light was modeled as a plane wave polarized along the x–direction with an incidence normal to the structure. The calculations were realized for an array of Si nanowires with a diameter of 600 nm, a length and pitch of 2μm, a passivation layer of 50 nm of silicon dioxide covering the substrate and nanowire sidewalls up to a height of 1.5 μm and a layer of 400 nm of ITO as front electrode.

Figure 3.14 depicts the electric field energy density along the wire (at x= 0 and y= 0) and within the wire cross–section at 400 nm below the junction respectively, at 400, 600, 800 and 1000 nm. From the vertical cross–section, it can be observed that light is mainly absorbed within

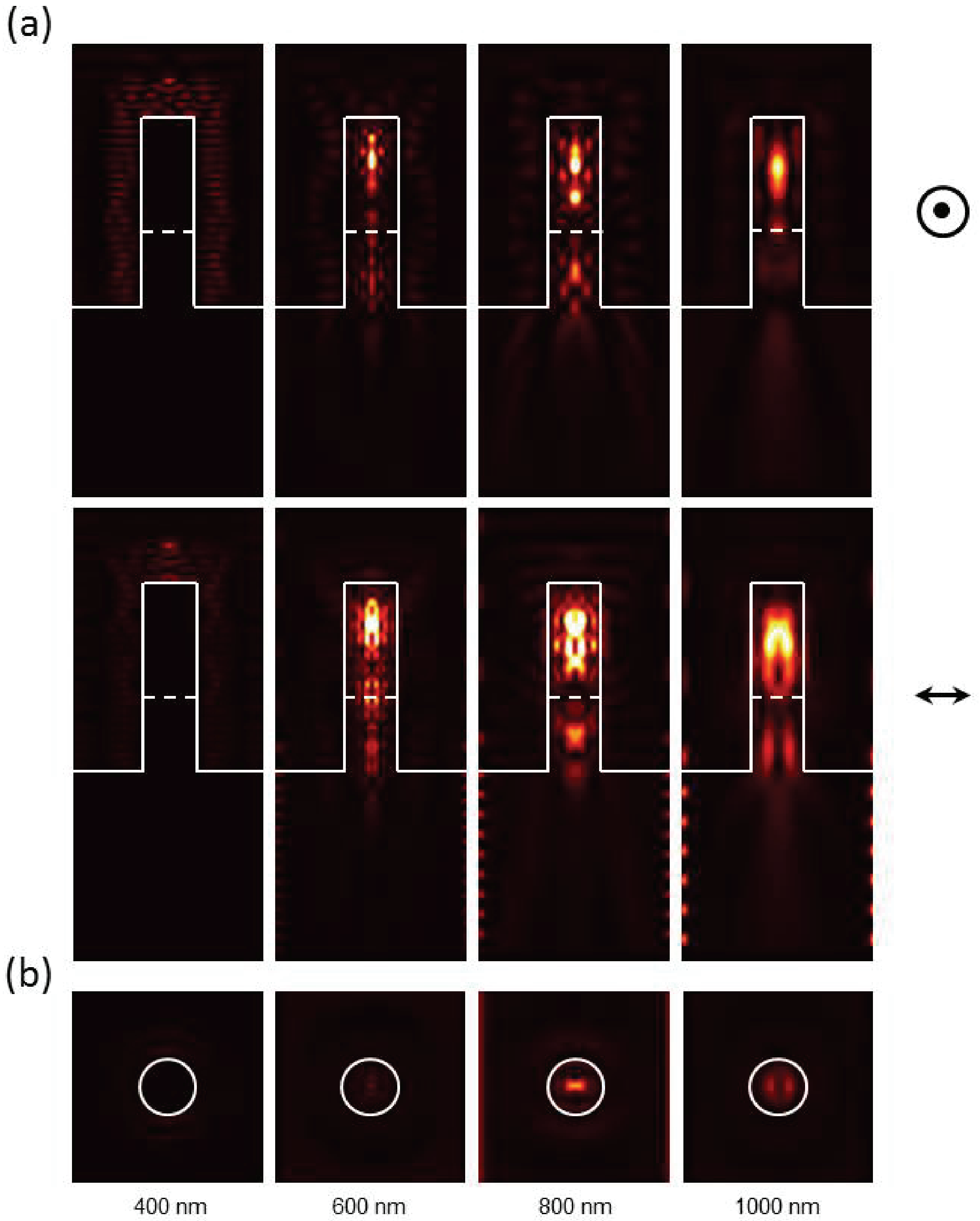

Figure 3.14: FDTD simulated electric field energy density (a) along the z–axis (above: cross–section at x= 0; below: cross–section at y= 0) and (b) at the cross–section placed 400 nm above the base of the Si nanowire (400 nm below the junction) at 400, 600, 800 and 1000 nm.

the wire. This confirms that the major losses are due to recombination in the wire. This is especially harmful for the SiO_2– and Al_2O_3–passivated devices but also for the one coated with SiN_x, as the junction is shifted further away from the generated carriers and more of them recombine before reaching the junction.

3.6 Conclusions

The impact of surface recombination on the performance of axial *p–n* junction Si nanowire–based solar cells has been investigated. Si nanowire arrays have been fabricated by means of Near–Field Phase–Shift Lithography (NF–PSL), a novel technique based on traditional photolithography which allows to push the resolution limits to the submicron scale. Four different passivation materials have been analyzed: ALD Al_2O_3, thermal SiO_2, PECVD SiN_x and a SiO_2/SiN_x stack. An improvement of the passivation quality gives rise to an important enhancement of the device performance, increasing the short–circuit current density, J_{sc}, the open–circuit voltage, V_{oc}, and the efficiency.

It has been demonstrated that the presence of a surface fixed charge density can lead to an inversion of carrier densities or to an enhancement of the recombination rate within the nanowire core. This effect could be nullified by the addition of a hydrogen–containing capping layer, which led to a hydrogen passivation of dangling bonds and to the suppression of the fixed charges at the interface. The device passivated with the SiO_2/SiN_x stack reported the best results, exhibiting a J_{sc} of 28.4 mA/cm^2, a V_{oc} of 0.52 V and an efficiency of 9.9%.

4 Alternative Front Transparent Electrode

Standard silicon solar cell processing includes a screen–printed metallic grid followed by a firing through step to form the front contacts. This type of contact has associated shading and resistive losses of around 10% [91]. Many alternatives have arisen to replace it. Historically, transparent conductive oxides (TCO) such as ZnO or indium–tin–oxide (ITO) have been the most largely used as they offer an interesting conductivity–transparency trade–off. The scarcity of indium has led researchers to seek other solutions. In this chapter, highly conformal metal nanoparticle films generated via a polymer–brush–guided method are proposed as a novel approach. This solution benefits from an additional light scattering enhancement due to surface plasmons on metal nanoparticles. The role they play in the overall performance of the device is also compared to a standard TCO such as tin–doped indium oxide.

Publications:

C. Sugnaux*, A. Dalmau Mallorquí*, J. E. Herriman, H. A. Klok, and A. Fontcuberta i Morral *Microwire Solar Cells with a Conformal, Plasmonic, Nanoparticle–Based Electrode, in preparation.*

**equal contribution*

4.1 Introduction

The front transparent electrode is a key element of a solar cell that must maximize light transmission and carrier collection. Unfortunately, accomplishing both of them in an optimum way is a struggle for photovoltaic technologies, as electrical conductivity is proportional to the square of the light absorption coefficient by the following relation:

$$\sigma = \frac{8\omega}{\mu_0}\left(\frac{nk}{c}\right)^2, \tag{4.1}$$

where σ is the conductivity, ω is the angular frequency of the wave, μ_0 is the permeability in vacuum, c is the speed of light in vacuum, n is the refractive index and k, the extinction coefficient. k is directly related to the absorption coefficient and hence, transmittance:

$$T = \exp(-\alpha t) = \exp\left(-\frac{4\pi k t}{\lambda}\right), \tag{4.2}$$

where α is the absorption coefficient, λ is the wavelength and t is the layer thickness.

Transparent conductive oxides (TCOs) have traditionally addressed these needs. The most well–known TCOs are impurity–doped ZnO, In_2O_3 and SnO_2, like Ga– and Al–doped ZnO (GZO and AZO) or combinations of these oxides, such as indium-tin-oxide (ITO). Transparency is intimately related with the electronic band structure of the material and its crystal structure. In order to be transparent to the most relevant part of the solar spectrum, a band gap of 3 eV or more is required and, as only insulator materials can have such a large band gap, they have to be doped to degeneracy to become conductive. At the same time, a high density of impurities leads to a decrease in carrier mobility. Hence, the doping level as well as the deposition technique have an important influence on the quality and performance of the material.

The most widely used TCO is ITO. It offers the lowest resistivity/transparency ratio, a wide variety of deposition methods and an easy processing, what converts it into an attractive material to be commercialized. ITO thin films can be produced by dip coating [92], sol–gel methods [93], reactive thermal deposition [94], chemical vapor deposition [95], electron beam evaporation [96], spray pyrolysis [97], laser ablation [98], atomic layer deposition [99] or sputtering [100]. A resistivity of $\sim 10^{-4}$ Ω·cm is often quoted as an optimized ITO resistivity, along with a transmittance above 85%. However, an important disadvantage of ITO is the scarcity of Indium.

Another widely used TCO material is ZnO. It has the advantage of a cheaper price and abundance over ITO. It is usually doped with Al or Ga (AZO and GZO, respectively) giving rise to similar conductivities to those of ITO.

However, researchers have struggled to find new solutions to avoid the use of such brittle materials considering the rising importance of flexible electronic devices and displays. These solutions include carbon nanotubes, graphene, highly conductive polymers, metal nanowire mesh and ultrathin metal films.

Carbon nanotubes are nanoscale cylinders composed of one–atom–thick sheet of graphene wrapped forming a tube. They have unique electrical properties due to their one–dimensional geometry and low density of defects (Figure 4.1a). Phonon scattering is highly reduced as electrons can only propagate forward and backward, and optical phonons are too high in energy to be present at room temperature. In addition, the effective density of states in nanotubes is much lower than traditional metals because of the semimetallic nature of graphene. These characteristics lead to large mean–free paths, which explains the high electron mobilities of carbon nanotubes [101, 102]. There exist several methods of producing transparent ultrathin films of pure single–walled carbon nanotubes (SWNT), giving rise to transmittances ranging from 70 to 90% over the visible part of the spectrum and sheet resistances between 30 and 200 $\Omega/\square$. These results are still inferior but approaching that of commercialized TCO, what brought some groups to report on the use of SWNT as a substitute of TCOs for optoelectronic applications [103–106].

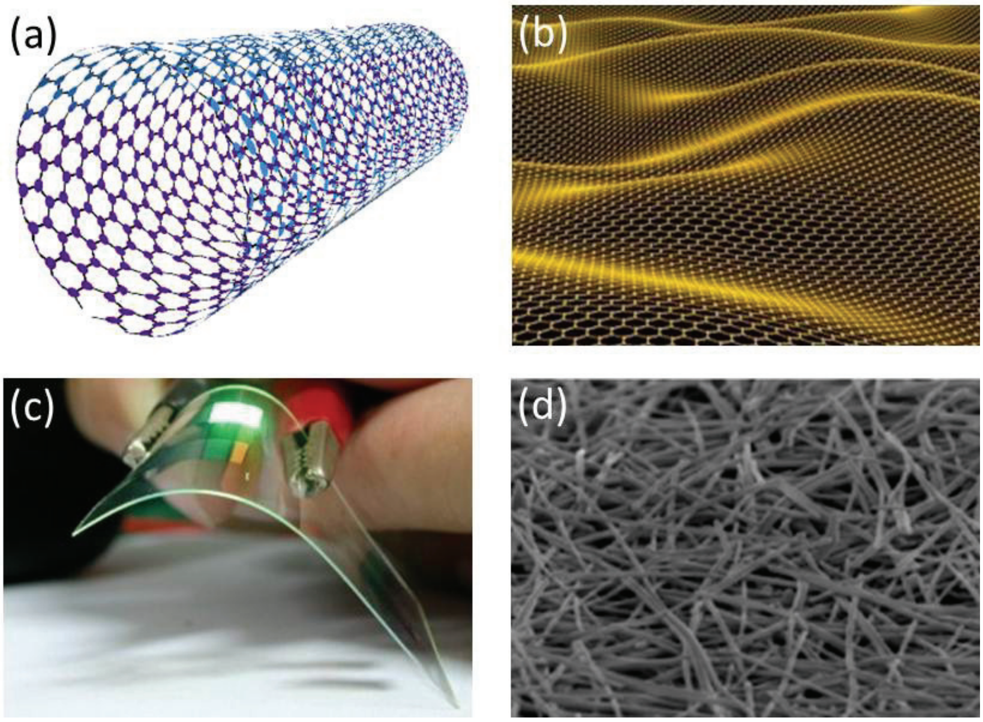

Figure 4.1: New transparent electrode solutions: (a) carbon nanotubes, (b) graphene, (c) highly conductive polymers, and (d) metal nanowire mesh.

A new breakthrough material as transparent electrode that came up in the last years was graphene (Figure 4.1b). Graphene is a material composed of pure carbon organized in a honeycomb lattice forming a one–atom thick planar sheet. Graphene is a semimetal with similar electrical properties to those of metallic carbon nanotubes. Although planar graphene itself has been presumed not to exist in the free state, Geim and Novoselov successfully prepared single–layer graphene and studied their electronic properties [107]. Carrier mobilities up to 10000 $\mathrm{cm^2/Vs}$ were measured, showing almost no dependency on absolute temperature, indicating that the mobility is limited by scattering on defects. These promising results encouraged many groups to suggest graphene for new feasible uses such as nanoelectromechanical systems (NEMS), batteries, field emitters, optoelectronic devices or labs–on–chips [108]. MIT professors Kong and Bulović [109] investigated the use of graphene as an electrode for organic solar cells. They achieved a transmittance of 91.2% and a sheet resistance ranging from 500 to 300 $\Omega/\Box$, for a 3–layered graphene sheet grown by CVD, which is still one order of magnitude higher than solar cells requirements. In addition, it can be easily exfoliated, what enables a good control of its thickness and, hence, of its transmittance. The biggest challenge they faced was the adhesion of graphene to the cell. They solved it by adding some impurities at the surface, for instance doping it, which moreover improved its conductivity.

Highly conductive polymers have also been proposed as an alternative electrode for flexible applications (Figure 4.1c). They started to be commercialized in the 1990s when the conductivity of common polymers was improved by doping them and stabilizing the doped state by dissolving them in common solvents. The instability of the doped state was a big problem since the conductivity decreases rapidly when exposed to various stresses (thermal, chemical, etc.) [110]. The most widely used is poly(3,4–ethylene–dioxythiophene) stabilized by aqueous polystyrenesulfonate acid (PEDOT:PSS). Due to its low–cost and simplicity in deposition over large–area electronics numerous works have focused on its use as transparent electrode on solar cells [111–113].

Another alternative solution is the use of a metal nanowire mesh [114] (Figure 4.1d). The resistivity of a metal nanowire mesh depends on wire resistance and wire–to–wire contact resistance. At higher densities, the wire–to–wire contact resistance decreases as it is favoured by the formation of many parallel connections, where the lowest resistance connections dominate the overall resistance. The size of the wires also plays a role, as the conductance of individual wires will increase with the length and the square diameter. On the other hand, the random nature of the mesh, added to the length of the wires and the wire density, leads to an increase of scattering of incident light and, thus, an increase of the diffuse transmission. Excellent electrical and optical properties have been reported for both silver [115, 116] and copper [117–119] nanowire meshes.

Metals are the most conductive materials thanks to a high density of free electrons. By slimming them down to few nanometers they become transparent to visible light, and hence they can be used as front electrode. However, they become highly resistive when the film thickness is smaller than the mean free path length. O'Connor *et al.* reported a sheet resistance of 15 $\Omega/\Box$ for a 9–nm thick Ag film [120]. They also modeled the evolution of resistivity versus the film thickness, by taking into account the reduction of the grain size at small thicknesses. They showed a sharp increase in sheet resistance for thicknesses below 10 nm, that they attributed to an increase of electron scattering.

In this chapter we propose a scalable process to obtain a highly conformal and transparent metal nanoparticle network as a transparent and conductive front electrode on radial microwire–based solar cells. This approach exploits polymer brushes [121], which have previously shown relevance in the fabrication of thin inorganic [122–125] and metallic films [126], as a matrix for the guided formation of gold and silver films. In this context polymer brushes offer an alternative synthetic tool because they allow the elaboration of conformal thin films with a precise control over thickness, metallic composition and microstructuration. This solution benefits from demonstrated light scattering enhancement due to surface plasmons on metal nanoparticles. The effect of the material, size and shape of isolated particles on electric intensity enhancement in the near-field outside the particles have been largely studied [127, 128], as well as the interaction between surface plasmons on neighboring particles and their benefits for photovoltaic applications [129–132]. Other important factors are the surrounding and underlying materials and also the distance between the particles and the substrate.

4.2 Plasmonics for Photovoltaics

When evaporating ultrathin films (~ 5 nm) of nobel metals, instead of a continuous film island–like structures are formed. These structures act as light scattering centers due to resonant oscillations of conduction electrons in the metal. These resonances are called surface plasmons on metal nanoparticles and they strongly interact with incident light of wavelengths near the plasmon resonance by scattering or absorbing it. Such properties sparked an interest amongst the photovoltaic community in the integration of nanoscale metal particles on solar cells. In particular, they offer an alternative to surface texturing, a technique largely used on thin–film solar cells. Nanoparticles have been proven to significantly enhance the photocurrent at long wavelengths, which are weakly absorbed in such devices [131, 133, 134].

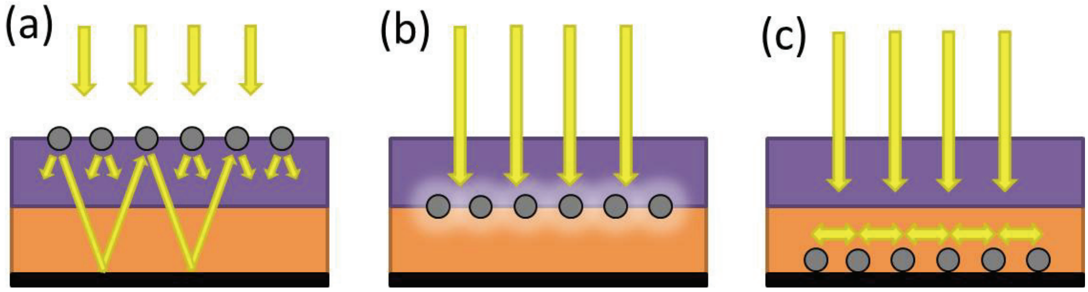

Figure 4.2: Plasmonic light–trapping by scattering from metal nanoparticles (a) placed at the surface, (b) embedded in the semiconductor, and (c) at the back surface (adapted from [129]).

These good results encouraged researchers to find new geometries that could take advantage of the benefits that plasmons offer. Atwater and Polman [129] suggested three different ways of using plasmonic nanostructures (Figure 4.2). On one hand, they proposed to use nanoparticles as scattering elements by placing them at the surface. On the other hand, when embedded in the semiconductor they can act as antennas inducing light concentration. Finally, they can trap and guide light in the semiconductor layer when positioned at the interface between the semiconductor and the back contact.

In order to understand the mechanisms that originate the photocurrent enhancement some theories were developed. For particles small compared to incident wavelengths, surface plasmons can be theoretically described by the point dipole approximation together with the quasistatic model, which lead to the following expressions to calculate the scattering and absorption cross–sections [135]:

$$C_{\mathrm{sca}} = \frac{1}{6\pi}\left(\frac{2\pi}{\lambda}\right)^4 |\alpha|^2 \tag{4.3}$$

and

$$C_{\mathrm{abs}} = \frac{2\pi}{\lambda}\mathrm{Im}[\alpha], \tag{4.4}$$

where α is the polarizability of the particle and is given by:

$$\alpha = 3V\left(\frac{\epsilon_{\mathrm{p}}/\epsilon_{\mathrm{m}}-1}{\epsilon_{\mathrm{p}}/\epsilon_{\mathrm{m}}+2}\right). \tag{4.5}$$

Here, V is the volume of the particle, ϵ_{p} is the dielectric function of the particle and ϵ_{m} is the dielectric function of the surrounding medium. From these equations one can already conclude that the main parameters influencing the surface plasmon resonance are the volume and material of the particle and the dielectric function of the surrounding material. Some works reported on the effect of these parameters on the scattering efficiency [127, 130]. Catchpole *et al.* [127] also analyzed the effect of an oxide layer between the particles and the substrate on the light–trapping enhancement. They showed that although the scattering cross–section increases with the oxide thickness, the fraction of light scattered into the substrate diminishes. Moreover, it has been demonstrated that plasmonic coupling between neighbouring particles can induce strong local electric field enhancements that increase when decreasing the particle spacing [132].

4.3 Sample Preparation

Polymer–brush–guided silver and gold nanoparticle (Ag–NP and Au–NP, respectively) networks were synthesized on radial *p*–*n* junction microwire–based solar cells and their planar counterparts. The *p*–core Si microwires were fabricated on a 380–μm thick Czochralski <100> wafer (ρ = 1–10 Ω·cm) by a combination of photolithography and deep reactive ion etching, as described in chapter 2. The diameter, spacing and length of the wires were 2.8, 8 and 9.8 μm, respectively. A 450–nm–thick *n*–doped shell was formed by diffusion of $POCl_3$ at 850°C for 35 min. The front surface was chemically modified as described below in order to deposit a thin Au–NP or Ag–NP film on the top of the device. The rear contact was formed by 200 nm of sputtered Al. The area of the completed devices was 16 mm^2.

The synthesis of metal–NP films on silicon microwires was performed in collaboration with the Laboratory of Polymers at EPFL. Polymer brushes synthesized by controlled radical polymerization (SI–CRP) were used as the matrix for *in–situ* Ag–NP and Au–NP synthesis (Figure 4.3). First, all the samples were cleaned by oxygen plasma before removing the native oxide layer with 40% HF. Photochemical grafting of alkene was used to attach a dense layer of ATRP initiators on the silicon surface [136, 137], from which PDMAEMA (poly(2–(dimethylamino)ethyl methacrylate)) or PHEMA (poly(2–hydroxyethyl methacrylate)) brushes were grown.

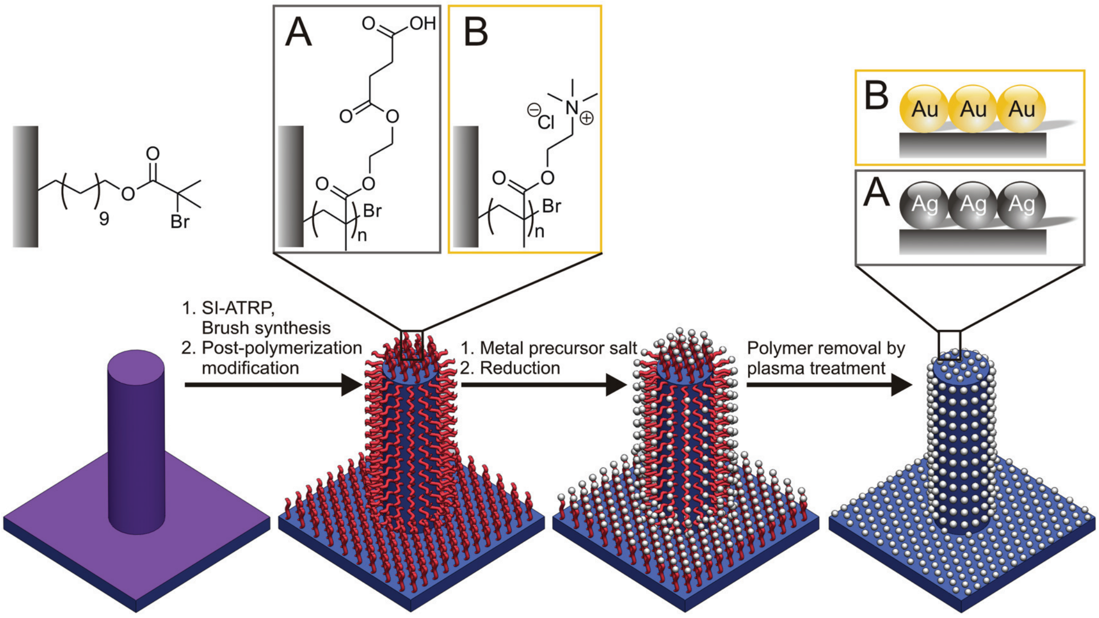

Figure 4.3: Schematic representation of the preparation of conformal gold and silver networks as top transparent electrodes on *p*–*n* junction microwire–based solar cells.

On one hand, PHEMA brushes led to the preparation of Ag–NP. Polymer brush/Ag–NP hybrids were prepared via a method similar to one reported elsewhere [138]. Carboxylic acid groups were incorporated on the PHEMA brush side chains by coupling the hydroxyl residues with succinic anhydride [139]. Loading of the acids groups with silver cations was followed by reduction of the complexed salt afford brush/Ag–NP hybrids layers. Next, hydrogen plasma was applied in order to remove the polymer–brush matrix [140].

On the other hand, Au–NP films were synthesized following the strategy developed by Paripovic *et al.* [126], implying the following steps: (i) quaternization of the PDMAEMA, (ii) complexation of gold anions, (iii) *in–situ* reduction and (iv) removal by oxygen plasma of the polymer brush template.

Figure 4.4 shows scanning electron microscopy images of both, Ag– and Au–NP films. Figures 4.4a and 4.4d give a close look to the morphology of the films. Figures 4.4b, 4.4c and 4.4e, 4.4f present the final devices covered with silver and gold nanoparticles, respectively. We

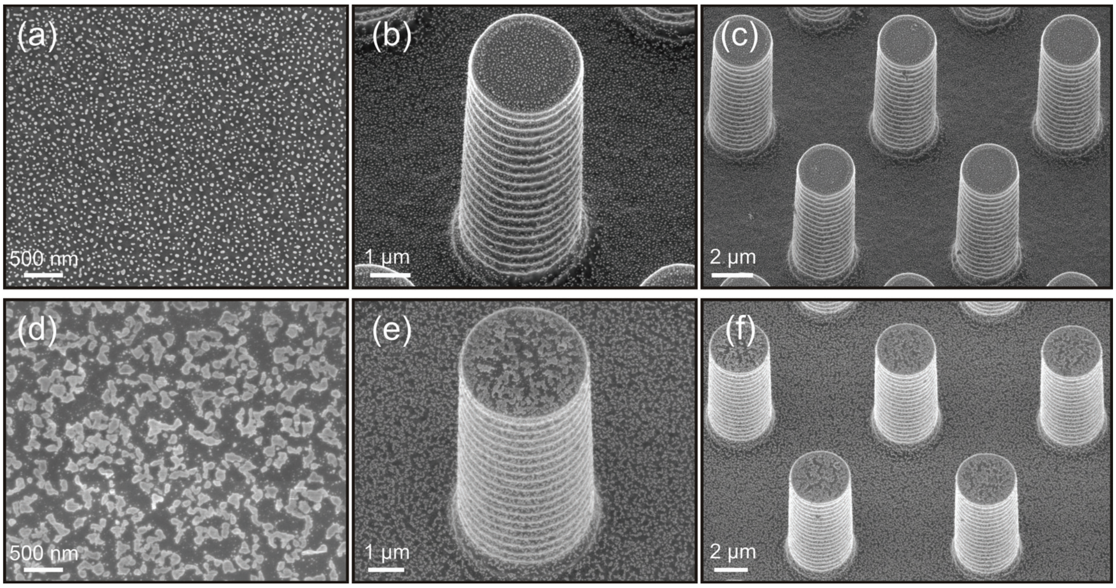

Figure 4.4: SEM images of Ag–NP films ((a), (b) and (c)) and Au–NP films ((d), (e) and (f)) taken at different magnifications (views at 25° tilt).

observe a homogeneous distribution of Ag–NPs across the entire surface of the device. This demonstrates the excellent conformability of both metallic films to high aspect–ratio surfaces.

We turn now towards some important details of the Ag–NP characterization. In order to monitor the entire process accurately, XPS analyses were performed at different stages of modification. Results are gathered in Figure 4.5. Immobilization of the bromoisobutyrate initiator on silicon surfaces was confirmed by the presence of a Br 3d signal at 71 eV in the XPS high–resolution spectra of bromide as well as the increase of water contact angle up to 86°. After surface–initiated polymerization of HEMA, the PHEMA film presents a typical high–resolution C 1s spectra which can be decomposed in five model Gaussian curves (Figure 4.5a) [141]. Post–modification with succinic anhydride results in an increase of carbonyl content and a decrease of ether groups, corresponding to binding energies at 289.1 and 287.0 eV, respectively (Figure 4.5). After silver loading, the polymer matrix contains Ag^{+} ions, as revealed by a Ag 3d doublet at 374.81 (Ag 3d3/2) and 368.80 eV (Ag 3d5/2) [142]. Formation of Ag–NP in the brush template after reduction with sodium borohydride was confirmed (Figure 3B); high–resolution Ag 3d spectra revealed the presence of a doublet Ag 3d3/2 and Ag 3d5/2 at 373.80 and 367.80 eV, respectively, which is in good agreement with the formation of metallic Ag(0) NP in a polymer network [143]. The complete disappearance of the carbonyl group in the high–resolution C 1s spectra combined with the drastic decrease of carbon content highlight the successful removal of the PHEMASA–brush matrix after the hydrogen plasma treatment (Figure 3C) causing the coalescence of Ag–NP into a thin film [126].

In Figure 4.6a AFM analyses of micro–patterned brushes on planar *p–n* junctions taken at each step of modification report on the evolution of film thickness during the fabrication

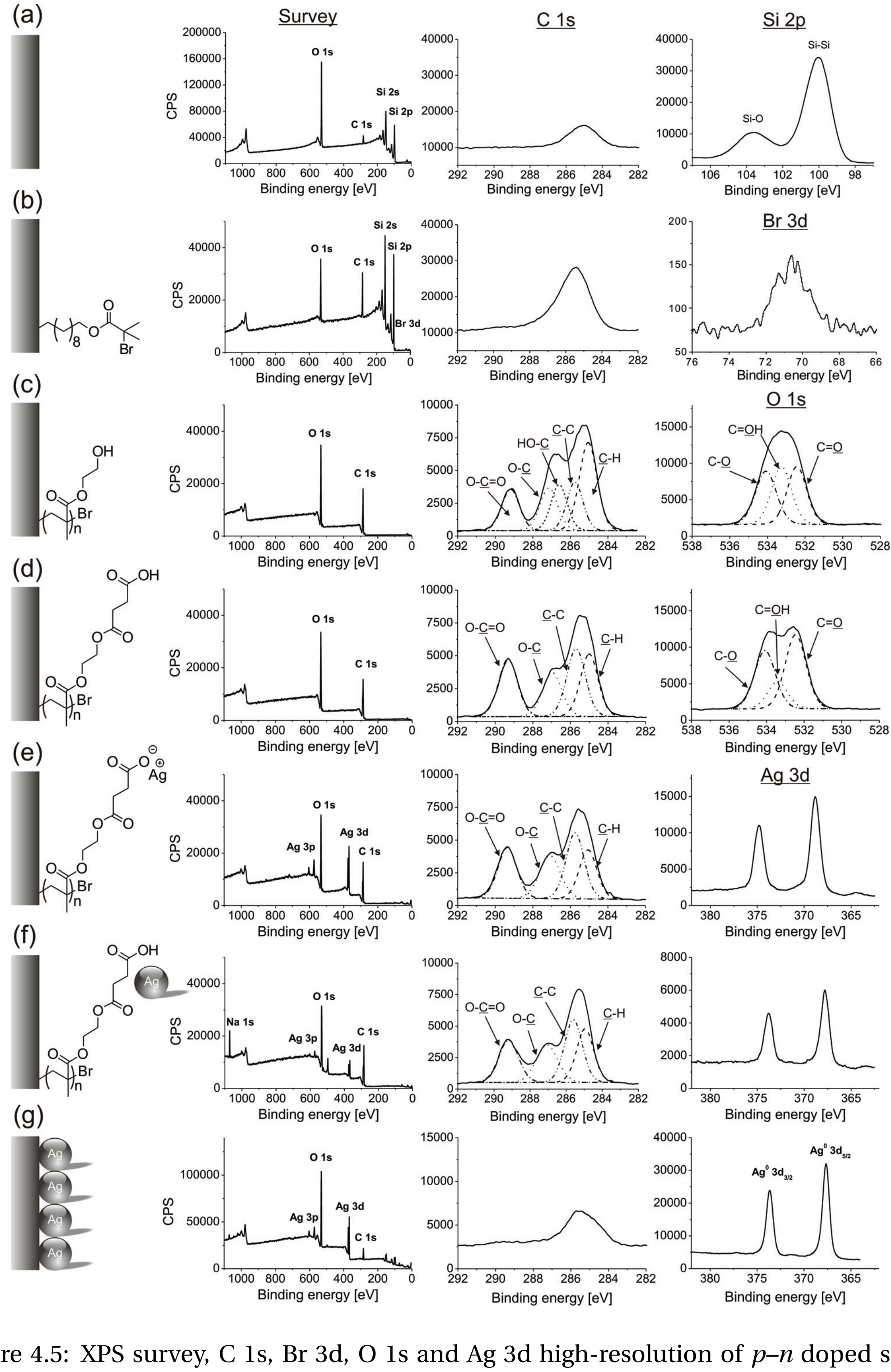

Figure 4.5: XPS survey, C 1s, Br 3d, O 1s and Ag 3d high-resolution of *p*–*n* doped silicon substrates modified with (a) ATRP initiator, (b) PHEMA brushes, (c) post-modified PHEMA, (d) silver loaded brushes, (e) AgNP loaded brushes and (f) silver film.

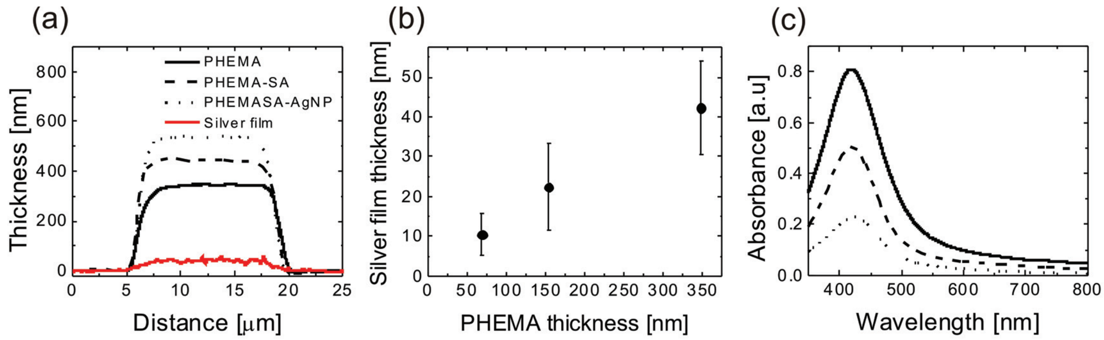

Figure 4.6: (a) AFM cross–sectional profiles of patterned PHEMA (dotted line), post–modified PHEMA (dashed line), silver nanoparticles–loaded PHEMA modified brushes reduced with 10 mM $NaBH_4$ (full line) and silver film (red line). (b) Comparison of the silver film thicknesses obtained after plasma treatment of PHEMASA–AgNP composite film with that of the initial PHEMA brush template. (c) UV/vis spectra of $AgNO_3$ loaded PHEMASA brushes after reduction with 10 mM $NaBH_4$. The original PHEMA brush thicknesses were 95 nm (dotted line), 151 nm (dashed line) and 276 nm (full line).

process. Extension of PHEMA side chains with carboxylic groups resulted in a substantial increase of brush height. After treating the PHEMA–SA brush with silver nitrate and sodium borohydride, formation of Ag–NP in the network occurred, leading to a second significant increase of brush thickness. Finally, a drastic decrease of profile height is observed upon matrix removal, attesting the physical deposition of Ag–NP on the surface. In Figure 4.6b we show the dependence of the silver thin film thickness on the original PHEMA brush thickness, which is clearly linear. In addition, Ag–NP–loaded matrices prepared from PHEMA brushes of different brush heights were analyzed by UV/vis (Figure 4.6c). Their absorbance displayed a characteristic absorption peak at 420 nm [144, 145], confirming the presence of Ag–NP in the network and furthermore highlighting that higher concentrations of Ag–NP were found in thicker brush matrices as an effect of brush thickness. The influence of the reducing agent concentration on the formation of Ag–NP was also investigated (Figure 4.7). Independent of

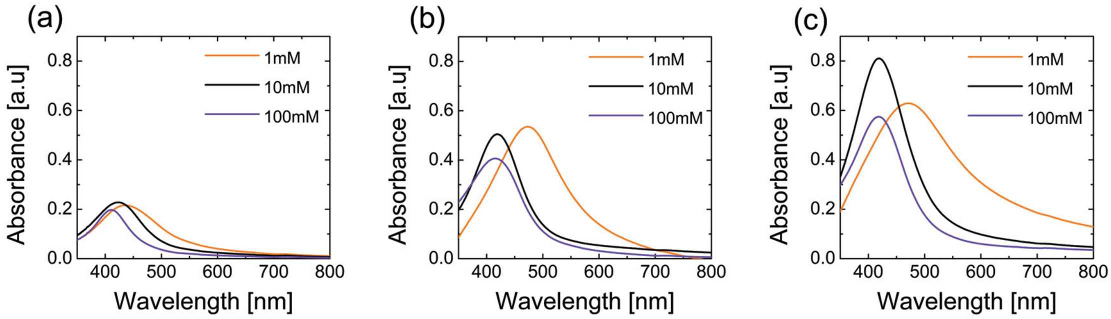

Figure 4.7: UV/vis spectra of silver nanoparticles loaded post-modified PHEMA brushes grown for (a) 1, (b) 2 and (c) 7 hours. The reducing agent concentration was of 100 mM (violet line), 10 mM (black line) and 1 mM (orange line).

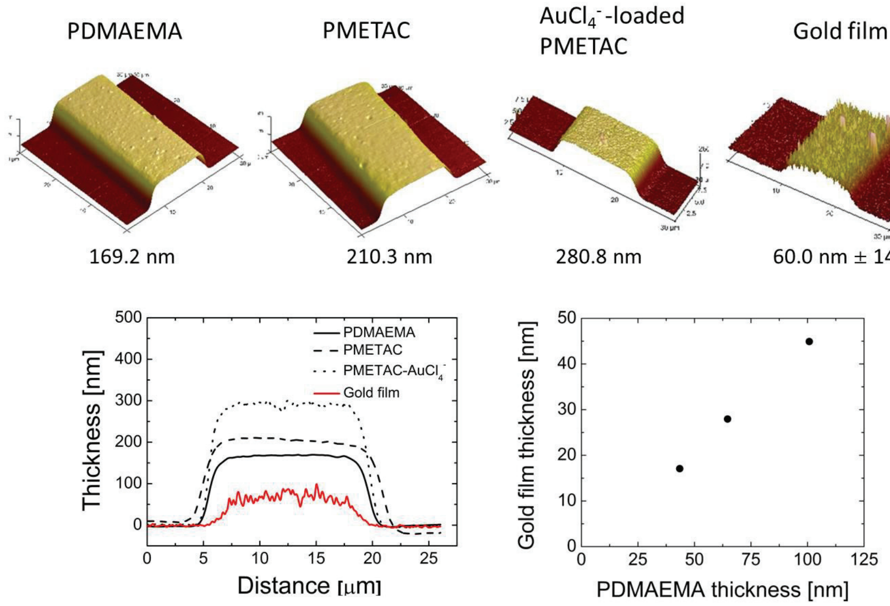

Figure 4.8: Top: AFM pictures of patterned polymer brushes at different steps of modification. Bottom left: height profiles of patterned polymer brushes at different steps of modification. Bottom right: Comparison of the gold film thicknesses obtained after plasma treatment with that of the starting PDMAEMA brush template.

polymerization time, a single and characteristic absorption peak was observed at 420 nm when high concentrations of reducing agent were used (10 and 100 mM). If a lower concentration (1 mM) of reducing agent was applied to the system, a red shift to 470 nm was observed. The polymer brush/Ag–NP hybrids prepared in the first case were composed of well–dispersed and spherical Ag–NP while the bathochromic shift observed for the second case may suggest an increase in the Ag–NP size or partial aggregation of the Ag–NP into the network [138].

Similar results were obtained in the preparation of Au–NP films. Figures 4.8 bottom left and 4.8 bottom right show the thickness of patterned polymer brushes at different steps of modification and the lineal dependence of the resulting gold film thickness with that of the initial PDMAEMA brush matrix, respectively. The conversion of PDMAEMA brushes to PMETAC resulted in an increase of the film thickness, which was further increased when loading PMETAC brushes with $AuCl_4^-$. Polymer removal led to an abrupt decrease of the profile height. The characterization of the synthesis was completed by a XPS analysis at different stages of the process. Figure 4.9 displays the XPS spectra of PDMAEMA brushes, PMETAC brushes and the gold film after the polymer removal. The shift of the N 1s peak from 397.7 to 401 eV and the appearance of a Cl 2p signal at around 194 eV in the N 1s and Cl 2p high–resolution scans corroborate a 100% quaternization of the tertiary amine groups on the conversion of PDMAEMA to PMETAC brushes. Finally, the high–resolution XPS spectra after plasma treatment show a drastic reduction of the C 1s signal and the presence of Au $4f_{7/2}$ and Au $4f_{5/2}$ signals, demonstrating the formation of polymer–free gold nanoparticle network.

In Figure 4.10a, the UV/vis spectra of $AuCl_4^-$–loaded PMETAC brushes are compared. Again, the gold loading capacity increases with the polymer brushes thickness and they show a peak at 320 nm caused by the absorbance of the gold chloride anion. The reduction of the gold salt

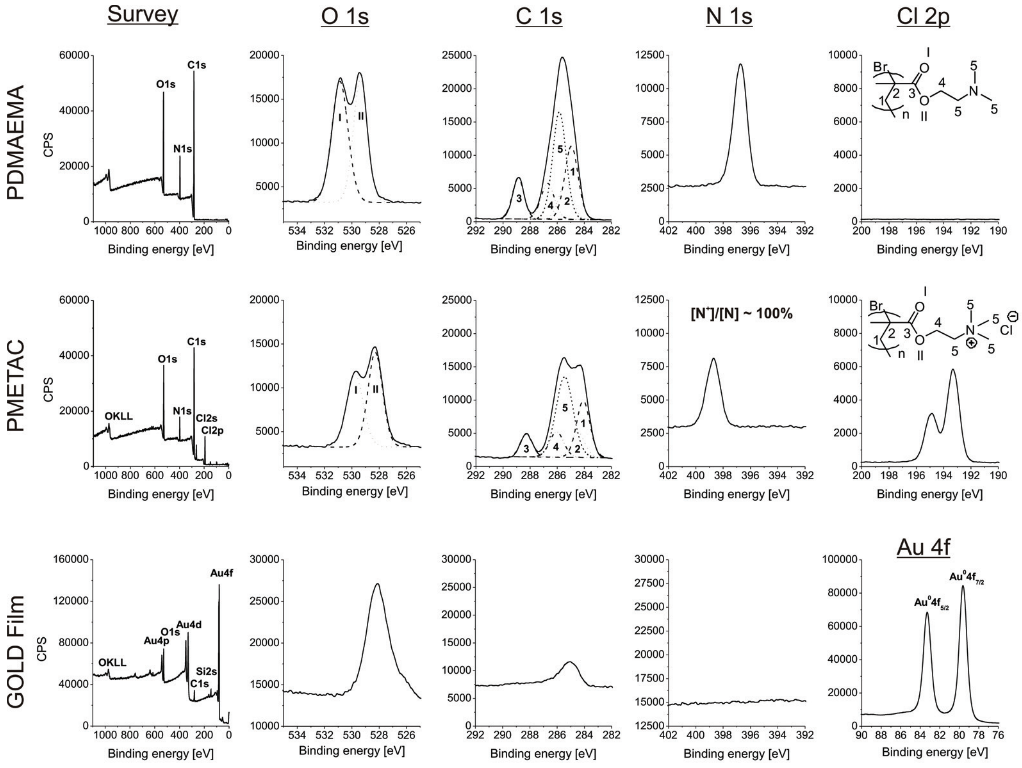

Figure 4.9: XPS of silicon oxide functionalized with poly(diemthylaminoethyl) methacrylate grown for 10 minutes. From the top to the bottom: (1) PDMAEMA brushes, (2) PMETAC brushes, (3) formation of the thin gold film after plasma removal of the polymer layer.

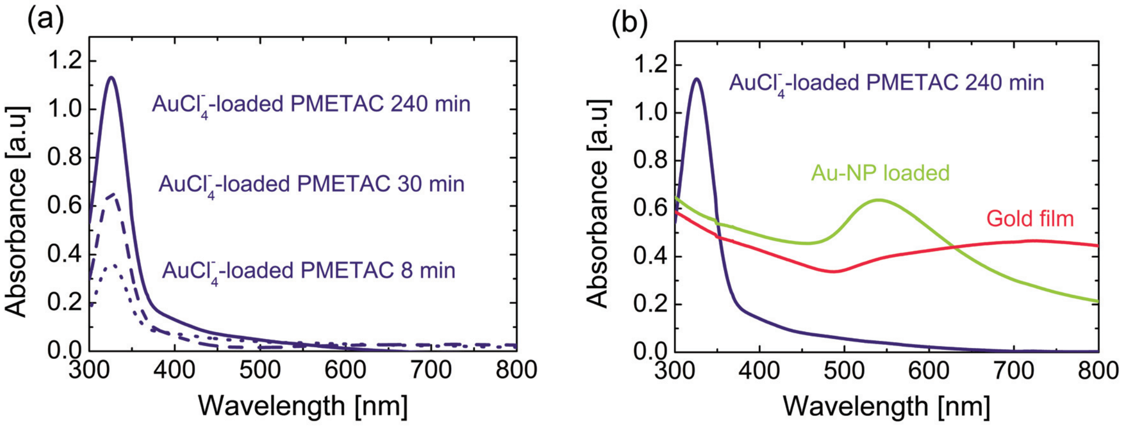

Figure 4.10: (a) UV/vis spectra of $AuCl_4^-$–loaded PMETAC brushes. (b) UV/vis spectra of $AuCl_4^-$–loaded PMETAC brushes after 240 minutes of polymerization.

is confirmed by the disappearance of the 320–nm absorbance peak and the appearance of a new peak around 550 nm, corresponding to the formation of Au–NP (Figure 4.10b).

4.4 Results

In order to prove the potential of such films as transparent front electrodes, they were first tested on planar *p*–*n* junction devices. Solar cells coated with Au–NP and Ag–NP films (75 and 17 nm thick, respectively) were compared to the same structure coated by 200 nm of sputtered ITO ρ = 0.2–0.4 mΩ·cm). For the sake of simplicity, from now on devices coated with gold and silver nanoparticle films will be called Au–NP and Ag–NP devices, respectively. Figure

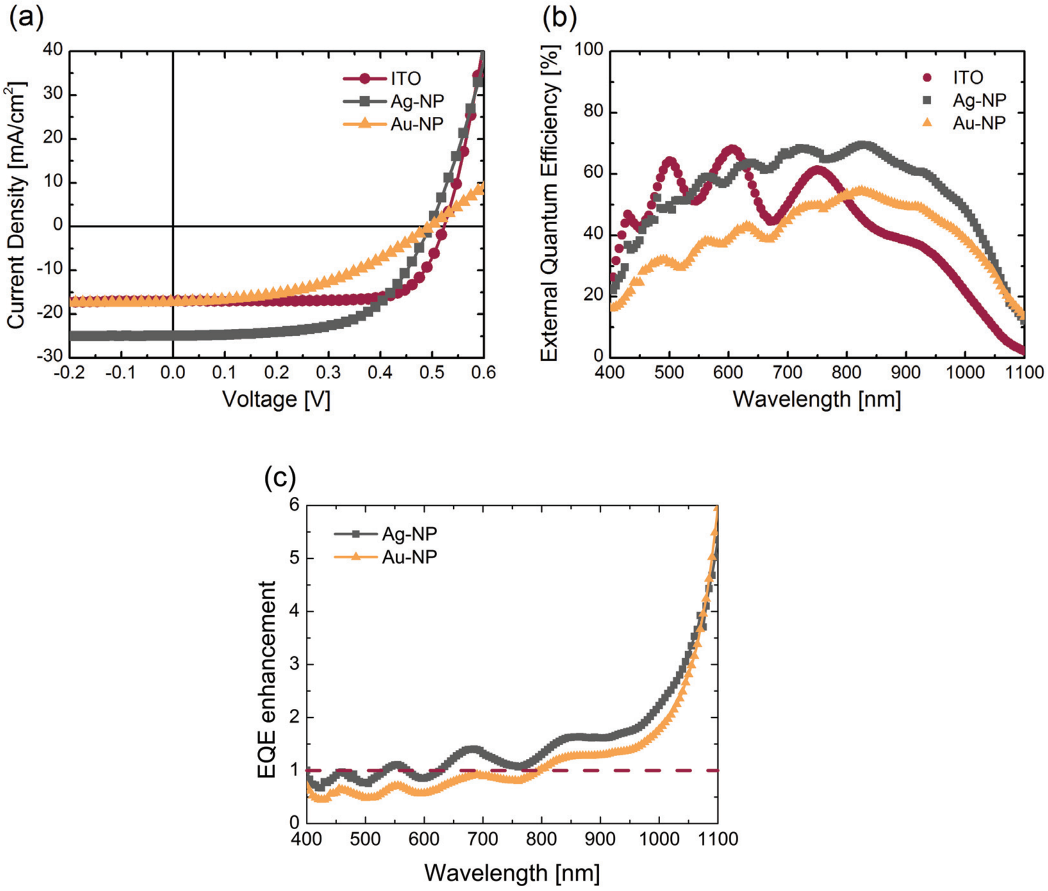

Figure 4.11: Comparison of the photovoltaic response of a planar Si solar cell coated with three different front electrodes: 17–nm–thick polymer–brush–guided Ag–NP film (grey–square–symbol line), 75–nm–thick polymer–brush–guided Au–NP film (orange–triangle–symbol line), and standard 200–nm–thick sputtered ITO (maroon–dot–symbol line). (a) Current–voltage curves under an illumination of AM 1.5G, (b) EQE of the three devices, and (c) EQE enhancement ($\text{EQE}/\text{EQE}_{\text{ITO}}$) of Ag–NP and Au–NP devices respect to the ITO device (maroon dashed line represents the reference $\text{EQE}_{\text{ITO}}/\text{EQE}_{\text{ITO}}$

4.11a and Table 4.1 show the current–voltage curves and the photovoltaic properties of the three different devices. The series resistance of the Ag–NP cell (R_s = 12 Ω) is similar to the one covered with standard ITO (R_s = 3 Ω). On the contrary, the Au–NP film is much more resistive (R_s = 80 Ω), probably due to a high Schottky barrier at the Au/*n*–Si interface.

Table 4.1: Measured photovoltaic properties of planar solar cells coated with Ag–, Au–NP films and ITO.

electrode material	film thickness (nm)	J_{sc} (mA/cm^2)	V_{oc} (V)	FF	R_s (Ω)	η (%)
Ag	7	24.9	0.50	0.60	12	7.4
Au	75	17.3	0.50	0.44	80	3.8
ITO	200	17.0	0.52	0.74	3	6.6

Furthermore, both metallic nanoparticle networks exhibit better J_{sc} than the cell coated with ITO: J_{sc} is increased by a margin of 46% for the Ag–NP device and 2% for the Au–NP device. These successful results could be explained by a better light transmittance of metal-NP networks compared to the ITO film. However, comparing the UV/vis spectra of the three layers presented in Figure 4.12 it can be clearly seen that the ITO film is less absorbent for the whole range of wavelengths. Then, the existence of a plasmonic–related absorption enhancement of the subwavelength–sized particles forming the film should be considered [129, 146, 147]. The effect of plasmons on light scattering enhancement is especially beneficial for indirect band gap materials such as Si, which exhibit poor light absorption at wavelengths close to the band gap [133, 148]. This effect is less pronounced for Au–NP due to their high absorption cross–section over the extinction cross–section (the sum of scattering and absorption cross–sections) [127]. This hypothesis is further supported by the external quantum efficiency (EQE) measurements presented in Figure 4.11b. For the sake of clarity, the metal–NP devices are normalized by the ITO cell in Figure 4.11c. Both devices exhibit lower photocurrent responses

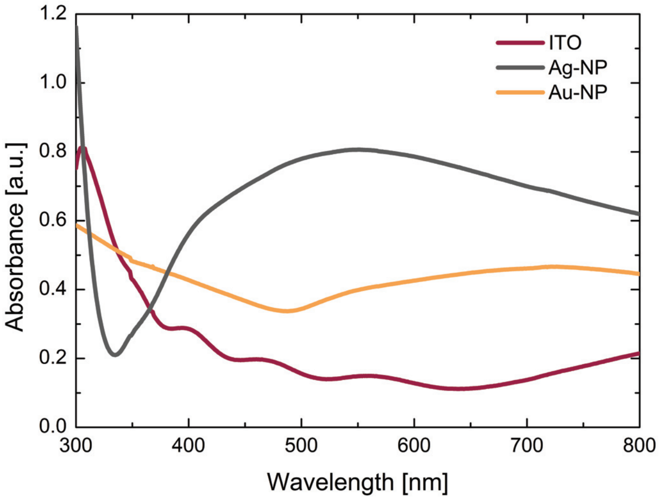

Figure 4.12: UV/vis spectra of ITO, Au–NP and Ag–NP films.

at short wavelengths but they experience a significant EQE increase at wavelengths close to the band gap, ramping up to an enhancement factor of 6 with respect to the ITO cell photoresponse.

These good R_s and J_{sc} values yield an overall efficiency of 7.4% for the Ag–NP electrode, improving the results obtained by ITO (6.6%).

Table 4.2: Photovoltaic properties comparison between planar and microwire-based solar cells under AM 1.5G illumination.

device configuration	J_{sc} (mA/cm^2)	V_{oc} (V)	FF	R_s (Ω)	η (%)
Planar	24.9	0.50	0.60	12	7.4
Microwires	22.7	0.35	0.36	16	2.8

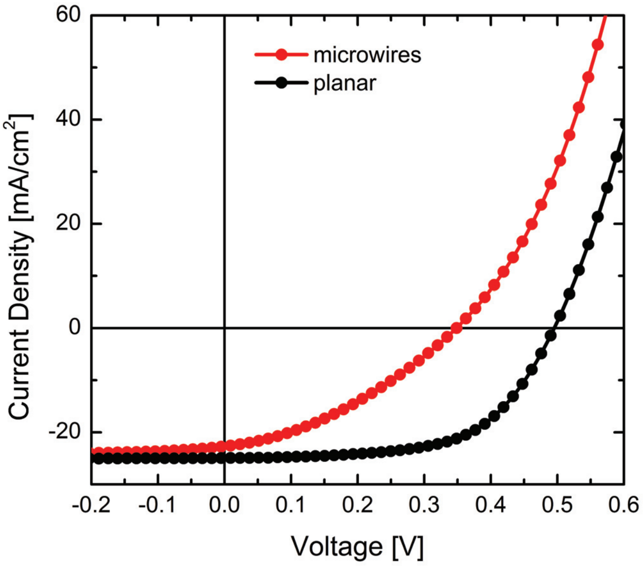

Figure 4.13: Current–voltage characteristics of the best measured planar and microwire-based solar cells under AM 1.5G illumination. The thickness of the Ag thin film in both cases is 17 nm.

As a further proof–of–concept, we coated microwire arrays with an Ag–NP top electrode. As shown in Figure 4.4, the particles are uniformly distributed over all the wire surface forming a conformal metallic network. Typical current–voltage characteristics of a microwire–based device under AM 1.5G illumination is presented in Figure 4.13 and compared to its planar counterpart. The microwire–based device exhibits a R_s of 16 Ω, a V_{oc} of 0.35 V, a FF of 0.36, a J_{sc} of 22.7 mA/cm^2 and an efficiency calculated over the total projected area of 2.8%. It should be noted that FF and V_{oc} values of the microwire–based device are much lower than those of the planar cell. Considering the high surface–to–volume ratio of microwires, the microwire–based devices are more sensitive to surface recombination losses. Therefore, their performance could significantly be affected by recombination losses produced at the metal/Si interface. In order to avoid this detrimental effect, the addition of an oxide layer between the device and the nanoparticle film would minimize the contact area and prevent from interface losses while keeping the light scattering advantages of surface plasmons [62, 133]. Still, this solution could cause an increase of the series resistance. Therefore a compromise between reducing ohmic losses and series resistance should be found.

The effect of the metallic film thickness on the performance of the microwire–based device was also investigated. The initial thickness of PHEMA brushes could be controlled by changing the polymerization time, which results in a linear variation of the final film thickness (Figure 4.6b). By fixing the polymerization time to 1, 2 and 7 hours, silver films with a thickness of 7, 17, and 24 nm, respectively, were obtained. In Figure 4.14, high–resolution AFM images of the three film thicknesses are shown. It can be qualitatively observed that the size, shape and density of Ag–NPs change with film thickness. From these images, the diameter of the particles were estimated to be around 50 and 60 nm for a polymerization time of 1 and 2 hours, respectively. For a polymerization time of 7 hours, particles agglomerate. Then, when increasing the thickness, the particles become larger, less spherical and less densely packed.

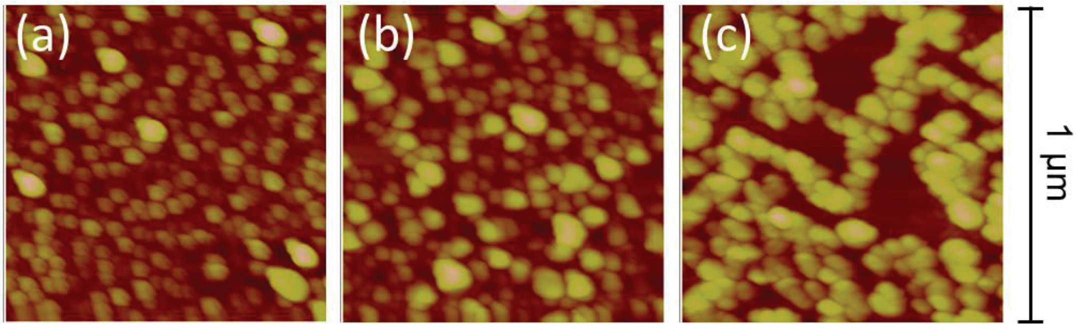

Figure 4.14: AFM images the Ag–NP film obtained after a polymerization time of (a) 1, (b) 2 and (c) 7 hours (fixed reducing agent concentration of 10 mM).

The current–voltage characteristics of microwire–based devices coated with these three different Ag–NP film thicknesses were measured under illumination (Figure 4.15) and the results are summarized in Table 4.3. As it could be expected, the silver film becomes more conductive when increasing its thickness and it results in a drop of the series resistance from 143 to 14 Ω. Short–circuit current density also increases with the thickness, exhibiting an increment of 27.5% and 32.5% for the 17– and 24–nm thick films with respect to the film of 7 nm, respectively.

Assuming that the metal particles are small compared to incident wavelengths, we can consider the quasistatic approximation model introduced in section 4.2 to describe the light absorption and scattering from Ag nanoparticles. It results from this theory that the absorption cross–section of a particle, C_{abs}, depends linearly on its volume (Equation 4.4), whereas the scattering cross–section, C_{sca}, depends on the square of the particle volume (Equation 4.3). If we define the extinction cross–section as,

$$C_{\text{ext}} = C_{\text{sca}} + C_{\text{abs}} \tag{4.6}$$

we can conclude that as the size of the particles increases, it is dominated by scattering [129, 149]. For instance, the albedo (scattering cross–section over extinction cross–section) of a 25–nm–diameter Ag particle is 0.1 and it rises up to 0.9 for particles with a diameter of 100 nm [150]. Therefore, at longer polymerization times particles are larger and their scattering cross–section also increases.

Table 4.3: Measured photovoltaic properties of microwire solar cells for different Ag thin film thicknesses.

polymerization time (h)	film thickness (nm)	J_{sc} (mA/cm^2)	V_{oc} (V)	FF	R_{s} (Ω)	η (%)
1	7	17.8	0.38	0.29	143	2.0
2	17	22.7	0.35	0.36	16	2.8
7	24	23.6	0.30	0.36	14	2.5

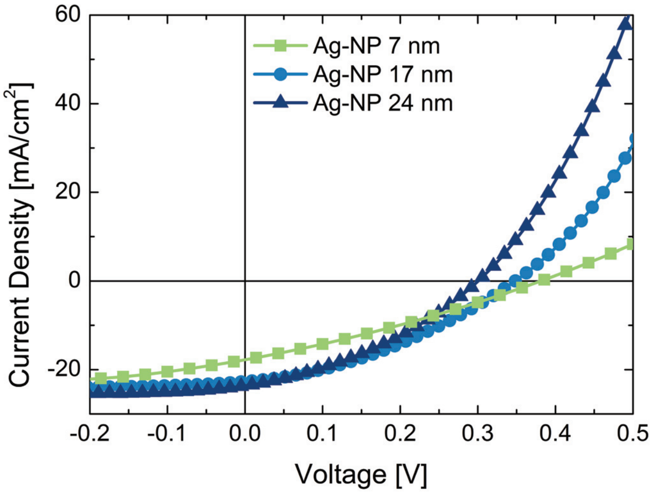

Figure 4.15: Current–voltage characteristics of micropillar arrays coated with three different Ag–NP film thicknesses: 7, 17 and 24 nm.

On the other hand, we should also consider the shape of particles. When increasing the polymerization time, the particles become less spherical and they can exhibit the lightning rod effect [151]. This could cause the concentration of the dipolar fields at the tip and corners of the particles. The more needle–like the particle, the stronger the near–field enhancement.

Finally, we observe that the open–circuit voltage decreases with increasing the film thickness. This could be due to an increase of recombination losses at the metal–semiconductor ohmic contact when increasing the particles size, which limits the V_{oc} of the solar cell.

4.5 Conclusions

In conclusion, we have demonstrated the synthesis of highly conformal polymer–brush–guided Au– and Ag–NP films on silicon microwire arrays. The proposed method uses thin polymer films prepared by surface-initiated atom transfer radical polymerization as a template for the formation of the electrode. This strategy allows to control the thickness, shape and density of metal nanoparticles by controlling the polymer brush thickness. Such films exhibit good conductive properties and enhanced light absorption due to the plasmonic scattering properties of the particles. An increase of 2% and 46% on the short–circuit current density was obtained for devices coated with Au– and Ag–NP, respectively, compared to the one reported by cells coated with standard ITO as transparent electrode.

5 Ordered Growth of III–V Nanowires for Solar Cell Fabrication

There are two distinct approaches to create small objects: top–down and bottom–up. The bottom–up approach, in which atoms assemble themselves to construct more complex structures, offers the possibility of going beyond the limits that top–down technologies establish. The desired size and optical and electronic properties can be obtained by precisely controlling their assembly during the growth. A key issue to integrate these structures to a wide range of devices is the growth of ordered arrays, achievable by patterning the substrate. Here, the role of the pattern geometry on the nanowire growth is still not fully understood. In this chapter, some guidelines on the impact of holes spacing on the InAs nanowire growth will be given. The potential and pitfalls of InAs nanowire arrays on Si as solar cells are exploited as well.

Publications:

(1) S. Conesa–Boj, E. Russo–Averchi, A. Dalmau–Mallorquí, J. Trevino, E. F. Pecora, C. Forestiere, A. Handin, M. Ek, L. Zweifel, L. R. Wallenberg, D. Rüffer, M. Heiss, D. Troadec, L. Dal Negro, P. Caroff, and A. Fontcuberta i Morral, *Vertical "III–V" V–Shaped Nano–Membranes Epitaxially Grown on a Patterned Si[001] Substrate and their Enhanced Light Scattering*, ACS Nano **6** (2012), 10982–10991.
(2) E. Russo–Averchi, A. Dalmau–Mallorqui, I. Canales–Mundet, G. Tutuncuoglu, E. Alarcon–Lladó, M. Heiss, D. Rüffer, P. Caroff, S. Conesa–Boj, and A. Fontcuberta i Morral, *Growth Mechanisms and Process Window for InAs V–Shaped Nanoscale Membranes on Si[001] Substrate and their Enhanced Light Scattering*, Nanotechnology 2013, *accepted.*
(3) M. Heiss*, E. Russo–Averchi*, A. Dalmau–Mallorquí*, G. Tutuncuoglu*, F. Matteini, D. Rüffer, S. Conesa–Boj, O. Demichel, E. Alarcon–Lladó, and A. Fontcuberta i Morral, *III–V Nanowire Arrays: Growth and Light Interaction*, Nanotechnology 2013, *accepted* (invited paper for the 10th anniversary of the journal).
(4) A. Dalmau Mallorquí, E. Alarcon–Lladó, E. Russo–Averchi, G. Tutuncuoglu, and A. Fontcuberta i Morral, *Ordered Growth of InAs Nanowires on Silicon for Solar Cell Fabrication, in preparation.*

5.1 Introduction

Indium arsenide is a widely used semiconductor material due to its high electron mobility, which enables high–speed and low–power devices, as well as its direct band gap, which is interesting for photon emitting and detection devices in the infrared. A key issue to make indium arsenide (InAs) attractive for industrial applications is their integration on the largely developed Si platform. The use of InAs nanowires on Si devices could provide them with faster and more efficient performances, but still taking advantage of the renowned CMOS technology platform.

From the perspective of a photovoltaic application, GaAs is much better suited material for single–junction devices due to its band gap of 1.42 eV, which sits close to the visible range of the solar spectrum. Shockley and Queisser calculated the theoretical upper limit or detailed balance limit for the efficiency of solar cells as a function of the energy gap [12] (Figure 5.1). The Shockley–Queisser limit predicts a maximum efficiency of around 6% for an InAs single junction (band gap of 0.35 eV) while it rises up to 32% in the case of GaAs. However, it is difficult to grow GaAs nanowires in a selfcatalysed–manner on a patterned Si substrate. It has been shown that the thickness of the oxide layer together with sample preparation and surface cleaning play an important role on GaAs nanowire growth [152–154]. Due to this setback, InAs was chosen as a model system for III–V nanowires integration on Si. Solar cells based on GaAs nanowire arrays will follow once the growth issues will be solved.

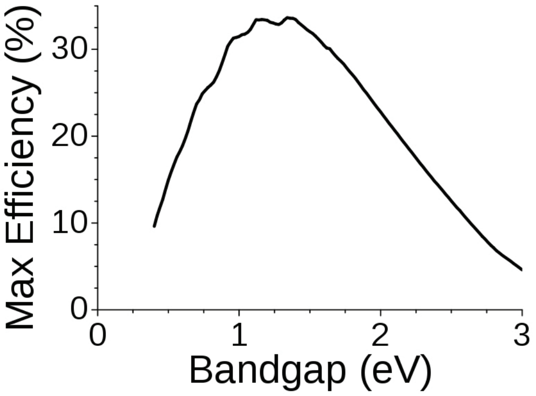

Figure 5.1: Shockley–Queisser limit for the efficiency of the solar cell depending on the energy gap of the semiconductor. [155]

There are numerous difficulties to overcome for the growth of InAs on silicon (and III–Vs in general), such as lattice mismatch and differences in thermal expansion coefficients and polarity. The mismatch in the lattice constant between Si and InAs is 11.6%. This introduces an interface strain that leads to the appearance of misfit dislocations. In the case of nanowires the strain can be relaxed laterally thanks to their small diameter [156] and dislocations are present only at the interface, with little impact on the device performance [157]. Similar problems could be caused by thermal mismatch, as epitaxy growth takes place at high temperatures.

Finally, because silicon is a nonpolar semiconductor whereas III–V semiconductors are polar, anti–phase domains are very likely to occur [158]. Again, the use of nanowires can avoid this problem since each crystal plane is believed to start growing by a single nucleation event across the interface with the substrate [159].

In many applications, a control on the position and orientation of the nanowires is required to effectively employ such structures. Vertical orientation can be achieved on Si (111) substrates in very high yields [160–162] and ordered array of wires can in principle be attained by employing a patterned mask layer. Many techniques have been developed for nanopatterning, such as electron beam lithography, nanoimprint lithography [163], nanosphere lithography [164], phase shift lithography [74] or anodic aluminium oxide masks [165].

The effect of the pattern design on the nanowire growth has been investigated, but with apparent contradictory results. While Hertenberger *et al.* [161] observed a clear dependency of the axial growth rate with the pitch (constant growth rate for pitches larger than 1.5 μm and decreasing growth rate with time for smaller pitches), Björk *et al.* [160] determined a constant growth rate independently of the pitch. In this chapter, an analysis of the kinetics that governs the growth of position–controlled and catalyst–free InAs nanowires grown by Molecular Beam Epitaxy (MBE) is presented. As the growth process of InAs nanowires is very sensitive to temperature, pressure, V/III ratio or oxide thickness, we studied samples grown in the same conditions. In this way, the effect of the pattern geometry (size of the oxide openings and spacing) could be evaluated in detail. Furthermore, a method to contact an array of vertical nanowires for their use as solar cells is proposed.

5.2 Nanowire Growth Mechanisms

We have grown ordered arrays of InAs nanowires by molecular beam epitaxy. MBE is an ultra–high–vacuum method of growing crystalline semiconductors. Thanks to its ultra–high vacuum conditions, to the absence of chemical precursors and to the extreme purity of the source elements, highly pure films can be achieved. Source elements are heated in separate cells and deposited at a controlled rate on the target substrate. High–vacuum conditions in the main chamber ensure that the mean free path of the vaporized atoms or molecules is larger than the chamber diameter, such that there is no interaction between them before reaching the substrate surface (the so called *molecular beam*).

Crystalline one–dimensional III–V nanostructures can be grown, either by MBE or other synthesis techniques such as metalorganic vapor phase epitaxy (MOVPE) or chemical beam epitaxy (CBE).

5.2.1 Catalyst–assisted nanowire growth

A new concept to perform crystal growth from the vapor was formulated by Wagner and Ellis in 1964 [166]. They called it Vapor–Liquid–Solid (VLS) mechanism and it explains the growth of 1D nanostructures from a foreign metal droplet (typically gold). Growth species are collected in the metal droplet and form a liquid alloy. Following the thermodynamic phase diagram, the increase of growth species content in the liquid droplet leads to a supersaturation resulting in the precipitation and epitaxial growth of a nanowire. Later on, Givargizov established the basis of the kinetics involved in the VLS growth [167]. We take the example of a Si nanowire. In order for Si to crystallize at the liquid–solid interface a thermodynamic driving force is required. This force is called supersaturation and it is defined as the effective chemical potential difference of Si dissolved in the liquid droplet and in the wire. According to the Gibbs–Thomson effect, the supersaturation is related to the droplet diameter as follows:

$$\Delta\mu = \Delta\mu_0 - 4\Omega\alpha/d, \tag{5.1}$$

where $\Delta\mu_0$ is the potential difference for a planar surface, Ω is the atomic volume of Si and d is the droplet diameter. This results into a decrease of the growth rate for small droplets, *i.e.* thin wires.

Later reports have showed that it is possible to grow a large variety of semiconductor compounds by using this method. In the same way, besides Au, many metals can be used as catalyst, such as Ti, Al, Mn or Ni [168, 169].

A variation of this mechanism is the vapor–solid–solid growth (VSS). In this case, the growth is based on a solid–phase diffusion mechanism of a single component through a metal seed particle [170]. The growth is performed at temperatures below the eutectic point.

5.2.2 Self–assisted nanowire growth

Despite the success of catalyst–assisted nanowire growth for a big disparity of materials, such as group IV materials and III–V and II–VI compounds, the use of gold as catalyst has many drawbacks. The main one is the incorporation of gold through the catalyst droplet to the crystallographic structure, especially in defects such as stacking–faults [63]. Gold is a fast–diffusing metal that introduces deep level traps into the band gap of the semiconductor, resulting in a degradation of its electronic properties. Thus, the use of nanowires for optic or electronic applications requires a crystallographic structure free of impurities. For this reason, alternative growth mechanisms avoiding foreign metal seed particles have been proposed [171].

The different methods of synthesis can be grouped in two main categories: particle–assisted and particle–free growth. The first group comprises the above mentioned VLS and VSS concepts but replacing the metal catalyst by one of the elements constituting the wire [153, 154, 172–175]. Within the second group we can distinguish between selective area epitaxy

(SAE) [160–162, 176] and oxide–assisted growth (OAG) [177]. Both of them are based on the idea of suppressing the lateral growth to fabricate a one–dimensional structure. In the SAE case, the suppression is achieved by limiting the growth area with a low–sticking–coefficient mask layer with well–defined openings [178]. Thus, the diameter of the wire is largely determined by the size of the openings and a layer–by–layer vertical growth is enabled. The 1D growth is attributed to the formation of low growth–rate side facets [179]. OAG uses a *'semiconductor–rich'* oxide cluster as a seed nucleus. During the subsequent growth, oxygen atoms diffuse towards the edge forming an oxide shell which will prevent lateral growth.

5.2.3 InAs nanowire growth mechanism

The mechanism that rules the crystal growth of self–assembled InAs nanowires is still in debate and both particle–assisted and particle–free mechanisms have been reported.

Among the defenders of a particle–free growth, the group of Fukui showed that InAs nanowires grown in metalorganic vapor phase epitaxy (MOVPE) were composed of six vertical $\{\bar{1}10\}$ facets and (111)B plane at the tip, indicating a selective area epitaxy growth [162]. Previously, the same group reported about selective–area grown GaAs nanowires [179]. They analyzed the crystal structure depending on the substrate orientation and growth conditions. They

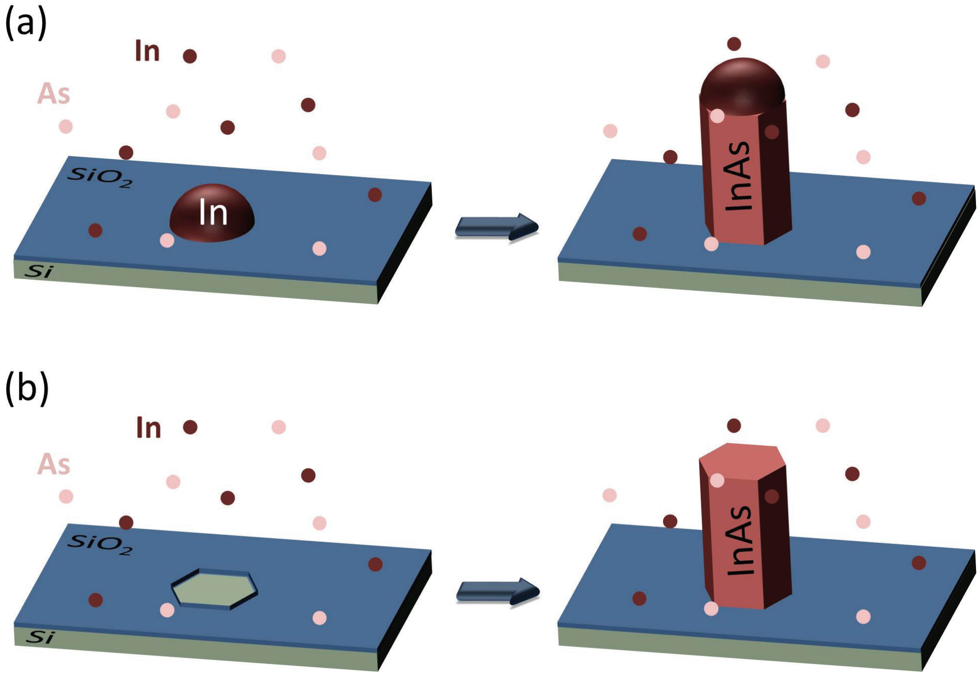

Figure 5.2: Schematic representation of the two InAs nanowires growth mechanisms: (a) Vapor–Liquid–Solid growth. An In particle is formed in the hole and acts as catalyst for the growth. (b) Selective Area Epitaxy. InAs nucleates in the openings of the SiO_2 mask and continues growing vertically.

achieved nanowire structures only on (111)B substrate at high temperature and low [AsH_3] conditions. These results dissent from a VLS hypothesis, in which nanowires tend to grow following the [111]B direction independently of the substrate orientation. Their theory was reinforced by demonstrating that the formation and growth rate of specific low–index facets were determined by the growth conditions. Hertenberger *et al.* also justified this theory by observing nontapered nanowires and an absence of InAs wetting layer [176].

On the other hand, Mandl *et al.* compared their experimental results with the predictions resulting from the different growth mechanisms [174]. The hypothesis of an oxide–assisted growth was rejected by studying the wire diameter when changing the growth time. This theory is based on the existence of an oxide sidewall that prevents lateral growth, which is in disagreement with the observed increase of diameter by time. Furthermore, they observed opposite trends for nanowire density and number of openings in the oxide mask with temperature, which is inconsistent with the theory of a selective area epitaxy. Thus, by performing further experiments using different substrate materials and adding an interruption step during the growth, they proposed a mechanism based on the VLS concept using In as a catalyst. The oxide layer role is to immobilize In droplets restricting its size and making nanowire nucleation possible, and the density of wires is temperature–dependent as the diffusion length of In also depends on temperature. They finally suggested that In droplet crystallizes into an InAs tip during cooling, since the AsH_3 flow is maintained during this step to avoid wire decomposition. Figure 5.2 illustrates the two different growth mechanisms.

In the following, we consider the contribution of diffusion of adatoms to the oxide openings, desorption of adatoms from SiO_2 and shadowing from the neighboring nanowires to the growth of InAs nanowires on patterned Si substrate. The three effects are evaluated theoretically and compared to the experimental results.

5.3 Sample Preparation

In order to position control the nanowires a pre–growth nanopatterning of the substrate is required. Thus, a layer of 20nm thermally–grown SiO_2 was used as a mask to define the pattern on a 2–inch <111> *p*–doped Si wafer with a resistivity of 0.1–0.5 Ω·cm. 90 nm of ZEP520A resist (consisting of 11% methyl styrene and chloromethyl acrylate copolymer and 89% anisole), diluted 50% in anisole was spin–coated before performing an electron beam lithography. Hole arrays with nominal diameters of 45 nm and spacings (measured from center to center) ranging from 200 nm to 10 μm were then transferred to the silicon wafer by exposing the samples to a short O_2 plasma (descum) to remove any resist residuals and dipping them in a solution of buffered hydrofluoridric acid (BHF, 7:1) for 12 s. Finally, a long O_2 plasma strip was performed to completely remove all the ZEP resist. After the process, the real diameter was in average 110 nm.

To ensure a perfectly clean and oxide–free surface in the holes a 2 s BHF dip followed by a 3 min deionized (DI) water rinsing was performed before keeping the sample in isopropyl alcohol

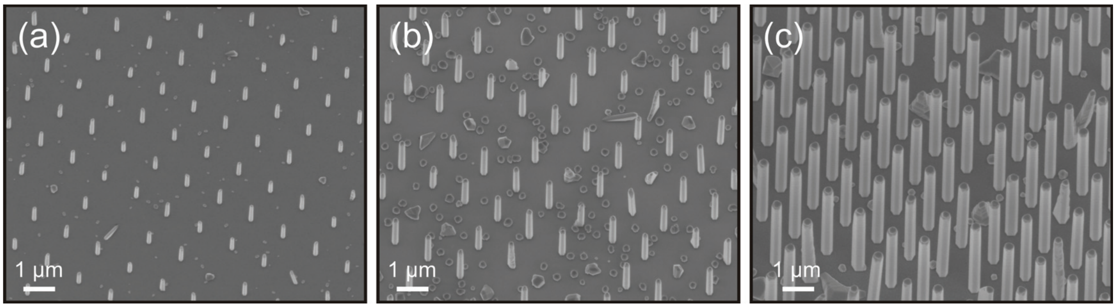

Figure 5.3: SEM images tilted 25° of nanowire arrays grown for (a) 1 h, (b) 2 h, and (c) 5 h. The spacing in the three cases is 1200 nm.

until its introduction in the MBE load lock. The substrates were subsequently introduced in the degassing chamber and heated up at 600°C for 2 h in order to degas any remaining organic residuals. Just before the growth, they were loaded in the growth chamber and heated to around 800°C for 30 min to further remove any possible contaminants. Finally, the growth was carried out at 500°C and with a nominal In growth rate of 0.2 Å/s, As_4 partial pressure of 6 $\times 10^{-6}$ Torr and with 7 rpm rotation. Temperature was calibrated using a pyrometer on the sample holder. Under these conditions, three growths were performed for 1, 2 and 5 hours. A picture of the three growths for a pitch of 1200 nm is shown in Figure 5.3. The growth of InAs nanowires was homogeneous over the array area for all spacings.

5.4 Results

Despite the intense debate around the mechanism leading the growth of InAs nanowires, we have not found any investigations to correlate nanowire spacing with its volume and geometrical characteristics. This kind of study can give us access to physical parameters such as the diffusion length of adatoms. In order to do so, three different growths were carried out changing the growth time to 1, 2 and 5 hours. Top and bottom diameters as well as the length were measured over 30 nanowires for each spacing. The volume was calculated considering nanowires as truncated cones.

We analyzed the diameter and length of the nanowires for the same hole size as a function of the spacing. Figure 5.4a and 5.4b show the evolution of the nanowire length and tip diameter, respectively, as a function of the pitch for the three different growth times. The nanowire length seems to follow a *competitive growth regime* to *diffusion–limited growth regime* transition [161]. For pitches equal or above half of the diffusion length, adatoms collection is constant and limited by the number of adatoms that impinge within a circle whose radius is equal to the diffusion length. This regime is called *diffusion–limited growth*. However, in our case the diffusion lengths resulting from this theory change from 400 to 1000 nm with the growth time (but the same growth conditions). On the other hand, for pitches below half of the diffusion length, adatoms are distributed equally over all the holes. As holes compete against each other

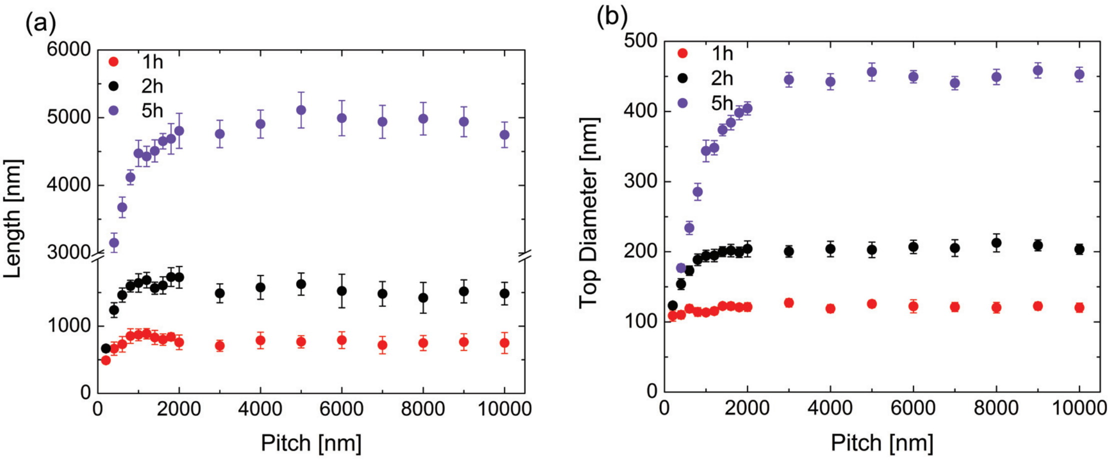

Figure 5.4: Geometrical characteristics as a function of the pitch: (a) length, and (b) tip diameter. Statistics of the three growths are performed on 45–nm holes.

to adsorb an adatom, this regime is called *competitive growth*. In this regime, wires should grow both, axially and radially, with the spacing. Figure 5.4b shows that for a 1–hour growth the diameter does not change with the spacing, what is also contradictory with the model. Thus, in order to study more accurately the growth mechanism, we will analyze the relation between the volume of the nanowire and the spacing between them, as it includes the total amount of incorporated adatoms.

5.4.1 Theoretical Model

To understand better what guides the growth synthesis, we will simplify it by dividing the whole process in four different processes [180]:

- Adsorption
- Diffusion
- Desorption
- Incorporation

The income vapor flux impinges onto the substrate and only a certain amount of the source flux will physisorb onto the surface. This phenomenon is called *adsorption*. Adsorption of atoms from their vapor phase to a solid surface occurs when attractive forces act at short distances between them (process 1 in Figure 5.5).

Opposite to adsorption is desorption (process 3 in Figure 5.5). Desorption of arsenic is very rapid while indium desorption becomes important at temperatures above 500°C. Hence, for

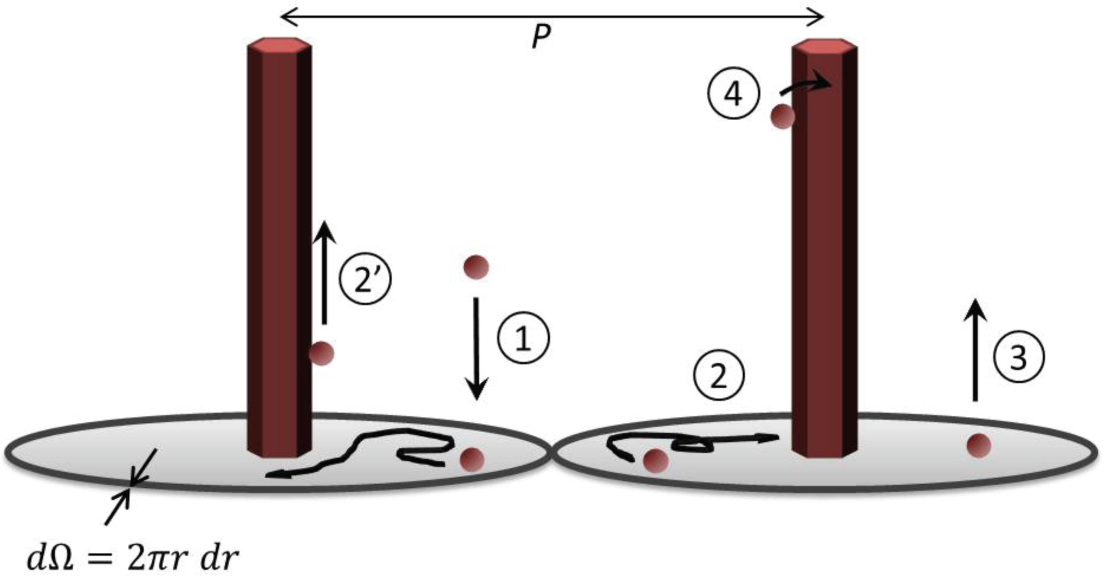

Figure 5.5: Sketch of the kinetic processes considered in the nanowire growth: (1) adsorption, (2) diffusion on the substrate, (2') diffusion along the nanowire sidewalls, (3) desorption, and (4) incorporation.

conventional growth, the growth rate is limited by the group III element. The desorption rate is given by the Arrhenius equation:

$$-\frac{\mathrm{d}\theta}{\mathrm{d}t} = \nu_{\perp}\ \exp\left(-\frac{E_{\mathrm{d}}}{kT}\right), \tag{5.2}$$

where $\nu_{\perp}$ is the vertical vibration frequency of the adatom and E_{d} is the activation energy for desorption. For diffusion to occur, E_{d} should be bigger than E_{A}.

Once the atom is adsorbed it diffuses over the surface following the Einstein diffusion equation:

$$\frac{\partial\, p(x,y,t)}{\partial t} = D \cdot \nabla^2 p(x,y,t), \tag{5.3}$$

where the function *p(x,y,t)* describes the probability of finding a particle at the position (*x,y*) at the time *t* and *D* is the diffusion coefficient or diffusivity defined by:

$$D = \nu_{-}\ \exp\left(-\frac{E_{\mathrm{A}}}{kT}\right). \tag{5.4}$$

ν_{-} is the horizontal vibration frequency and E_{A} is the activation energy required to jump to a new position. Since the activation energy depends on the temperature and on the nature of the substrate, the diffusivity on the SiO_2 layer and on the uncovered Si substrate will differ, leading to a gradient of concentration. For the sake of simplicity, we can assume that the gradient of concentration points towards the center of the nearest Si hole, meaning that the adatom distribution changes only on the direction of the gradient vector, $\vec{r}$. Thus, equation 5.3 can be converted to a one–dimensional diffusion equation:

$$\frac{\partial\, p(r,t)}{\partial t} = D \cdot \frac{\partial^2\, p(r,t)}{\partial r^2}, \tag{5.5}$$

with the initial condition:

$$p(r, t \to 0) = \delta(r - r_0) \tag{5.6}$$

and the boundary condition at r→ ∞:

$$p(r \to \infty, t) = 0. \tag{5.7}$$

If we consider Si holes as absorbing points, *i.e.*, a point that absorbs every atom impinging on it, the other boundary condition will be defined by:

$$p(r = 0, t) = 0 \tag{5.8}$$

The analytical solution to this problem is [181]:

$$p(r,t) = \frac{1}{\sqrt{4\pi D t}} \exp\left[-\frac{(r-r_0)^2}{4D(t-t_0)}\right] - \frac{1}{\sqrt{4\pi D t}} \exp\left[-\frac{(r+r_0)^2}{4D(t-t_0)}\right], \quad r \geq 0. \tag{5.9}$$

The second term in equation 5.9 corresponds to particle removal by the absorbing point, *i.e.* an atom that has been incorporated in the nanowire (formation of a chemical bond, process 4 in Figure 5.5). Thus the total amount of particles removed by the absorbing point is:

$$\begin{aligned} N(r,t) &= 1 - \int_0^\infty p(r,t)\, \mathrm{d}r, \\ &= \mathrm{erfc}\left[\frac{r_0}{\sqrt{4D(t-t_0)}}\right]. \end{aligned} \tag{5.10}$$

The value of $(t - t_0)$ is determined by the lifetime, τ, of In atoms on the surface and their diffusion length is characterized by $L_\mathrm{D} = \sqrt{D\,\tau}$.

To obtain the final volume of the nanowire, we just need to integrate equation 5.10 over the surrounding collecting area (which in our case is a circle of radius half of the pitch (P)) and add the adsorbed volumetric flux, Q_s. Q_s is described by,

$$Q_\mathrm{s} = Q_0 \cdot (1 - r_\mathrm{des}), \tag{5.11}$$

where Q_0 is the incoming volumetric flux and r_des is the desorbed fraction.

Therefore, the final expression is:

$$V = Q_\mathrm{s} \int_\Omega N(r,t) \; = Q_s \int_0^{P/2} \mathrm{erfc}\left[\frac{r_0}{2L_\mathrm{D}}\right] 2\pi r \,\mathrm{d}r,$$

$$V = Q_s \,\frac{\pi}{2} \left[4L_\mathrm{D}^2 \,\mathrm{erf}\left(\frac{P}{4L_\mathrm{D}}\right) + \frac{P}{2} \left(P \,\mathrm{erfc}\left(\frac{P}{4L_\mathrm{D}}\right) - \frac{4L_\mathrm{D} \,\exp\left(\frac{-P^2}{16L_\mathrm{D}^2}\right)}{\sqrt{\pi}} \right)\right]. \tag{5.12}$$

Finally, incorporation can occur either from the sidewalls or from the tip. As the nanowires are composed by non polar {110} side facets and a polar (1-11)B plane at the tip, the incorporation rate is faster axially than radially.

5.4.2 Experimental Results

In this section, the presented theoretical model is compared to the experimental data obtained from the three growths. The growth conditions in the three cases are the same and only the growth time was changed to 1, 2 and 5 hours. In Figure 5.6 the volume of the nanowires is plotted as a function of the spacing. The nominal diameter of the oxide openings is 45 nm and the spacings vary from 200 nm to 10 μm. Data points are fitted by equation 5.12 and the parameters resulting from the fitting are summarized in table 5.1.

Table 5.1: Diffusion length, L_D, total adsorbed flux, Q_s, and desorbed fraction, r_des obtained from the fitting of the volume vs pitch.

Growth time (h)	L_D (nm)	Q_s (nm)	Q_0 (nm)	r_des
1	237	29.5	72	0.59
2	409	54.8	144	0.62
5	1130	125.7	360	0.65

The total adsorbed flux, Q_s, increases in a proportional manner with time. From the nominal In growth rate (0.2 Å/s) the total incident volumetric flux for each growth can be calculated and, hence, the desorbed fraction is also obtained. As shown in table 5.1, the resulting desorbed fraction is around 0.6, increasing slightly with the growth time. This yields a desorption rate of $-\mathrm{d}\theta/\mathrm{d}t \simeq 0.12$ Å/s at 500°C.

From the fittings, the diffusion length of In adatoms was also obtained. In order to do so, we should consider the shadow effect originated by the neighboring nanowires [182]. Considering that the incident beam is tilted 60° from the substrate plane, the maximum length of the nanowire for being free from shadowing is defined by $h = P \cdot \tan 60$ (Figure 5.7). When nanowires become longer than h, the majority of the incident In atoms impinge directly on the nanowire and diffuse along its sidewall. This means that for nanowires long and close

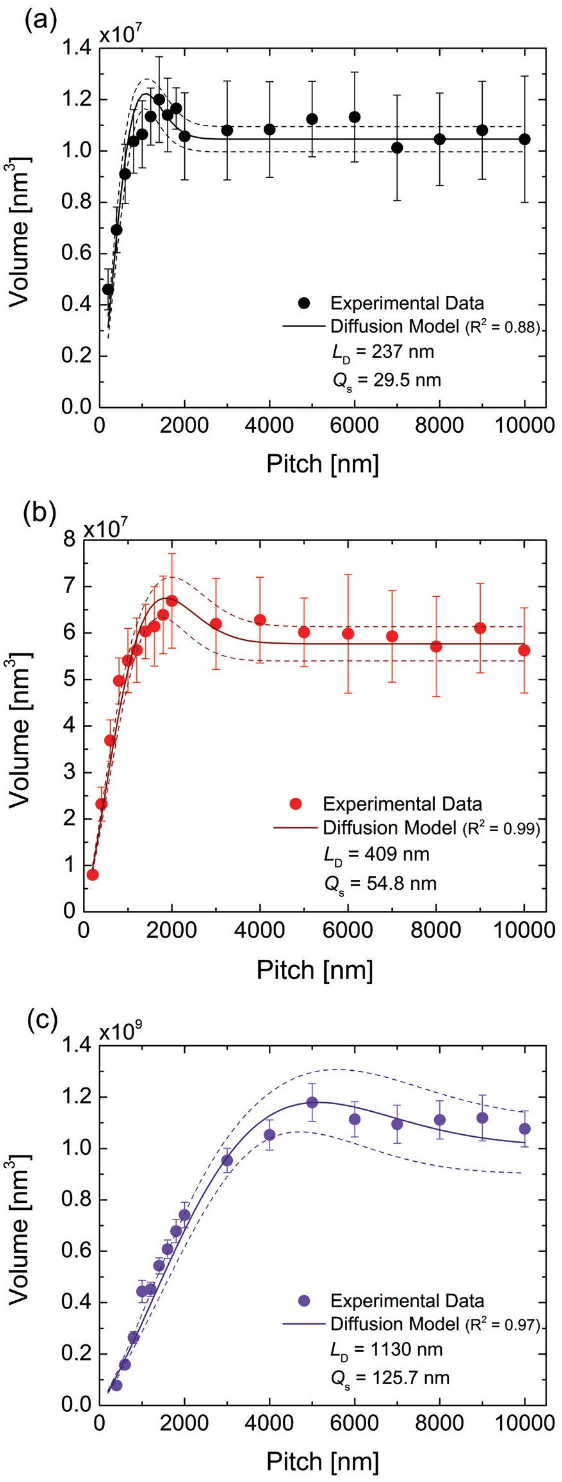

Figure 5.6: Average volume of nanowires as a function of the pitch for three different growth times (a) 1 h, (b) 2 h, and (c) 5 h. Solid lines show the fitting of Equation 5.12 to the experimental data.

each other enough to be affected by shadowing, the diffusion length obtained from the fitting includes proportional contributions from the diffusion length of adatoms diffusing on the silicon oxide substrate and the diffusion length of adatoms impinging directly on the nanowire and diffusing along the InAs sidewall.

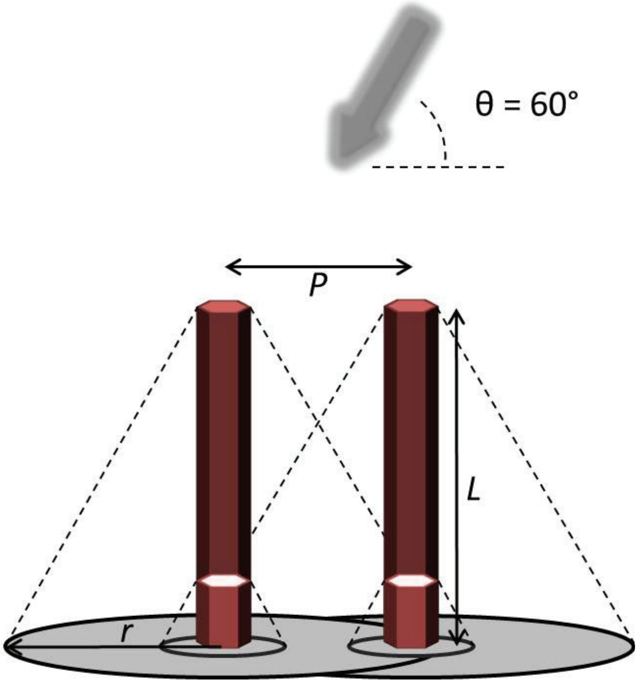

Figure 5.7: Schematic of the nanowire growth illustrating the shadowing effect (*P* denotes the pitch between wires, *L* is the length of the nanowire, *r* is the radius of the shadowed area and θ is the angle of the beam flux respect to the substrate plane). When the wires reach a certain height a fraction of the incident flux will be captured by the neighboring nanowire.

Nanowires grown for 1 hour are shorter than h for all pitches. Thus, we can consider that almost all the atoms have been incorporated into the nanowire after diffusing on the oxide. Therefore, the diffusion length calculated for this growth is the diffusion length of In adatoms on silicon oxide, which is around 240 nm.

A lower bound of the diffusion length of In adatoms on InAs(110) can be estimated from the 5–hour–growth sample (L_D = 1.1 μm). In this case, nanowires are affected by shadowing. As the diffusion length of In adatoms on InAs is larger than on SiO_2, L_D on InAs cannot be smaller than 1.1 μm.

The upper bound can be determined from nanowires tapering. InAs nanowires present a pronounced tapering due to the contribution of adatoms diffusing from the substrate to the lateral growth (Figure 5.8a). In Figure 5.8b the bottom diameter/top diameter ratio for the three different samples are compared. For pitches larger than 3 μm, since there is no shadowing from the neighboring nanowires, the ratio between the tip diameter and the base diameter

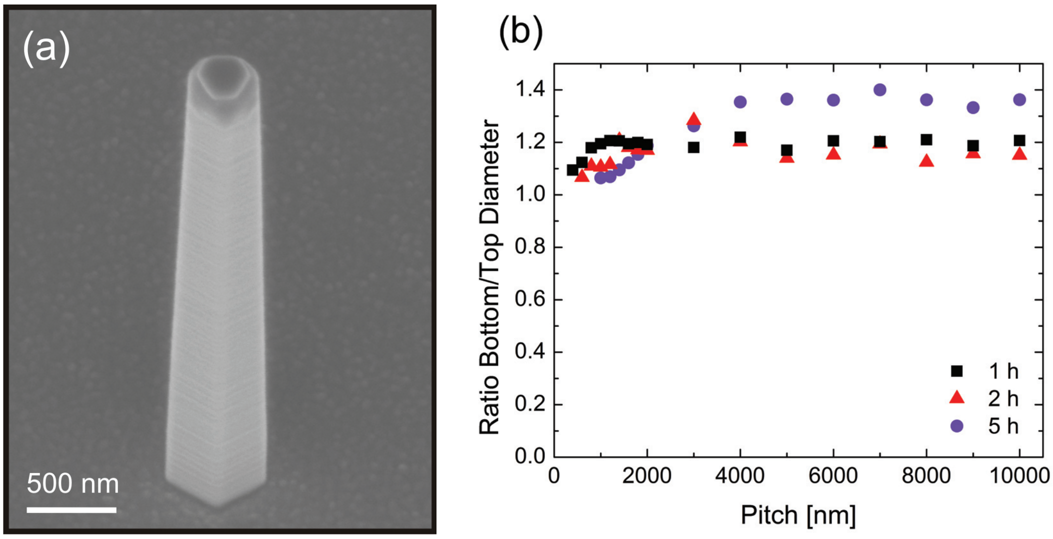

Figure 5.8: (a) SEM tilted view of a grown InAs nanowire exhibiting a pronounced tapering. (b) Ratio bottom/top diameter depending on the pitch. For large spacings, there is no shadowing from the neighboring wires and the ratio between the tip diameter and the base diameter becomes independent of the pitch.

becomes independent of the distance between wires. The ratio is around 1.2 for 1–hour and 2–hour growth samples, while for the longer growth the tapering is more pronounced (ratio of 1.35). This can be attributed to the diffusion length of adatoms on the nanowire surface: L_D is smaller than the nanowire height and adatoms diffusing from the substrate cannot reach the tip. Then, the lateral growth at the tip is only induced by atoms impinging directly on the sidewall. Hence, the diffusion length of adatoms on InAs is smaller than the height of the nanowires grown for 5 hours, which is around 5 μm. These results confirm that the adatoms diffusion length on the InAs(110) sidewall is between 1.1 and 5 μm, which is in good agreement with the 1.5 μm reported by Tchernycheva *et al.* [183].

5.5 Application to Solar Cells

The achievement of ordered arrays of vertical InAs nanowires on top of *p*–doped silicon substrate gives us the chance to study the performance of the heterostructure formed between InAs and *p*–Si as a solar cell. Even though the grown InAs nanowires are not doped, InAs surfaces are known to possess a high concentration of donor–type surface states, which results in an electron accumulation layer and, consequently, Fermi level pinning [184]. Thus, it creates a *p*–Si/*i*–InAs/*n*–InAs structure.

The growth of InAs nanowire arrays is described in Section 5.3. In this case and in order to make a device, the substrate was patterned with a 1.5×1.5 mm^2 array of holes with a diameter of 100 nm and a pitch of 800 nm. The wires were grown at 500°C, with an arsenic partial pressure of 6×10^{-6} Torr and a rotation of 7 rpm for 1 h. The indium cell was heated up to

790°C, which is equivalent to a nominal In growth rate of 0.2 Å/s. Under these conditions, 2–μm long wires were obtained with diameters around 168 nm. A SEM picture of the as–grown wires is depicted in Figure 5.9a. After the growth and in order to electrically insulate the *p*–doped Si substrate from a subsequent front contact, wires and substrate were covered by a 17–nm thick conformal layer of sputtered SiO_2 (Figure 5.9b). Then, wires were embedded in a polymer matrix which would act as an etch barrier for the oxide located on the substrate. For this purpose, photoresist AZ1512HS was spin–coated at 1700 rpm for 1 min and baked at 120°C for 5 min, obtaining an homogeneous film of 2050 nm (Figure 5.9c). Afterwards, the resist layer was etched down for 2 min using an O_2 induced coupled plasma (ICP)(Figure 5.9d). A controlled etch was achieved by using an electrostatic chuck power of 100 W and an ICP source power of 600 W. The remaining photoresist thickness was around 275 nm. The sputtered oxide

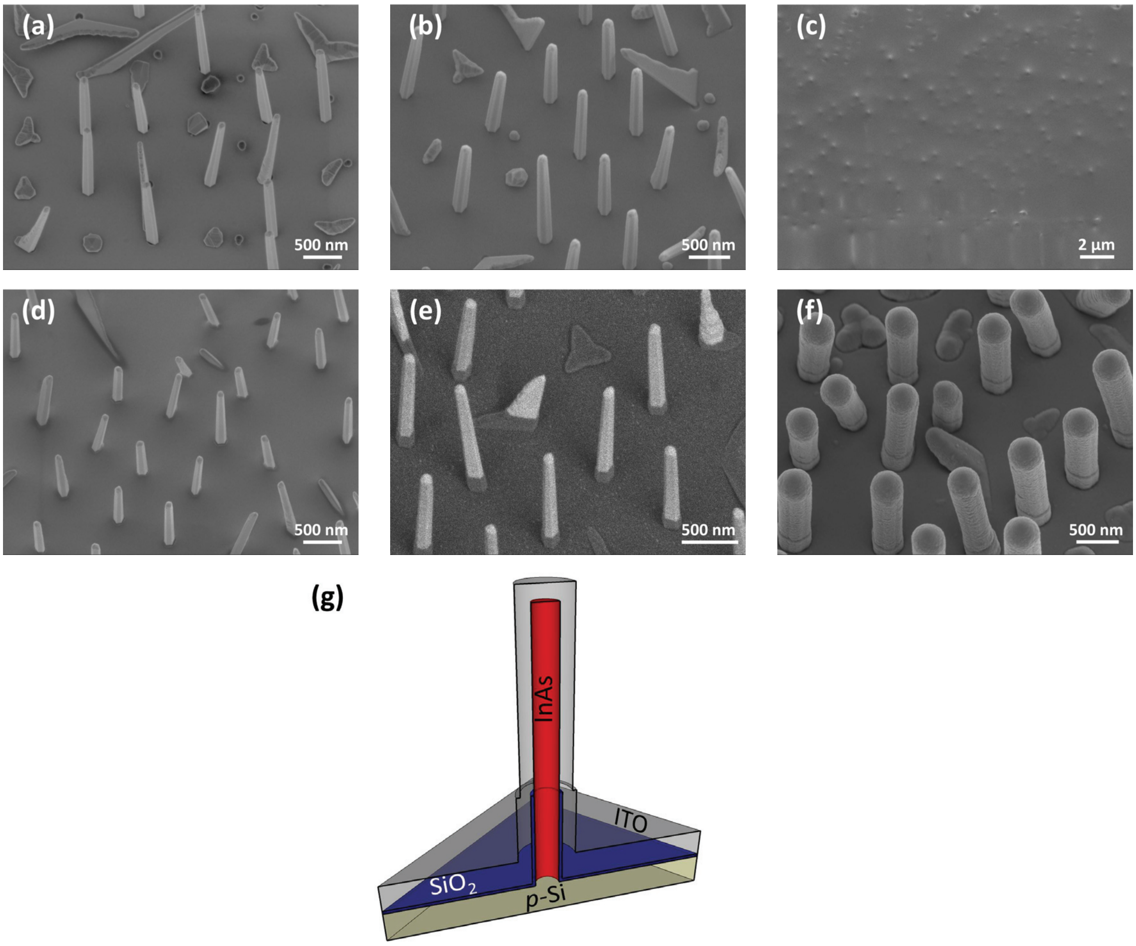

Figure 5.9: 20° tilted SEM images of the fabrication process. (a) As–grown InAs nanowires array on a *p*–doped Si substrate. (b) Sputtering of 45 nm of SiO_2. (c) Spin–coating of 2–μm thick AZ1512HS photoresist. (d) Partially etched photoresist and removal of the unprotected oxide. (e) Removal of the remaining photoresist. (f) Sputtering of ITO front contact. (g) Schematic of the final device composed by a Si–InAs *p*–*n* heterojunction.

covering the polymer–free part of the wires was removed by dipping the samples in BHF, 7:1 solution for 45 s (Figure 5.9e). Before depositing the front contact, a last O_2 plasma removal was carried out to clean the sample from any organic residue. Finally, 200 nm of aluminium were sputtered on the backside and 500 nm of ITO on the front side (Figure 5.9f). On top of the ITO, a layer of 10 nm of Ti and 200 nm of Au was evaporated through a metallic mask all around the arrays to have a better contact with the probe tip. A sketch of the final device is depicted in Figure 5.9g.

The current–voltage characteristics were measured in the dark and with a sun simulator under illumination conditions of AM1.5G. An example of the resulting curve is shown in Figure 5.10. The open–circuit voltage and fill factor are respectively 310 mV and 0.32. The short–circuit current density obtained was 14 mA/cm^2, taking into account the total area of the array (2.25 mm^2), resulting in an efficiency of 1.4% (the Shockley–Queisser limit for an InAs single junction is around 6%). However, if we only consider the junction area, which is the interface between Si substrate and InAs nanowires (~8.00×10^{-4} cm^2), the short–circuit current density rises up to 392 mA/cm^2. The maximum power generated is 31.7 μW which gives an apparent efficiency for each individual nanowire of 39.6%.

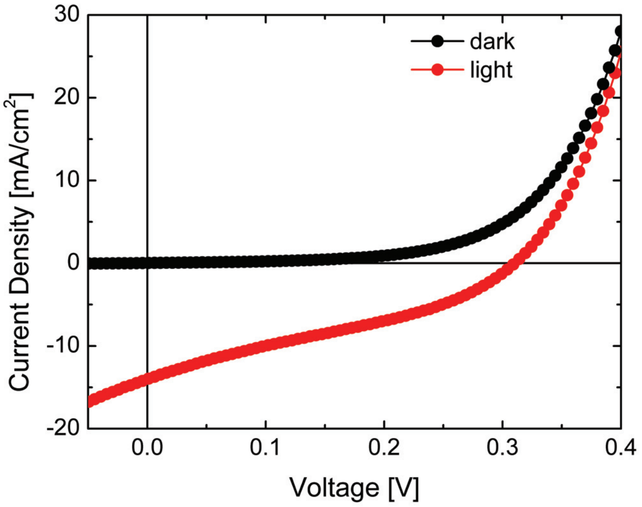

Figure 5.10: I–V characteristic curve of InAs nanowire arrays on *p*–doped Si in the dark and under AM 1.5G illumination.

To further analyze the spectral response of the photocurrent, the external quantum efficiency (EQE) was also measured as shown in Figure 5.11a. The overall photoresponse is dramatically low and it presents a peak between 700 and 800 nm. Finite Difference Time–Domain (FDTD) simulations [90] were performed to understand the light absorption in the device and are plotted in Figure 5.11b. The structure simulated was composed by an array of InAs nanowires standing on a 1 μm thick Si substrate. The nanowires have a diameter of 160 nm, a length of 2μm, 800 nm of pitch, a layer of 17 nm of silicon dioxide covering the substrate and a layer of 150 nm of ITO as front electrode. An incoming plane wave polarized along the x–direction and approaching the structure at normal incidence was modeled. According to the

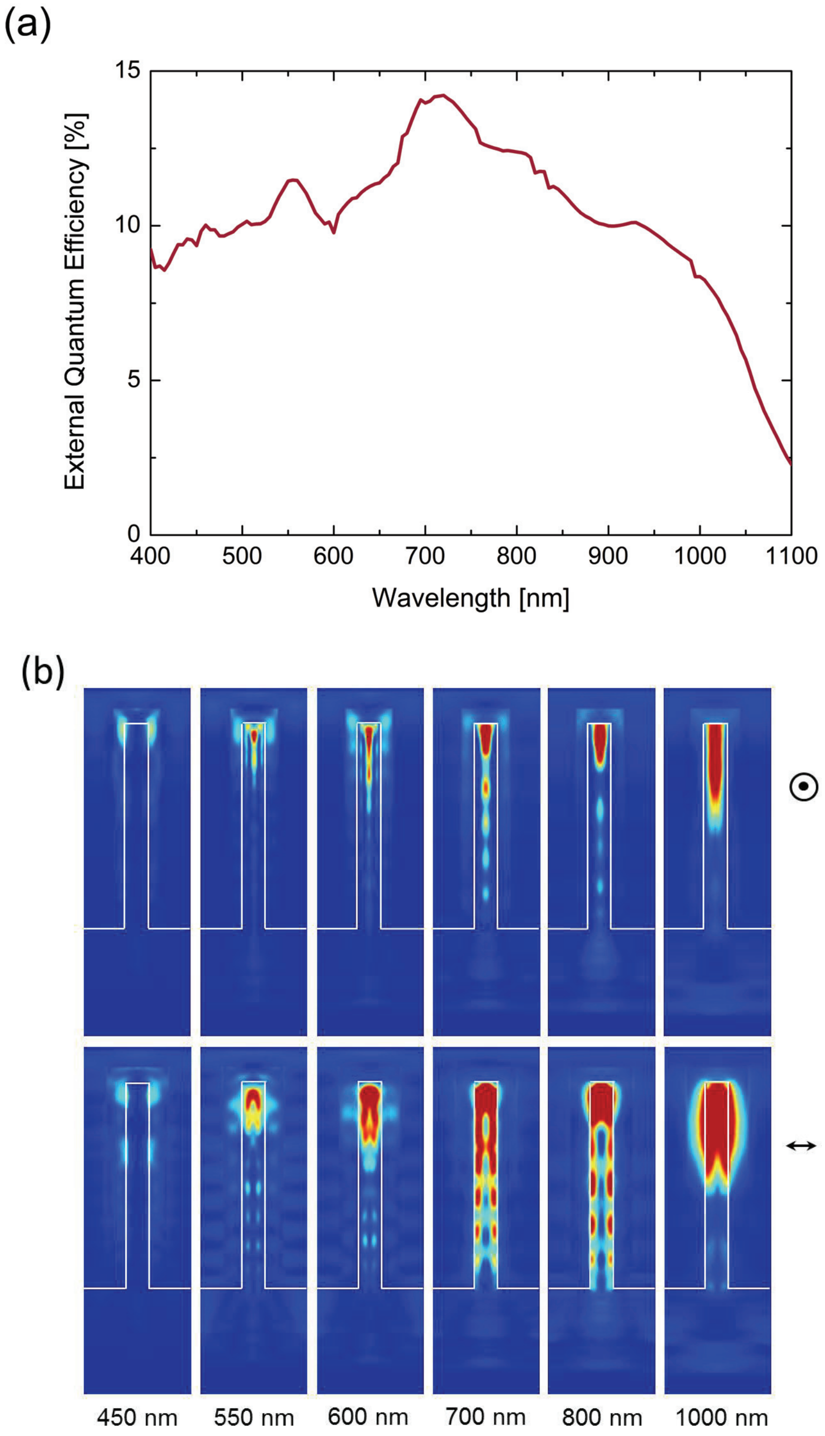

Figure 5.11: (a) External quantum efficiency (EQE) of *i*–InAs nanowires on *p*–doped Si substrate. (b) FDTD simulated cross–sections of the electric field energy density (above: cross–section at x= 0; below: cross–section at y= 0) at 450, 550, 600, 700, 800 and 1000 nm.

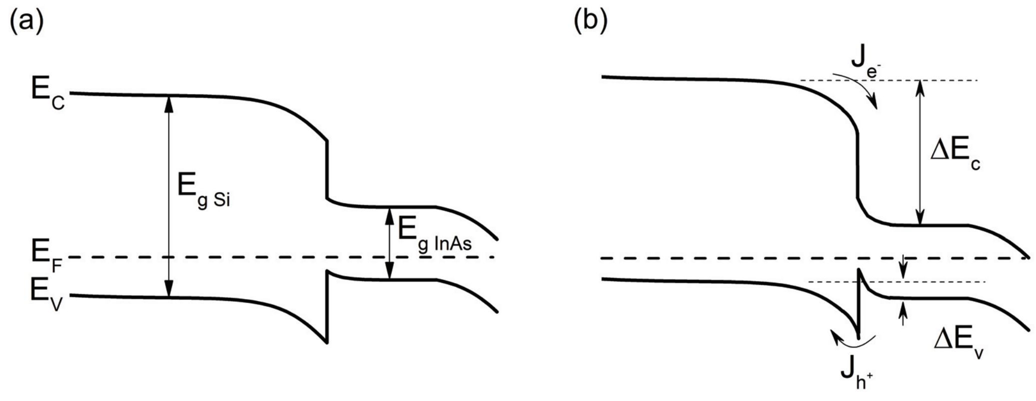

Figure 5.12: Band diagram of Si/InAs heterojunction at thermal equilibrium in (a) dark and (b) under illumination. J_{h^+} denotes hole tunneling current and J_{e^-}, current due to electrons drift.

simulations, for most of the wavelengths light is absorbed mainly at the upper part of the nanowire except for the range of wavelengths from 700 to 800 nm, in which light is absorbed more homogeneously along the wire and also a small fraction is absorbed in the Si substrate.

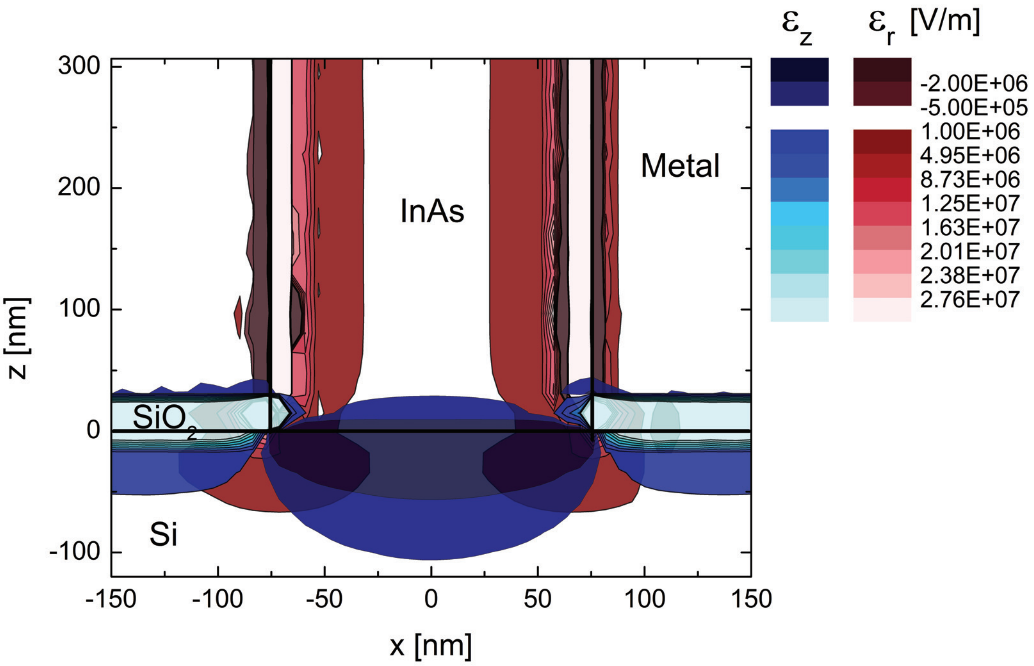

Figure 5.13: Axial and radial components of the calculated built–in electric field. For the calculations, we considered an *i*–InAs nanowire of 150 nm of diameter standing on a *p*–Si substrate (doping concentration of 4×10^{-14} cm^{-3}).

If we now have a look at the calculated band diagram of the heterostructure in the dark and under illumination depicted in Figure 5.12, we can observe that the valence band is barely bent while the conduction band offset is much larger. Thus the band alignment favours the flow of electrons from the silicon substrate to the InAs nanowire while it screens the flow of holes from InAs to Si. To further illustrate this, we calculated the built–in electric field at the heterojunction with the software package next**nano**^{3} [89]. For the calculations, we considered a cylindrical *i*–InAs nanowire with a diameter of 150 nm standing on a *p*–doped Si substrate (doping concentration of 4×10^{14} cm^{-3}). Figure 5.13 depicts the axial and radial electric field at the junction. As it can be clearly seen, the depletion region in the Si substrate is much larger than the depleted volume in the InAs nanowire. Moreover, it is well known that InAs nanowires content a lot of stacking defects [185], leading to a small diffusion length of carriers. Then, most of the carriers generated at the nanowire will be lost by recombination before reaching the junction by diffusion. These results explain the low values of the quantum efficiency. On the other hand, the peak at around 700–800 nm is from the light absorbed closer to and in the Si substrate, as electrons are better collected thanks to the higher electric field at this area.

The origin of the generated photocurrent could be localized by spatially resolved photocurrent measurements. This technique also allows to determine the diffusion length of electrons in the silicon substrate. The nanowire array was mounted on a x–y piezostage and illuminated

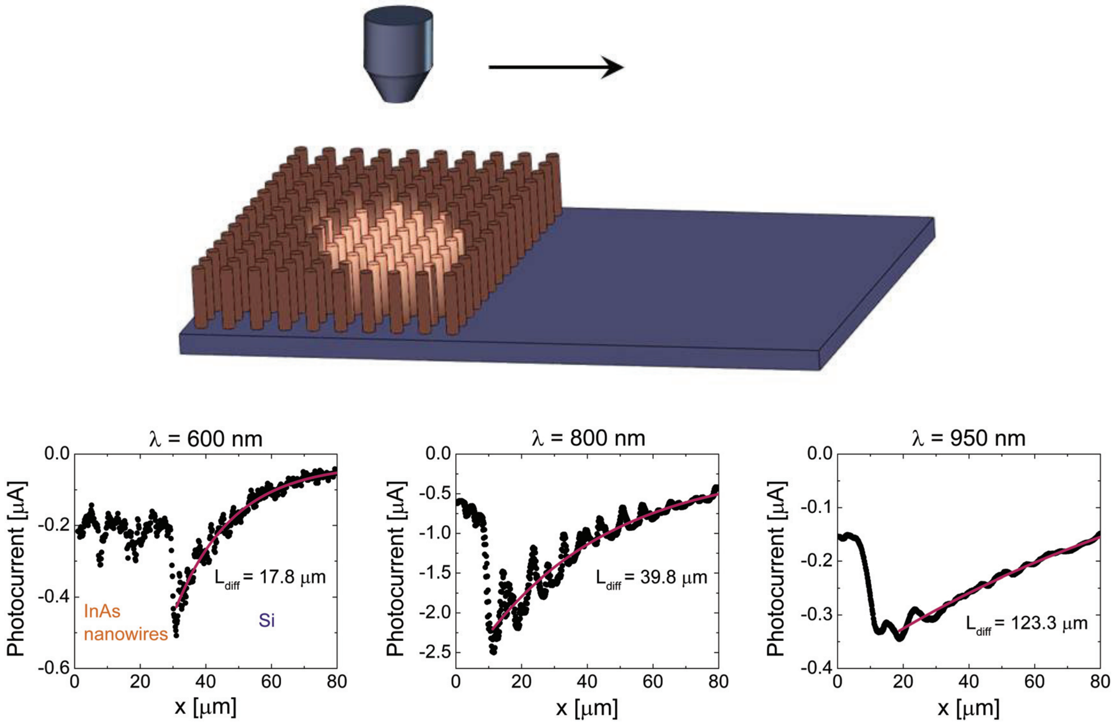

Figure 5.14: Schematic of the photocurrent line–scan measurement and photocurrent profiles at 600, 800 and 950 nm. The red line shows the fitted photoresponse exponential decay versus distance from the heterojunction.

with a wavelength of 600, 800 and 950 nm and a spot diameter of 976, 1301 and 1545 nm, respectively. The photocurrent was line–scanned along 80 μm, from the InAs nanowire array to the silicon substrate, away from the junction. Figure 5.14 shows the current generated in the Si/InAs heterojunction and the exponential decay dependence on the distance from the junction for each wavelength. The response is quite homogenous when the light spot is placed on the nanowires and increases significantly when the uncovered silicon substrate next to the junction is illuminated. Then the photoresponse decreases exponentially when moving away from the array. These results confirm what stated above: the light is mainly absorbed within the wires and, because of the energy–band alignment, the current is generated by the holes diffusing from InAs to Si. Nevertheless, when light is absorbed within the silicon, electrons are attracted from the silicon to the junction by the built–in electric field created by the conduction band offset. The photoresponse profile at the InAs–to–Si transition becomes less sharp with the wavelength because the spot of the light increases linearly with it.

On the other hand, the diffusion length of minority carriers in silicon can be extracted from the exponential decay of the photoresponse versus the distance from the junction by the following expression:

$$I_{\mathrm{ph}} \propto \exp\left(-\frac{d}{L_{\mathrm{diff}}}\right), \tag{5.13}$$

where I_{ph} is the photocurrent, d is the distance from the junction and L_{diff} is the diffusion length. The diffusion lengths obtained were 17.8, 39.8 and 123.3 μm for a wavelength of 600, 800 and 950 nm, respectively. This increase is due to the surface effect: longer wavelengths are absorbed deeper inside the silicon, where there is lower density of traps and, hence, lower recombination rate. However, all values should increase when illuminating with higher intensities. It follows from equation 3.1 that when the density of carriers is lower than the density of traps, the recombination rate presents a constant maximum dominated by the concentration of traps. Then, for higher densities of carriers the recombination rate decreases, leading to an enhancement of lifetime over one order of magnitude [186], which would be in agreement with values reported in Table 2.1 for surface lifetimes and in literature for bulk lifetimes.

Therefore, the potential of InAs nanowire arrays on Si as a solar cell could be further improved by increasing the spacing between wires. In this way, more light could be absorbed in the silicon substrate by keeping the antireflective function of nanowires.

5.6 Conclusions

Ordered arrays of vertical InAs nanowires on a patterned SiO_2/Si substrate were grown by means of molecular beam epitaxy. A theoretical model based on the diffusion of adatoms to the oxide openings and desorption of In adatoms was proposed and fitted to the nanowire volumes obtained from three different growth times. The diffusion length and desorption rate of In adatoms on oxide were calculated and resulted to be approximately 240 nm and 0.12 Å/s, respectively, for a growth temperature of 500°C, a nominal In growth rate of 0.2 Å/s and As_4 partial pressure of 6×10^{-6} Torr. Also the diffusion of In adatoms on InAs sidewalls was considered to explain nanowires tapering. This study gave us access to the diffusion length of In adatoms on InAs, resulting in a value ranging between 1.1 and 5 μm.

Finally, the heterojunction formed by InAs nanowires on *p*–doped Si was evaluated as a solar cell. We obtained a J_{sc} and an efficiency of 14 mA/cm^2 and 1.4%, respectively, considering the total projected area of the array. The external quantum efficiency results showed a very low photoresponse of the device. It was demonstrated that the light is mostly absorbed within the InAs nanowires and photocurrent is limited by the small valence band offset, which creates a small drift current of holes from InAs to Si. However, the current of electrons from Si to InAs is more favourable due to a high conduction band offset. Thus, the device performance could be significantly improved by increasing the spacing between wires, which would lead to a higher absorption of light within the substrate and higher photocurrent. Finally, the diffusion length of minority carriers in the silicon substrate was shown to be strongly affected by the surface recombination.

6 Summary

In this last chapter the main results achieved throughout this thesis are highlighted. The prospects of nanowires for high photon–to–electron conversion efficiency have been explored. The main points covered in it are the engineering of the radial junction, the influence of surface recombination on the overall performance of the device, the implementation of a highly conformal metal nanoparticle film as front electrode and the integration of III–V nanowires on silicon.

Semiconductor nanowires exhibit unique electrical, optical, magnetic and mechanical properties due to their quasi–one dimensional structure. In recent times they have been explored for electronic, optoelectronic and sensor applications. In this work, we have addressed different aspects of the system that may influence on the performance of the final device for photovoltaic purposes. The main results accomplished in this thesis are summarized below.

In chapter 2, the influence of the microwires geometry and doping level on the photovoltaic performance has been explored. With this aim, a top–down method to obtain radial junction silicon microwire solar cells has been developed. Energy conversion efficiencies of 10.13% were achieved on solar cells with 29 mm^2 areas. Microwire arrays showed good light absorption properties, being the absorption linearly dependent to the microwire length. However, this did not necessarily lead to higher short–circuit current densities: long microwires suffer from higher surface and junction recombination losses, which cancel out the benefits from the light absorption enhancement. In addition, studies on the *p*– and *n*–doping levels revealed that the doping of the core should be kept low in order to reduce bulk recombination and its radius should be smaller than the diffusion length of minority carriers. On the other hand, the shell should be highly doped and as thin as possible to limit emitter losses. Finally, both core diameter and shell thickness should be scaled with the depletion width in order to avoid a fully depleted structure.

The impact of the surface recombination on the photovoltaic properties of axial *p*–*n* junction silicon nanowires has been studied in chapter 3. Nanowire arrays have been defined by Near–Field Phase–Shift Lithography, a method based on traditional optical lithography which allows the obtention of submicron structures. It has been shown that the reduction of the recombination velocity contributes to a significant enhancement of both the open–circuit voltage and the short–circuit current, resulting in higher efficiencies. Four different passivation layers have been tested: ALD Al_2O_3, thermally grown SiO_2, PECVD SiN_x and a thermal SiO_2/ PECVD SiN_x bilayer. It has been demonstrated that an improper field–effect passivation could lead to higher losses. For instance, positive fixed charges on *p*–type silicon causes carrier inversion. In the case of low doping level, a high concentration of fixed charges (introduced by the SiN_x layer) results in inversion conditions across the whole nanowire cross–section, shifting the junction to the base of the wire. On the other hand, lower densities of fixed charges (in the case of the SiO_2/Si interface) can cause the electron and hole densities to become equal within the nanowire diameter, which favours the recombination. The same is applicable for negative fixed charges (in the Al_2O_3/Si system) on *n*–type silicon. The addition of a hydrogen–containing capping layer on the thermally grown SiO_2 suppresses the fixed charges at the interface and improves the chemical passivation, giving rise to a great improvement of the device performance.

In chapter 4, we have proposed a novel method to coat complex 3D structures with a conformal metal nanoparticle film. Gold and silver nanoparticle networks were synthesized via a polymer–brush–guided method generated by surface–initiated polymerization. A uniform coverage across the entire surface has been achieved following this approach. Moreover, the dependency of the type, size, shape and density of the particles on the polymer matrix thickness has been demonstrated. Both films present good conductive properties and enhanced light absorption due to the plasmonic scattering properties of metal nanoparticles. In fact, the light scattering cross–section of the particles increases with the size resulting in higher short–circuit current densities. Silver nanoparticle films exhibit photocurrent densities 46% higher than those exhibited by devices coated with sputtered indium tin oxide as transparent electrode.

In the last chapter, we have outlined the growth, fabrication and integration of III–V nanowires on silicon. Ordered arrays of vertical InAs nanowires were grown on a patterned SiO_2/Si substrate by means of molecular beam epitaxy. The growth of the nanowires has been demonstrated to be controlled by the diffusion of In adatoms on the oxide surface to the openings. The diffusion length and desorption rate of In on SiO_2 have been calculated to be approximately 240 nm and 0.12 Å/s, respectively, for a growth temperature of 500°C, a nominal In growth rate of 0.2 Å/s and As_4 partial pressure of 6×10^{-6} Torr. The diffusion length of In adatoms on the InAs nanowire sidewalls has also been determined when comparing arrays with different spacing between wires and growth times. A diffusion length between 1.1 and 5 μm has been obtained. The potential of the InAs/*p*–Si system for photovoltaic applications has been evaluated. Light absorption simulations determined that the light is mainly absorbed within the wires. However, the InAs/*p*–Si band alignment is not favourable to create a drift current from InAs to Si. In addition, we have presented evidence that when the light is absorbed in the silicon substrate it highly contributes to a better photoresponse due to a high conduction band offset that pushes electrons towards the junction. On the other hand, surface recombination at the substrate was shown to dramatically reduce the diffusion length of minority carriers: the diffusion length was found to increase from 18 to 123 μm when increasing the wavelength, and thus, generating the carriers further apart from the surface.

In conclusion, radial *p*–*n* junction nanowire arrays are good candidates for third generation solar cells. They exhibit a great potential in terms of light absorption and carrier collection, which can be strengthened through a good surface passivation and an optimum design. Moreover, they are interesting structures to use for materials with low diffusion lengths when configured in a radial manner. They also offer the possibility of combining different materials to create multijunction devices to match a broader range of the solar spectrum while using less material than for planar devices.

Bibliography

[1] BP statistical review of world energy. *http://www.bp.com/statisticalreview*, 2012.

[2] J. D. Hamilton. Causes and consequences of the oil shock of 2007–08. *Brookings Papers on Economic Activity*, 2009:215–261, 2009.

[3] J. Murray and D. King. Climate policy: Oil's tipping point has passed. *Nature*, 481:433–435, 2012.

[4] World energy outlook 2004. Technical report, International Energy Agency, 2004.

[5] M. Bazilian, I. Onyeji, M. Liebreich, I. MacGill, J. Chase, J. Shah, D. Gielen, D. Arent, D. Landfear, and S. Zhengrong. Re–considering the economics of photovoltaic power. *Renewable Energy*, 53:329–338, 2013.

[6] DuPont Innovalight. *http://www2.dupont.com/Photovoltaics/en_US/products_services/silicon_inks/silicon_inks.html*, 2001.

[7] Sol Voltaics. *http://www.solvoltaics.com*, 2008.

[8] M. Heurlin, M. H. Magnusson, D. Lindgren, M. Ek, L. R. Wallenberg, K. Deppert, and L. Samuelson. Continuous gas–phase synthesis of nanowires with tunable properties. *Nature*, 492:90–94, 2012.

[9] Jenny Nelson. *The Physics of Solar Cells.* Imperial College Press, 2003.

[10] M. A. Green, K. Emery, Y. Hishikawa, W. Warta, and E. D. Dunlop. Solar cell efficiency tables (version 41). *Progress in Photovoltaics: Research and Applications*, 21:1–11, 2013.

[11] A. Polman and H. A. Atwater. Photonic design principles for ultrahigh–efficiency photovoltaics. *Nature Materials*, 11:174–177, 2012.

[12] W. Shockley and H. J. Queisser. Detailed balance limit of efficiency of *p–n* junction solar cells. *J. Appl. Phys.*, 21:510, 1961.

[13] O. D. Miller, E. Yablonovitch, and S. R. Kurtz. Strong internal and external luminescence as solar cells approach the Shockley–Queisser limit. *IEEE Journal of Photovoltaics*, 2:303–311, 2012.

[14] M. A. Green. Third generation photovoltaics: Ultra–high conversion efficiency at low cost. *Progress in Photovoltaics: Research and Applications*, 9:123–135, 2001.

[15] A. Luque and A. Martí. Increasing the efficiency of ideal solar cells by photon induced transitions at intermediate levels. *Phys. Rev. Lett.*, 78:5014–5017, 1997.

[16] M. A. Green. Third generation photovoltaics: Solar cells for 2020 and beyond. *Physica E*, 14:65–70, 2002.

[17] P. Würfel. Solar energy conversion with hot electrons from impact ionisation. *Solar Energy Materials & Solar Cells*, 46:43–52, 1997.

[18] C. M. Lieber and Z. L. Wang. Functional nanowires. *MRS Bulletin*, 32:99–104, 2007.

[19] X. Duan, Y. Huang, Y. Cui, J. Wang, and C. M. Lieber. Indium phosphide nanowires as building blocks for nanoscale electronic and optoelectronic devices. *Nature*, 409:66–69, 2001.

[20] B. M. Kayes, H. A. Atwater, and N. S. Lewis. Comparison of the device physics principles of planar and radial *p*–*n* junction nanorod solar cells. *J. Appl. Phys.*, 97(11):114302, 2005.

[21] E. D. Kosten, E. L. Warren, and H. A. Atwater. Ray optical light trapping in silicon microwires: Exceeding the $2n^2$ intensity limit. *Optics Express*, 19:3316–3331, 2011.

[22] P. Krogstrup, H. I. Jørgensen, M. Heiß, O. Demichel, J. V. Holm, M. Aagesen, J. Nygard, and A. Fontcuberta i Morral. Single nanowire solar cells beyond the Shockley–Queisser limit. *Nature Photonics*, 7:306–310, 2013.

[23] R. R. LaPierre. Numerical model of current–voltage characteristics and efficiency of GaAs nanowire solar cells. *J. Appl. Phys.*, 109:034311, 2011.

[24] B. Tian, X. Zheng, T. J. Kempa, Y. Fang, N. Yu, G. Yu, J. Huang, and C. M. Lieber. Coaxial silicon nanowires as solar cells and nanoelectronic power sources. *Nature*, 449:885–889, 2007.

[25] B. Tian, T. J. Kempa, and C. M. Lieber. Single nanowire photovoltaics. *Chem. Soc. Rev.*, 38:16–24, 2009.

[26] L. Tsakalakos, J. Balch, J. Fronheiser, B. A. Korevaar, O. Sulima, and J. Rand. Silicon nanowire solar cells. *Appl. Phys. Lett.*, 91:233117, 2007.

[27] E. Garnett and P. Yang. Light trapping in silicon nanowire solar cells. *Nano Lett.*, 10:1082–1087, 2010.

[28] B. O'Donnell, L. Yu, M. Foldyna, and P. Roca i Cabarrocas. Silicon nanowire solar cells grown by PECVD. *Journal of Non–Crystalline Solids*, 358:2299–2302, 2011.

[29] D. R. Kim, C. H. Lee, P. M. Rao, I. S. Cho, and X. L. Zheng. Hybrid Si microwire and planar solar cells: passivation and characterization. *Nano Lett.*, 11:2704–2708, 2011.

[30] L. Yu, B. O'Donnell, M. Foldyna, and P. Roca i Cabarrocas. Radial junction amorphous silicon solar cells on PECVD–grown silicon nanowires. *Nanotechnology*, 23:194011, 2012.

[31] M. C. Putnam, D. B Turner-Evans, M. D. Kelzenberg, S. W. Boettcher, N. S. Lewis, and H. A. Atwater. 10 μm minority–carrier diffusion lengths in Si wires synthesized by Cu–catalyzed vapor–liquid–solid growth. *Appl. Phys. Lett.*, 95:163116, 2009.

[32] J. Wallentin, N. Anttu, D. Asoli, M. Huffman, I. Åberg, M. H. Magnusson, G. Siefer, P. Fuss-Kailuweit, F. Dimroth, B. Witzigmann, H. Q. Xu, L. Samuelson, K. Deppert, and M. T. Borgström. InP nanowire array solar cells achieving 13.8% efficiency by exceeding the ray optics limit. *Science*, 2013.

[33] J. Zhu, Z. Yu, G. F. Burkhard, C. M. Hsu, S. T. Connor, Y. Xu, Q. Wang, M. McGehee, S. Fan, and Y. Cui. Optical absorption enhancement in amorphous silicon nanowire and nanocone arrays. *Nano Lett.*, 9:279–282, 2009.

[34] J. Zhu, C-M Hsu, Z. Yu, S. Fan, and Y. Cui. Nanodome solar cells with efficient management and self–cleaning. *Nano Lett.*, 10:1979–1984, 2010.

[35] D. Zhou and R. Biswas. Photonic crystal enhanced light–trapping in thin film solar cells. *J. Appl. Phys.*, 103:093102, 2008.

[36] J. Motohisa and K. Hiruma. Light absorption in semiconductor nanowire arrays with multijunction cell structures. *Jpn. J. Appl. Phys.*, 51:11PE07, 2012.

[37] M. Foldyna, L. Yu, B. O'Donnell, and P. Roca i Cabarrocas. Optical absorption in vertical silicon nanowires for solar cell applications. In *Proc. SPIE*, 2011.

[38] A. Convertino, M. Cuscuna, S. Rubini, and F. Martelli. Optical reflectivity of GaAs nanowire arrays: Experiment and model. *J. Appl. Phys.*, 111:114302, 2012.

[39] C. Colombo, M. Heiß, M. Grätzel, and A. Fontcuberta i Morral. Gallium arsenide *p–i–n* radial structures for photovoltaic applications. *Appl. Phys. Lett.*, 94:173108, 2009.

[40] N. Tajik, Z. Peng, P. Kuyanov, and R. R. LaPierre. Sulfur passivation and contact methods for GaAs nanowire solar cells. *Nanotechnology*, 22:225402, 2011.

[41] H. Goto, K. Nosaki, K. Tomioka, S. Hara, K. Hiruma, J. Motohisa, and T. Fukui. Growth of core–shell InP nanowires for photovoltaic application by selective–area metal organic vapor phase epitaxy. *Appl. Phys. Express*, 2:035004, 2009.

[42] Y. Dong, B. Tian, T. J. Kempa, and C. M. Lieber. Coaxial group III–nitride nanowire photovoltaics. *Nano Lett.*, 9:2183–2187, 2009.

[43] W. U. Huynh, J. J. Dittmer, and A. P. Alivisatos. Hybrid nanorod–polymer solar cells. *Science*, 295:2425, 2002.

[44] Y. Kang, N. G. Park, and D. Kim. Hybrid solar cells with vertically aligned CdTe nanorods and a conjugated polymer. *Appl. Phys. Lett.*, 86:113101, 2005.

[45] J. B. Baxter and E. S. Aydil. Nanowire–based dye–sensitized solar cells. *Appl. Phys. Lett.*, 86:053114, 2005.

[46] M. Law, L. E. Greene, J. C. Johnson, R. Saykally, and P. Yang. Nanowire dye–sensitized solar cells. *Nature Materials*, 4:455–459, 2005.

[47] M. Y. Song, Y. R. Ahn, S. J. Jo, and D. Y. Kim. TiO_2 single–crystalline nanorod electrode for quasi–solid–state dye–sensitized solar cells. *Appl. Phys. Lett.*, 87:113113, 2005.

[48] K. E. Plass, M. A. Filler, J. M. Spurgeon, B. M. Kayes, S. Maldonado, B. S. Brunschwig, H. A. Atwater, and N. S. Lewis. Flexible polymer–embedded Si wire arrays. *Adv. Mater.*, 21:325–328, 2009.

[49] Y. Da and Y. Xuan. Role of surface recombination in affecting the efficiency of nanostructured thin–film solar cells. *Optics Express*, 21:A1065–A1077, 2013.

[50] S. Yu, F. Roemer, and B. Witzigmann. Analysis of surface recombination in nanowire array solar cells. *Journal of Photonics for Energy*, 2:028002, 2012.

[51] W. C. Johnson and P. T. Panousis. The influence of Debye length on C–V measurement of doping profile. *IEEE Trans.*, ED-18:965–973, 1971.

[52] S. W. Jones. Diffusion in Silicon. IC Knowledge LLC, April 2008.

[53] G. W. Neudeck. *The pn junction diode.* Addison–Wesley Publishing Company, 1989.

[54] M. A. Green and M. J. Keevers. Optical properties of intrinsic silicon at 300 K. *Progress in Photovoltaics: Research and Applications*, 3:189–192, 1995.

[55] R. Calarco, M. Marso, T. Richter, A. I. Aykanat, R. Meijers, A. v. d. Hart, T. Stoica, and H. Lüth. Size–dependent photoconductivity in MBE–grown GaN–nanowires. *Nano Lett.*, 5(5):981–984, 2005.

[56] O. Demichel, M. Heiß, J. Bleuse, H. Mariette, and A. Fontcuberta i Morral. Impact of surfaces on the optical properties of GaAs nanowires. *Appl. Phys. Lett.*, 97:201907, 2010.

[57] D. Macdonald and A. Cuevas. Reduced fill factors in multicrystalline silicon solar cells due to injection–level dependent bulk recombination lifetimes. *Prog. Photovolt: Res. Appl.*, 8:363–375, 2000.

[58] J. del Alamo, S. Swirhun, and R. M. Swanson. Measuring and modeling minority carrier transport in heavily doped silicon. *Solid–State Electronics*, 28:47–54, 1985.

[59] G. Dingemans and W. M. M. Kessels. Status and prospects of Al_2O_3–based surface passivation schemes for silicon solar cells. *J. Vac. Sci. Technol. A*, 30:040802, 2012.

[60] A. G. Aberle, S. Glunz, and W. Warta. Field effect passivation of high efficiency silicon solar cells. *Solar Energy Materials & Solar Cells*, 29:175–182, 1993.

[61] M. V. Fernández-Serra, Ch. Adessi, and X. Blase. Conductance, surface traps, and passivation in doped silicon nanowires. *Nano Lett.*, 6:2674–2678, 2006.

[62] Y. Dan, K. Seo, K. Takei, J. H. Meza, A. Javey, and K. B. Crozier. Dramatic reduction of surface recombination by in situ surface passivation of silicon nanowires. *Nano Lett.*, 11:2527–2532, 2011.

[63] J. E. Allen, E. R. Hemesath, D. E. Perea, J. L. Lensch-Falk, Z. Y. Li, F. Yin, M. H. Gass, P. Wang, A. L. Bleloch, R. E. Palmer, and L. J. Lauhon. High–resolution detection of Au catalyst atoms in Si nanowires. *Nature Technology*, 3:168–173, 2008.

[64] Y. Cui, J. Wang, S. R. Plissard, A. Cavalli, T. T. T. Vu, R. P. J. van Veldhoven, L. Gao, M. Trainor, M. A. Verheijen, J. E. M. Haverkort, and E. P. A. M. Bakkers. Efficiency enhancement of InP nanowire solar cells by surface cleaning. *Nano Lett.*, 13:4113–4117, 2013.

[65] B. Hoex, F. J. J. Peeters M. Creatore, M. A. Blauw, W. M. M. Kessels, and M. C. M. van de Sanden. High–rate plasma–deposited SiO_2 films for surface passivation of crystalline silicon. *J. Vac. Sci. Technol. A*, 24:1823–1830, 2006.

[66] S. De Wolf, G. Agostinelli, G. Beaucarne, and P. Vitanov. Influence of stoichiometry of direct plasma–enhanced chemical vapor deposited SiN_x films and silicon substrate surface roughness on surface passivation. *J. Appl. Phys.*, 97:063303, 2005.

[67] B. Hoex, J. J. H. Gielis, M. C. M. van de Sanden, and W. M. M. Kessels. On the c–Si surface passivation mechanism by the negative–charge–dielectric Al_2O_3. *J. Appl. Phys.*, 104:113703, 2008.

[68] V. R. Manfrinato, L. Zhang, D. Su, H. Duan, R. G. Hobbs, E. A. Stach, and K. K. Berggren. Resolution limits of electron–beam lithography toward the atomic scale. *Nano Lett.*, 13:1555–1558, 2013.

[69] C. L. Haynes and R. P. Van Duyne. Nanosphere lithography: A versatile nanofabrication tool for studies of size–dependent nanoparticle optics. *J. Phys. Chem.*, 105:5599–5611, 2001.

[70] C. S. Lim, M. H. Hong, Y. Lin, Q. Xie, B. S. Luk'yanchuk, A. Senthil Kumar, and M. Rahman. Microlens array fabrication by laser interference lithography for super–resolution surface nanopatterning. *Appl. Phys. Lett.*, 89:191125, 2006.

[71] H. Morimoto, Y. Sasaki, K. Saitoh, Y. Watakabe, and T. Kato. Focused ion beam lithography and its application to submicron devices. *Microelectronic Engineering*, 4:163–179, 1986.

[72] H. J. Fan, P. Werner, and M. Zacharias. Semiconductor nanowires: From self–organization to patterned growth. *Small*, 2:700–717, 2006.

[73] F. Güder, Y. Yang, M. Krüger, G. B. Stevens, and M. Zacharias. Atomic layer deposition on phase–shift lithography generated photoresist patterns for 1D nanochannel fabrication. *ACS Appl. Mater. Interfaces*, 2:3473–3478, 2010.

[74] K. Subannajui, F. Güder, and M. Zacharias. Bringing order to the world of nanowire devices by phase shift lithography. *Nano Lett.*, 11:3513–3518, 2011.

[75] S. H. Chan, A. K. Wong, and E. Y. Lam. Initialization for robust inverse synthesis of phase–shifting masks in optical projection lithography. *Optics Express*, 16:14746–14760, 2008.

[76] T. Ito and S. Okazaki. Pushing the limits of lithography. *Nature*, 406:1027–1031, 2000.

[77] M. D. Levenson, N. S. Viswanathan, and R. A. Simpson. Improving resolution in photolithography with a phase–shifting mask. *IEEE Transactions on Electron Devices*, ED–29:1828–1836, 1982.

[78] F. Wang, K. E. Weaver, A. Lakhtakia, and M. W. Horn. Electromagnetic modeling of near–field phase–shifting contact lithography with broadband ultraviolet illumination. *Optik*, 116:1–9, 2005.

[79] J. A. Rogers, K. E. Paul, R. J. Jackman, and G. M. Whitesides. Using an elastomeric phase mask for sub–100 nm photolithography in the optical near field. *Appl. Phys. Lett.*, 70:2658–2660, 1997.

[80] R. Salach-Bielecki, T. Pisarkiewicz, T. Stapiński, and P. Wójcik. Influence of junction parameters on the open circuit voltage decay in solar cells. *Opto–Electron. Rev.*, 12(1):79–83, 2004.

[81] R. A. Sinton and A. Cuevas. Contactless determination of current–voltage characteristics and minority carrier lifetimes in semiconductors from quasisteadystate photoconductance data. *Appl. Phys. Lett.*, 69:2510–2512, 1996.

[82] M. J. Kerr, A. Cuevas, and R. A. Sinton. Generalized analysis of quasi–steady–state and transient decay open circuit voltage measurements. *J. Appl. Phys.*, 91(1):399–404, 2002.

[83] *http://pveducation.org/pvcdrom/materials/general-properties-of-silicon.*

[84] H. Mäckel and R. Lüdemann. Detailed study of the composition of hydrogenated SiN_x layers for high–quality silicon surface passivation. *J. Appl. Phys.*, 92:2602–2609, 2002.

[85] M. L. Reed and J. D. Plummer. Chemistry of Si–SiO_2 interface trap annealing. *J. Appl. Phys.*, 63:5776–5793, 1988.

[86] G. Dingemans, M. M. Mandoc, S. Bordihn, M. C. M. van de Sanden, and W. M. M. Kessels. Effective passivation of Si surfaces by plasma deposited SiO_x/a–SiN_x:H stacks. *Appl. Phys. Lett.*, 98:222102, 2011.

[87] D. B. Mawhinney, J. A. Glass Jr., and J. T. Yates Jr. FTIR study of the oxidation of porous silicon. *J. Phys. Chem. B*, 101:1202–1206, 1997.

[88] K. Matsunaga, T. Tanaka, T. Yamamoto, and Y. Ikuhara. First–principles calculations of intrinsic defects in Al_2O_3. *Phys. Rev. B*, 68:085110, 2003.

[89] software package next**nano**^{3}. *http://www.nextnano.com/nextnano3/index.htm.*

[90] A. F. Oskooi, D. Roundy, M. Ibanescu, P. Bermel, J. D. Joannopoulos, and S. G. Johnson. MEEP: A flexible free–software package for electromagnetic simulations by the FDTD method. *Comput. Phys. Commun.*, 181:687–702, 2010.

[91] M. F. Stuckings and A. W. Blakers. A study of shading and resistive loss from the fingers of encapsulated solar cells. *Solar Energy Materials & Solar Cells*, 59:233–242, 1999.

[92] Y. Takahashi, S. Okada, R. B. H. Tahar, K. Nakano, T. Ban, and Y. Ohya. Dip–coating of ITO films. *Journal of Non–Crystalline Solids*, 218:129–134, 1997.

[93] M. Toki and M. Aizawa. Sol–gel formation of ITO thin film from a sol including ITO powder. *Journal of Sol–Gel Science and Technology*, 8:717–720, 1997.

[94] P. Thilakan, S. Kalainathan, J. Kumar, and P. Ramasamy. Deposition and characterization of indium oxide and indium tin oxide semiconducting thin films by reactive thermal deposition technique. *Journal of Electronic Materials*, 24:719–724, 1995.

[95] T. Maruyama and K. Fukui. Indium tin oxide thin films prepared by chemical vapour deposition. *Thin Solid Films*, 203:297–302, 1991.

[96] J. George and C. S. Menon. Electrical and optical properties of electron beam evaporated ITO thin films. *Surface and Coatings Technology*, 132:45–48, 2000.

[97] Y. Zhou, G. M. Wu, D. W. Gao, G. J. Xing, Y. Y. Zhu, Z. Q. Zhang, and Y. Cao. Preparation and physical properties of ITO thin films by spray pyrolysis method. *Advanced Materials Research*, 465:268–275, 2012.

[98] C. Calì, M. Mosca, and G. Targia. Deposition of indium tin oxide films by laser ablation: Processing and characterization. *Solid–State Electronics*, 42(5):877–879, 1998.

[99] J. W. Elam, D. A. Baker, A. B. F. Martinson, M. J. Pellin, and J. T. Hupp. Atomic layer deposition of indium tin oxide thin films using nonhalogenated precursors. *J. Phys. Chem. C*, 112:1938–1945, 2008.

[100] K. Utsumi, O. Matsunaga, and T. Takahata. Low resistivity ITO film prepared using the ultra high density ITO target. *Thin Solid Films*, 334:30–34, 1998.

[101] P. L. McEuen, M. S. Fuhrer, and H. Park. Single–walled carbon nanotube electronics. *IEEE Transaction on Nanotechnology*, 1(1):78–85, 2002.

[102] S. J. Kang, C. Kocabas, T. Ozel, M. Shim, N. Pimparkar, M. A. Alam, S. V. Rotkin, and J. A. Rogers. High–performance electronics using dense, perfectly aligned arrays of single–walled carbon nanotubes. *Nature Nanotechnology*, 2:230–236, 2007.

[103] Z. Wu, Z. Chen, X. Du, J. M. Logan, J. Sippel, M. Nikolou, K. Kamaras, J. R. Reynolds, D. B. Tanner, A. R. Hebard, and A. G. Rinzler. Transparent, conductive carbon nanotube films. *Science*, 305:1273–1276, 2004.

[104] A. Du Pasquier, H. E. Unalan, A. Kanwal, S. Miller, and M. Chhowalla. Conducting and transparent single–wall carbon nanotube electrodes for polymer–fullerene solar cells. *Appl. Phys. Lett.*, 87:203511, 2005.

[105] M. W. Rowell, M. A. Topinka, M. D. McGehee, H. J. Prall, G. Denner, N. S. Sariciftci, L. Hu, and G. Gruner. Organic solar cells with carbon nanotube network electrodes. *Appl. Phys. Lett.*, 88:233506, 2006.

[106] J. Van de Lagemaat, T. M. Barnes, G. Rumbles, S. E. Shaheen, T. J. Coutts, C. Weeks, I. Levitsky, J. Peltola, and P. Glatkowski. Organic solar cells with carbon nanotubes replacing In_2O_3:Sn as the transparent electrode. *Appl. Phys. Lett.*, 88:233503, 2006.

[107] K. S. Novoselov, A. K. Geim, S. V. Morozov, D. Jiang, Y. Zhang, S. V. Dubonos, I. V. Grigorieva, and A. A. Firsov. Electric field effect in atomically thin carbon films. *Science*, 306:666–669, 2004.

[108] A. K. Geim. Graphene: Status and prospects. *Science*, 324:1530–1534, 2009.

[109] H. Park, J. A. Rowehl, K. K. Kim, V. Bulovic, and J. Kong. Doped graphene electrodes for organic solar cells. *Nanotechnology*, 21:505204, 2010.

[110] D. S. Hecht, L. Hu, and G. Irvin. Emerging transparent electrodes based on thin films of carbon nanotubes, graphene, and metallic nanostructures. *Adv. Mater.*, 23(13):1482–1513, 2011.

[111] G. P. Kushto, W. Kim, and Z. H. Kafafi. Flexible organic photovoltaics using conducting polymer electrodes. *Appl. Phys. Lett.*, 86:093502, 2005.

[112] S. Admassie, F. Zhang, A. G. Manoj, M. Svensson, M. R. Andersson, and O. Inganäs. A polymer photodiode using vapour–phase polymerized PEDOT as an anode. *Solar Energy Materials & Solar Cells*, 90:133–141, 2006.

[113] Y. Zhou, F. Zhang, K. Tvingstedt, S. Barrau, F. Li, W. Tian, and O. Inganäs. Investigation on polymer anode design for flexible polymer solar cells. *Appl. Phys. Lett.*, 92:233308, 2008.

[114] L. Hu, H. Wu, and Y. Cui. Metal nanogrids, nanowires, and nanofibers for transparent electrodes. *MRS Bulletin*, 36:760–765, 2011.

[115] S. De, T. Higgins, P. E. Lyons, E. M. Doherty, P. N. Nirmalraj, W. J. Blau, J. J. Boland, and J. N. Coleman. Silver nanowire networks as flexible, transparent, conducting films: Extremely high DC to optical conductivity ratios. *ACS Nano*, 3:1767–1774, 2009.

[116] J. Lee, S. T. Connor, Y. Cui, and P. Peumans. Solution–processed metal nanowire mesh transparent electrodes. *Nano Lett.*, 8:689–692, 2008.

[117] Y. Chang, M. L. Lye, and H. C. Zeng. Large–scale synthesis of high–quality ultralong copper nanowires. *Langmuir*, 21:3746–3748, 2005.

[118] A. R. Rathmell, S. M. Bergin, Y. L. Hua, Z. Y. Li, and B. J. Wiley. The growth mechanism of copper nanowires and their properties in flexible, transparent conducting films. *Adv. Mater.*, 22:3558–3563, 2010.

[119] P. C. Hsu, H. Wu, T. J. Carney, M. T. McDowell, Y. Yang, E. C. Garnett, M. Li, L. Hu, and Y. Cui. Passivation coating on electrospun copper nanofibers for stable transparent electrodes. *ACS Nano*, 6(6):5150–5156, 2012.

[120] B. O'Connor, C. Haughn, K. H. An, K. P. Pipe, and M. Shtein. Transparent and conductive electrodes based on unpatterned, thin metal films. *Appl. Phys. Lett.*, 93:223304, 2008.

[121] R. Barbey, L. Lavanant, D. Paripovic, N. Schüwer, C. Sugnaux, S. Tugulu, and H. A. Klok. Polymer brushes via surface–initiated controlled radical polymerization: Synthesis, characterization, properties, and applications. *Chemical Reviews*, 109:5437–5527, 2009.

[122] D.J. Kim, K. B Lee, Y. S. Chi, W. J. Kim, H. J. Paik, and I. S. Choi. Biomimetic formation of silica thin films by surface–initiated polymerization of 2–(dimethylamino)ethyl methacrylate and silicic acid. *Langmuir*, 20:7904–7906, 2004.

[123] D. J. Kim, K. B Lee, T. G. Lee, H. K. Shon, W. J. Kim, H. J. Paik, and I. S. Choi. Biomimetic micropatterning of silica by surface–initiated polymerization and microcontact printing. *Small*, 1:992–996, 2005.

[124] S. H. Yang, K. Kang, and I. S. Cho. Biomimetic approach to the formation of titanium dioxide thin films by using poly(2–(dimethylamino)ethyl methacrylate). *Chem. Asian J.*, 3:2097–2104, 2008.

[125] S. Tugulu, M. Harms, M. Fricke, D. Volkmer, and H. A. Klok. Polymer brushes as ionotropic matrices for the directed fabrication of microstructured calcite thin films. *Angew. Chem. Int. Ed.*, 45:7458–7461, 2006.

[126] D. Paripovic and H. A. Klok. Polymer brush guided formation of thin gold and palladium/gold bimetallic films. *ACS Appl. Mater. Interfaces*, 3:910–917, 2011.

[127] K. R. Catchpole and A. Polman. Design principles for particle plasmon enhanced solar cells. *Appl. Phys. Lett.*, 93:191113, 2008.

[128] M. J. Mendes, I. Tobías, A. Martí, and A. Luque. Light concentration in the near–field of dielectric spheroidal particles with mesoscopic sizes. *Optics Express*, 19:16207–16222, 2011.

[129] H. A. Atwater and A. Polman. Plasmonics for improved photovoltaic devices. *Nature Materials*, 9:205–213, 2010.

[130] S. Mokkapati, F. J. Beck, A. Polman, and K. R. Catchpole. Designing periodic arrays of metal nanoparticles for light–trapping applications in solar cells. *Appl. Phys. Lett.*, 95:053115, 2009.

[131] K. Nakayama, K. Tanabe, and H. A. Atwater. Plasmonic nanoparticle enhanced light absorption in GaAs solar cells. *Appl. Phys. Lett.*, 93:121904, 2008.

[132] P. Pavaskar, I. K. Hsu, J. Theiss, W. H. Hung, and S. B. Cronin. A microscopic study of strongly plasmonic Au and Ag island thin films. *J. Appl. Phys.*, 113:034302, 2013.

[133] S. Pillai, K. R. Catchpole, T. Trupke, and M. A. Green. Surface plasmon enhanced silicon solar cells. *J. Appl. Phys.*, 101:093105, 2007.

[134] D. M. Schaadt, B. Feng, and E. T. Yu. Enhanced semiconductor optical absorption via surface plasmon excitation in metal nanoparticles. *Appl. Phys. Lett.*, 86:063106, 2005.

[135] C. F. Bohren and D. R. Huffman. *Absorption and Scattering of Light by Small Particles.* Wiley-VCH Verlag GmbH, 1983.

[136] X. Wang, R. E. Ruther, J. A. Streifer, and R. J. Hamers. UV–induced grafting of alkenes to silicon surfaces: Photoemission versus excitons. *J. Am. Chem. Soc.*, 132:4048–4049, 2010.

[137] D. Xu, W. H. Yu, E. T. Kang, and K. G. Neoh. Functionalization of hydrogen–terminated silicon via surface–initiated atom–transfer radical polymerization and derivatization of the polymer brushes. *Journal of Colloid and Interface Science*, 279:78–87, 2004.

[138] E. M. Benetti, X. F. Sui, Zapotoczny S., and G. J. Vancso. Surface–grafted gel–brush/metal nanoparticle hybrids. *Adv. Funct. Mater.*, 20:939–944, 2010.

[139] C. Sugnaux, L. Lavanant, and H. A. Klok. Aqueous fabrication of pH–gated, polymer–brush–modified alumina hybrid membranes. *Langmuir*, 29:7325–7333, 2013.

[140] G. Kästle, H. G. Boyen, Weigl F., Lengl G., Herzog T., Ziemann P., S. Riethmüller, O. Mayer, C. Hartmann, J. P. Spatz, M. Möller, M. Ozawa, F. Banhart, M. G. Garnier, and P. Oelhafen. Micellar nanoreactors–preparation and characterization of hexagonally ordered arrays of metallic nanodots. *Adv. Funct. Mater.*, 13:853–861, 2003.

[141] G. Beamson and D. Briggs. *High resolution XPS of organic polymers, the scienta ESCA300 database.* 1992.

[142] A. M. Ferraria, A. P. Carapeto, and A. M. Botelho do Rego. X–ray photoelectron spectroscopy: Silver salts revisited. *Vacuum*, 86:1988–1991, 2012.

[143] D. Dasgupta, I. K. Shishmanova, A. Ruiz-Carretero, K. Lu, M. Verhoeven, H. P. C. van Kuringen, G. Portale, P. Leclère, C. W. M. Bastiaansen, D. J. Broer, and A. P. H. J. Schenning. Patterned silver nanoparticles embedded in a nanoporous smectic liquid crystalline polymer network. *J. Am. Chem. Soc.*, 135:10922–10925, 2013.

[144] A. Henglein and M. Giersig. Formation of colloidal silver nanoparticles: Capping action of citrate. *J. Phys. Chem. B*, 103:9533–9539, 1999.

[145] C. Petit, P. Lixon, and M. P. Pileni. In situ synthesis of silver nanocluster in AOT reverse micelles. *J. Phys. Chem.*, 97:12974–12983, 1993.

[146] K. R. Catchpole and A. Polman. Plasmonic solar cells. *Optics Express*, 16:21793–21800, 2008.

[147] B. P. Rand, P. Peumans, and S. R. Forrest. Long–range absorption enhancement in organic tandem thin–film solar cells containing silver nanoclusters. *J. Appl. Phys.*, 96:7519–7526, 2004.

[148] F. J. Beck, E. Verhagen, S. Mokkapati, A. Polman, and K. R. Catchpole. Resonant SPP modes supported by discrete metal nanoparticles on high–index substrates. *Optics Express*, 19:A146–A156, 2011.

[149] M. Brongersma and P. G. Kik. *Surface Plasmon Nanophotonics.* Springer Series in Optical Sciences, 2007.

[150] P. Spinelli, V. E. Ferry, J. van de Groep, M. van Lare, M. A. Verschuuren, R. E. I. Schropp, H. A. Atwater, and A. Polman. Plasmonic light trapping in thin–film Si solar cells. *J. Opt.*, 14:024002, 2002.

[151] P. F. Liao and A. Wokaun. Lightning rod effect in surface enhanced Raman scattering. *J. Chem. Phys.*, 76:751–752, 1982.

[152] M. Heiss, E. Russo-Averchi, A. Dalmau-Mallorquí, G. Tutuncuoglu, F. Matteini, D. Rüffer, S. Conesa-Boj, O. Demichel, E. Alarcon-Lladó, and A. Fontcuberta i Morral. III–V nanowire arrays: Growth and light interaction. *Nanotechnology*, 2013.

[153] S. Plissard, K. A. Dick, G. Larrieu, S. Godey, A. Addad, X. Wallart, and P. Caroff. Gold–free growth of GaAs nanowires on silicon: Arrays and polytypism. *Nanotechnology*, 21:385602, 2010.

[154] S. Plissard, G. Larrieu, X. Wallart, and P. Caroff. High yield of self–catalyzed GaAs nanowire arrays grown on silicon via gallium droplet positioning. *Nanotechnology*, 22:275602–275608, 2011.

[155] The Shockley–Queisser limit. *http://sjbyrnes.com/sq.html.*

[156] T. Mårtensson. *Semiconductor Nanowires: Epitaxy and Applications.* PhD thesis, Lund University, 2008.

[157] C. D. Bessire, M. T. Björk, H. Schmid, A. Schenk, K. B. Reuter, and H. Riel. Trap–assisted tunneling in Si–InAs nanowire heterjunction tunnel diodes. *Nano Lett.*, 11:4195–4199, 2011.

[158] E. P. A. M. Bakkers, J. A. van Dam, S. De Franceschi, L. P. Kouwenhoven, M. Kaiser, M. Verheijen, H. Wondergem, and P. van der Sluis. Epitaxial growth of InP nanowires on germanium. *Nature Materials,* 3:769–773, 2004.

[159] J. Johansson, L. S. Karlsson, C. P. T. Svensson, T. Mårtensson, B. A. Wacaser, K. Deppert, L. Samuelson, and W. Seifert. Structural properties of <111>B –oriented III–V nanowires. *Nature Materials*, 5:574–580, 2006.

[160] M. T. Björk, H. Schmid, C. M. Breslin, L. Gignac, and H. Riel. InAs nanowire growth on oxide–masked <111> silicon. *Journal of Crystal Growth*, 344:31–37, 2012.

[161] S. Hertenberger, D. Rudolph, M. Bichler, J. J. Finley, G. Abstreiter, and G. Koblmüller. Growth kinetics in position–controlled and catalyst–free InAs nanowire arrays on Si(111) grown by selective area molecular beam epitaxy. *J. Appl. Phys.*, 108:114316, 2010.

[162] K. Tomioka, P. Mohan, J. Noborisaka, S. Hara, J. Motohisa, and T. Fukui. Growth of highly uniform InAs nanowire arrays by selective–area MOVPE. *Journal of Crystal Growth*, 298(17):644–647, 2007.

[163] T. Mårtensson, P. Carlberg, M. Borgström, L. Montelius W. Seifert, and L. Samuelson. Nanowire arrays defined by nanoimprint lithography. *Nano Lett.*, 4:699–702, 2004.

[164] B. Furhmann, H. S. Leipner, H. R. Höche, L. Schubert, P. Werner, and U. Gösele. Ordered arrays of silicon nanowires produced by nanosphere lithography and molecular beam epitaxy. *Nano Lett.*, 5(12):2524–2527, 2005.

[165] Z. H. Wu, X. Y. Mei, D. Kim, M. Blumin, and H. E. Ruda. Growth of Au–catalyzed ordered GaAs nanowire arrays by molecular–beam epitaxy. *Appl. Phys. Lett.*, 81(27):5177–5179, 2002.

[166] R. S. Wagner and W. C. Ellis. Vapor–liquid–solid mechanism of single crystal growth. *Appl. Phys. Lett.*, 4(5):89, 1964.

[167] E. I. Givargizov. Fundamental aspects of VLS growth. *Journal of Crystal Growth*, 31:20–30, 1975.

[168] K. Hiruma, M. Yazawa, T. Katsuyama, K. Ogawa, K. Haraguchi, M. Koguchi, and H. Kakibayashi. Growth and optical properties of nanometer–scale GaAs and InAs whiskers. *J. Appl. Phys.*, 77:447, 1995.

[169] F. Martelli, S. Rubini, F. Jabeen, L. Felisari, and V. Grillo. On the growth of InAs nanowires by molecular beam epitaxy. *Journal of Crystal Growth*, 323:297–300, 2011.

[170] A. I. Persson, M. W. Larsson, S. Stenström, B. J. Ohlsson, L. Samuelson, and L. R. Wallenberg. Solid–phase diffusion mechanism for GaAs nanowire growth. *Nature Materials*, 3:677–681, 2004.

[171] V. Schmidt, J. V. Wittemann, S. Senz, and U. Gösele. Silicon nanowires: A review on aspects of their growth and their electrical properties. *Adv. Mater.*, 21:2681–2702, 2009.

[172] B. Bauer, A. Rudolph, M. Soda, A. Fontcuberta i Morral, J. Zweck, D. Schuh, and E. Reiger. Position–controlled self–catalyzed growth of GaAs nanowires by molecular beam epitaxy. *Nanotechnology*, 21:435601, 2010.

[173] C. Colombo, D. Spirkoska, D. Frimmer, G. Abstreiter, and A. Fontcuberta i Morral. Ga–assisted catalyst–free growth mechanism of GaAs nanowires by molecular beam epitaxy. *Phys. Rev. B*, 77:155326, 2008.

[174] B. Mandl, J. Stangl, E. Hilner, A. A. Zakharov, K. Hillerich, A. W. Dey, L. Samuelson, G. Bauer, K. Deppert, and A. Mikkelsen. Growth mechanism of self–catalyzed group III–V nanowires. *Nano Lett.*, 10:4443–4449, 2010.

[175] B. Mandl, A. W. Dey, J. Stangl, M. Cantoro, L. E. Wernersson, G. Bauer, L. Samuelson, K. Deppert, and C. Thelander. Self–seeded, position–controlled InAs nanowire growth on Si: A growth parameter study. *Journal of Crystal Growth*, 334:51–56, 2011.

[176] S. Hertenberger, D. Rudolph, S. Bolte, M. Döblinger, M. Bichler, D. Spirkoska, J. J. Finley, G. Abstreiter, and G. Koblmüller. Absence of vapor–liquid–solid growth during molecular beam epitaxy of self–induced InAs nanowires on Si. *Appl. Phys. Lett.*, 98:123114, 2011.

[177] R. Q. Zhang, Y. Lifshitz, and S. T. Lee. Oxide–assisted growth of semiconducting nanowires. *Adv. Mater.*, 15(7–8):635–640, 2003.

[178] M. Heiß, E. Riedlberger, D. Spirkoska, M. Bichler, G. Abstreiter, and A. Fontcuberta i Morral. Growth mechanisms and optical properties of GaAs–based semiconductor microstructures by selective area epitaxy. *Journal of Crystal Growth*, 310:1049–1056, 2008.

[179] K. Ikejiri, J. Noborisaka, S. Hara, J. Motohisa, and T. Fukui. Mechanism of catalyst–free growth of GaAs nanowires by selective area MOVPE. *Journal of Crystal Growth*, 298:616–619, 2007.

[180] L. Fröberg. *Growth, Physics, and Device Applications of InAs–based nanowires*. PhD thesis, Lund University, 2008.

[181] K. Schulten. Einstein diffusion equation. http://www.ks.uiuc.edu/Services/Class/PHYS498/, 1999.

[182] N. V. Sibirev, M. Tchernycheva, M. A. Timofeeva, J. C. Harmand, G. E. Cirlin, and V. G. Dubrovskii. Influence of shadow effect on the growth and shape of InAs nanowires. *J. Appl. Phys.*, 111:104317, 2012.

[183] M. Tchernycheva, L. Travers, G. Patriarche, F. Glas, J. C. Harmand, G. E. Cirlin, and V. G. Dubrovskii. Au–assisted molecular beam epitaxy of InAs nanowires: Growth and theoretical analysis. *J. Appl. Phys.*, 102:094313, 2007.

[184] E. Halpern, G. Elias, A. V. Kretinin, H. Shtrikman, and Y. Rosenwaks. Direct measurement of surface states density and energy distribution in individual InAs nanowires. *Appl. Phys. Lett.*, 100:262105, 2012.

[185] K. A. Dick, J. Bolinsson, M. E. Messing, S. Lehmann, J. Johansson, and P. Caroff. Parameter space mapping of InAs nanowire crystal structure. *J. Vac. Sci. Technol. B*, 29:04D103, 2011.

[186] M. Z. Rahman. Modeling minority carrier's recombination lifetime of p–Si solar cell. *International Journal of Renewable Energy Research*, 2:117–122, 2012.

Acknowledgements

This adventure, which is about to finish, began on 24 February 2009. That day I received a short but concise email from Anna opening for me the doors of LMSC:

> "Estimada Anna
>
> t'escric perque he vist la teva candidatura per fer la tesi a Lausanne. Podriem parlar per telefon sobre la possibilitat de venir al meu laboratori?
>
> Cordialment,
>
> Anna" [*sic*]

Trusting someone who comes from a completely different field is not easy, but she did it. And not only this, she also opened her home to make my landing in Lausanne easier. Per tot això i el que ha vingut després, moltíssimes gràcies.

But before even arriving to Lausanne, I already had my '*personal assistant*' via email: Yvonne. She was the person who guided me through all the administrative steps and who I knew I could rely on for any kind of trouble. Merci Yvonne pour être toujours prête à m'aider et pour ta gentillesse.

And of course, a good story needs a happy beginning. And I had the perfect colleagues for that: Carlo, who introduced me in the photovoltaic and clean room world; Bernt, who forced me to learn how to deal with physicists; and Santi, who was always able to bring good humour and friendliness. Thank you guys for the nice environment, memorable evenings in Satellite and Café du Pont and the many trips and excursions we enjoyed together.

Starting from the very first day in LMSC, I was immersed in a (new to me so far) *clean–room experience*. I will not forget the exciting time I spent (sometimes being more successful than many others) in clean–room: first in Physics Department and later on at CMI. All the processing I carried out was, definitely, thanks to Nicolas Leiser, Damien and Yoan Trolliet from ICMP, and Cyrille Hibert, Jean–Baptiste Bureau, Kevin Lister, Georges–André Racine and Zdenek Benes among many other technicians from CMI. Many thanks to all of them for taking care of the clean–room facilities and being available to bring new ideas and suggestions to improve the process flow.

After the first year the group started to grow and the intimate and cosy LMSC atmosphere changed with the arrival of old acquaintances from Munich: Lele, our nanowire grower, and Martin, a well of wisdom; and new blood: Stefano, Marco, Michael, Pierre, Shanna, Ele, Olivier, Yuyang, Lajko, … All them integrated and adapted in the group, making the lab an enjoyable place to be. And this have not change over the years, including the latest incorporations: Francesca, living often at the edge of a nervous breakdown; Jelena, who has always a moment to chat with friends while enjoying a glass of wine; and Heidi, always up for any kind of event.

Winters would not have been that fun without Fede, Chiara, Albertino and Daniel, always ready for skiing or playing board games.

Of course, a Catalan professor needs to form a Catalan cluster: gràcies Sònia per ser–hi, tant en la benvinguda com en l'‘a reveure’; Esther, per no tenir mai un no com a resposta; i Ignasi, per fer–me recordar els vells temps a l'ETSEIB.

During these more than 4 years, many students spent some time at LMSC carrying out their semester/master projects: Diane, Brigitte, Daniel, Jane, Armand, Vincent, Amirreza, Ignasi, Jérémie and Alice. They brought enthusiasm and helped me with my projects; I learned from them and I hope they also learned something from me.

I have also learned that sometimes collaborations can be fruitful both at the professional level as well as at the personal level. Merci Caro pour le bon travail, pour ne jamais perdre la confiance en notre projet et le courage mutuel dans ce période de stress. Je te souhaite le meilleur pour la fin de ta thèse et la suite aux États-Unis.

My last year would have been *fucking* boring without my beloved Tutu and Gelato. Thank you girls for the nice moments we shared together, for your friendship and for being there. I wish you good luck for your future endeavors.

It took me a while (as usual in Lausanne), but I finally found a place where I felt at home. Merci JD et Lara d'abord, et Florie plus tard, pour la bonne ambiance dans l'appart, les ‘cours de français’ et les week–ends au chalet.

I am grateful to Prof. Andreas Mortensen, Prof. Pere Roca i Cabarrocas, Prof. Fabien Sorin and Prof. Joan Ramon Morante i Lleonart to have kindly accepted to be part of my defense committee.

Naturalment, durant tot aquest temps sempre he tingut un ull posat a Catalunya i als meus. Les visites, les vacances en bici, el ‘*Dalmau style*’ o un simple email m'han fet sentir més a prop de la meva terra. Gràcies.

Finalment, la meva més sincera gratitud als meus pares i la meva germana per ensenyar–me a ser qui sóc i per ajudar–me a arribar fins aquí. Vull agrair en especial a la meva mare i a la meva germana la fortalesa que m'han demostrat i transmès en uns moments tan difícils com els que ens ha tocat viure. També vull donar les gràcies als meus oncles pel seu suport durant aquests últims anys.

Lausanne, November 2013 Anna Dalmau i Mallorquí

Anna Dalmau Mallorquí

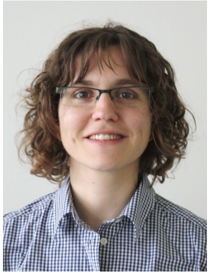

Date of birth: 16.11.1982
Ave. Louis Ruchonnet, 31 • 1003 Lausanne • Switzerland
✉ dalmaua@gmail.com ☎ +41 (0) 76 216 99 51

Education

2009–Present **École Polytechnique Fédérale de Lausanne, EPFL** Lausanne, Switzerland
PhD in Materials Science.
Nanowire–Based Solar Cells: Device Design and Implementation.

2000–2006 **Technical University of Catalonia, ETSEIB** Barcelona, Spain
M.S. in Industrial Engineering.
Illinois Institute of Technology, IIT Chicago, USA
Master's Thesis in Industrial Engineering (2005–2006).
Design of an apparatus to study the behavior of a bubble within a dielectric liquid when subject to a non–uniform electric field.

1992–2002 **Isaac Albéniz Music Conservatory** Girona, Spain
Bachelor of Music in Piano Performance (1996).
Professional Music Degree with a major in Violin.
Professional Music Degree with a major in Theory and Music History.

Experience

2009–Present **EPFL** Lausanne, Switzerland
PhD Assistant.

- Design and successfully implementation of a scalable method to fabricate silicon microwire solar cells.
- Performance of electrical and optical characterization of the system: analysis of its intrinsic and extrinsic limitations and device optimization (>10% efficiency).
- Supplier research, purchase and installation of new laboratory equipment (budget size: > 24000 CHF).
- Management and supervision of 14 master projects.

2008 **BAC VALVES, S.A.** Figueres, Spain
Homologation and Type Approval Manager.

- Management and planning of quality essays to ensure official and clients homologations.

2007–2008 **QUALIBERICA, S.L.** Girona, Spain
Technical Examiner.

- Supervision of the planning and execution of new building sites projects.
- Technical support to a portfolio of 100 customers.

2006–2007 **ECA, S.A.U.** Girona, Spain
Electrical Inspector.

- Overhaul of low tension electrification projects and their execution in agreement of the current Electrical Regulation.
- Client technical support to ensure compliance with applicable standards.

SUMMER 2004 **VIDRES TÈRMICS, S.L.** Campllong, Spain
Quality Supervisor. Establishment and management of the new quality department. Development and implementation of the quality manual for insulating glass.

SUMMER 2002 & 2003 **HUURRE IBÉRICA, S.A.** Cassà de la Selva, Spain
Quality Assistant. Performance of mechanical and thermal quality controls for metal faced sandwich panels with insulating polyurethane foam. Development of quality controls for new non-flammable polyurethane foam.

SUMMER 2001 **RICH XIBERTA, S.A.** Caldes de Malavella, Spain
Research Assistant. Development of quality control tests for cork stoppers (physical, organoleptic and microbiological analysis).

SKILLS

TECHNICAL SKILLS	Scanning Electron Microscopy (SEM) and Atomic Force Microscopy (AFM) analysis, optical and electron beam lithography, thin film deposition by sputtering and evaporation, lift–off, dry and wet etching, electrical measurements.
LANGUAGES	Catalan (native), Spanish (fluent), English (fluent) and French (fluent).
INFORMATICS SKILLS	Matlab, Origin, LabView, MS Office, SolidWorks and LaTeX.

AWARDS

2000	High school graduation with Highest Honors.
1996	Silver medal at the Table Tennis Barcelona Open.
1995	Bronze medal at the Table Tennis Catalan Championship.
1994	Honor Award in piano performance at Isaac Albéniz Music Conservatory.

EXTRA–CURRICULAR ACTIVITIES

2009–2013	Violinist at Orchestre Symphonique et Universitaire de Lausanne (OSUL).
2002–2009	Violinist at Orquestra de Cambra de Vic and Orquestra Simfònica Segle XXI.
2006–2009	Concertmaster at Jove Orquestra de Figueres.
1999-2000	Selected violinist for the Catalan National Youth Orchestra.

Publications

1. A. Dalmau Mallorquí, E. Alarcon–Lladó, E. Russo–Averchi, G. Tütüncüoğlu, and A. Fontcuberta i Morral, *Ordered growth of InAs nanowires on silicon for solar cell fabrication*, *in preparation.*
2. A. Dalmau Mallorquí, E. Alarcon–Lladó, I. Canales Mundet, A. Kiani, and A. Fontcuberta i Morral, *Field–effect passivation of silicon nanowire solar cells* , *in preparation.*
3. C. Sugnaux*, A. Dalmau Mallorquí*, J. E. Herriman, H. A. Klok, and A. Fontcuberta i Morral *Microwire solar cells with a conformal, plasmonic, nanoparticle–based electrode*, *in preparation.*
4. M. Heiss*, E. Russo–Averchi*, A. Dalmau–Mallorquí*, G. Tütüncüoğlu*, F. Matteini, D. Rüffer, S. Conesa–Boj, O. Demichel, E. Alarcon–Lladó, and A. Fontcuberta i Morral, *III–V nanowire arrays: growth and light interaction*, Nanotechnology **25** (2014), 014015.
5. E. Russo–Averchi, A. Dalmau–Mallorquí, I. Canales–Mundet, G. Tütüncüoğlu, E. Alarcon–Llado, M. Heiss, D. Rüffer, S. Conesa–Boj, P. Caroff, and A. Fontcuberta i Morral, *Growth mechanisms and process window for InAs V–shaped nanoscale membranes on Si[001]*, Nanotechnology **24** (2013), 435603.
6. E. F. Pecora, G. Walsh, C. Forestiere, A. Handin, E. Russo–Averchi, A. Dalmau–Mallorqui, I. Canales–Mundet, A. Fontcuberta i Morral, and L. Dal Negro, *Enhanced second harmonic generation from InAs nano–wing structures on silicon*, Nanoscale **5** (2013), 10163–10170.
7. A. Dalmau Mallorquí, F. M. Epple, D. Fan, O. Demichel, and A. Fontcuberta i Morral, *Effect of the pn junction engineering on Si microwire–array solar cells*, Phys. Status Solidi A **209** (2012), 1588–1591.
8. S. Conesa–Boj, E. Russo–Averchi, A. Dalmau Mallorquí, J. Trevino, E. F. Pecora, C. Forestiere, A. Handin, M. Ek, L. Zweifel, L. R. Wallenberg, D. Rüffer, M. Heiss, D. Troadec, L. Dal Negro, P. Caroff, and A. Fontcuberta i Morral, *Vertical "III–V" V–shaped nano–membranes epitaxially grown on a patterned Si[001] substrate and their enhanced light scattering*, ACS Nano **6** (2012), 10982–10991.
9. M. Hofmann, A. Cattani–Scholz, A. Dalmau Mallorquí, I. D. Sharp, A. Fontcuberta i Morral and L. Moreno i Codinachs, *Development and characterization of EIS structures based on* SiO_2 *micropillars and pores before and after their functionalization with phosphonate films*, Phys. Status Solidi A **208** (2011), 1333–1339.

(* *equal contribution*)

Conferences

Sep. 2012	*Poster*, Nanowire 2012 Workshop, Paul–Drude–Institute, Berlin (Germany).
Nov. 2011	*Poster*, Materials Research Society fall meeting, Boston (USA).
May 2011	*Oral Presentation*, École Polytechnique, invited by Prof. Roca i Cabarrocas, Paris (France).
March 2011	*Poster*, Winter School on Quantum Nanoscience, Crans–Montana (Switzerland).
Feb. 2011	*Poster*, WE–Heraeus–Seminar on "III–V Nanowires: Growth, Properties, and Applications", Bad–Honnef (Germany).